Universitat de les
Illes Balears

Programa Oficial de Postgrau de Ciències

Experimentals i Tecnologies (Física)

PH. D. THESIS

Transverse oscillations of coronal magnetic flux tube ensembles

---

Manuel Luna Bennasar

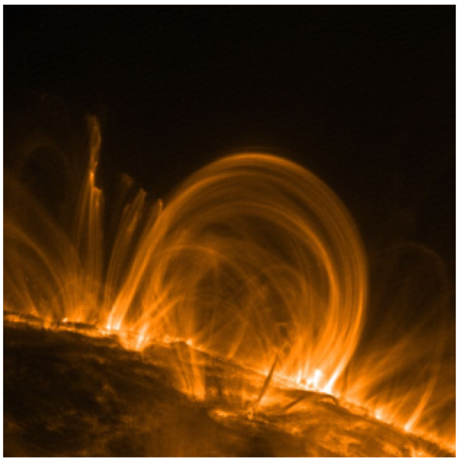

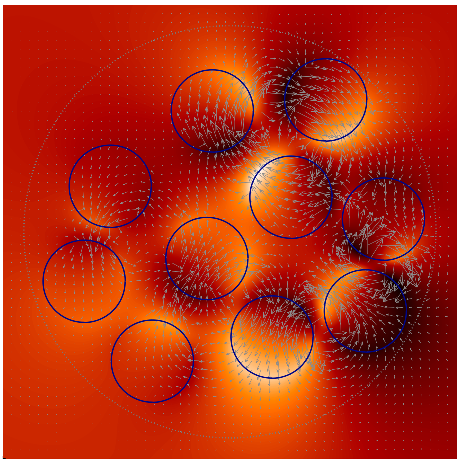

Memòria presentada per optar al Grau de Doctor
en Física per la Universitat de les Illes Balears

Directors: Drs. J. Terradas i R. Oliver

Universitat de les
Illes Balears

DEPARTAMENT DE FÍSICA

Programa Oficial de Postgrau de Ciències

Experimentals i Tecnologies (Física)

Transverse oscillations of coronal magnetic flux tube ensembles

Tesi Doctoral

Manuel Luna Bennasar

Memòria presentada per optar al Grau de Doctor
en Física per la Universitat de les Illes Balears

Directors: Drs. J. Terradas i R. Oliver

Palma de Mallorca, 14 de Maig de 2009

RESUMEN:

Oscilaciones transversales en conjuntos de tubos magnéticos coronales

La corona solar es la parte más externa de la atmósfera solar. En las zonas activas se encuentran una gran cantidad de bucles coronales que son arcos magnéticos llenos de plasma más caliente y denso que la corona circundante, y que conectan regiones de polaridad opuesta en la superficie solar. Se han observado oscilaciones transversales tras una fulguración solar gracias a los telescopios espaciales TRACE, HINODE y STEREO. Estas oscilaciones transversales han sido interpretadas en términos del modo fundamental "kink" de un tubo magnético recto. La combinación de las observaciones con modelos teóricos da lugar a la sismología coronal magnetohidrodinámica, y da información sobre distintas magnitudes físicas de la corona.

La mayor parte de estudios previos sólo han considerado las oscilaciones individuales de los bucles. Sin embargo, tras una fulguración se suelen excitar varios blucles y su dinámica podría estar afectada por la interacción mutua. Por otra parte los bucles coronales podrían tener estructura interna y estar formados por hebras finas que los telescopios actuales no pueden resolver. Estas hebras podrían estar acopladas y afectar al movimiento global del bucle. Por estos motivos se hace necesario el estudio de oscilaciones de estructuras compuestas de bucles o hebras con el fin de averiguar como la colectividad afecta a la dinámica de las oscilaciones. El objetivo de esta Tesis es proveer modelos teóricos para los propósitos de la sismología coronal.

En primer lugar se ha estudiado un sistema de dos bucles idénticos con el modelo de "slabs". Analíticamente se han estudiado los dos modos de oscilación que pueden estar relacionados con las oscilaciones transversales mencionadas anteriormente. Hemos hallado dos modos normales de oscilación con unas frecuencias y autofunciones que dependen de la separación entre bucles. El hecho que estos modos normales dependan de la separación entre bucles y que aparezcan dos modos normales en vez de uno del sistema individual indica un acoplamiento de los desplazamientos transversales. Los movimientos de los bucles asociados a uno de estos dos modos son en fase, mientras que para el otro modo son en antifase. Numéricamente se ha resuelto el problema de valores iniciales, resolviendo las ecuaciones linealizadas de la magnetohidrodinámica y se ha encontrado que

tras una perturbación inicial el sistema rápidamente oscila con un combinación de estos dos modos normales. Esta combinación hace que la dinámica del sistema sea compleja. Por ejemplo, bajo ciertas condiciones los bucles pueden intercambiar su energía por completo periódicamente en forma de batidos. Tras este estudio se ha considerado un modelo más realista de bucle basado en tubos cilíndricos. El sistema de dos bucles idénticos cilíndricos tiene cuatro modos normales colectivos de oscilación que, como en el caso del modelo de “slabs”, dependen de la separación entre bucles indicando la naturaleza colectiva de estos modos. También se ha resuelto el problema de valores iniciales y se ha hallado que dependiendo de la perturtabación inicial se excitan distintas combinaciones de modos normales colectivos. Esta superposición de modos normales también hace que la evolución temporal del sistema de bucles sea compleja. Por ejemplo, la dirección de oscilación de los bucles cambia con el tiempo debido a la interacción entre ambos.

A continuación se ha aplicado el formalismo de la “T-matrix” en el estudio de oscilaciones transversales. Esta potente herramienta nos ha permitido encontrar analíticamente los modos normales colectivos de conjuntos arbitrarios de tubos magnéticos. Uno de los resultados más interesantes que hemos encontrado es que los movimientos transversales de distintos tubos magnéticos con diferentes propiedades están fuertemente acoplados si sus frecuencias individuales de oscilación son parecidas, y sin embargo están desacoplados si son suficientemente distintas. Este resultado tiene implicaciones observacionales puesto que puede dar correcciones a las estimaciones de campo magnético de los tubos magnéticos ya que hasta ahora sólo se ha empleado el modelo de bucle aislado o individual.

Con esta misma herramienta han sido hallados los modos normales de oscilación de un bucle formado por hebras. Las hebras están fuertemente acopladas y, en consecuencia, pueden tener lugar movimientos complejos de éstas. Hay una gran cantidad de modos normales de oscilación que depende del número de hebras considerado y cuyas frecuencias se encuentran en una banda ancha. Esto indica que la interacción entre las hebras afecta a la oscilación global del bucle. Un resultado interesante es que no se ha encontrado un modo global “kink” en el que todas las hebras se muevan en la misma dirección y en fase, como sucedería en el modelo de bucle individual.

Para *Carol*

AGRADECIMIENTOS-ACKNOWLEDGEMENTS

Esta Tesis es el resultado de varios años de trabajo en el Grupo de Física Solar del Departament de Física de la UIB. Este trabajo fue iniciado el año 2005 y ha sido realizado bajo la dirección de los Doctores Jaume Terradas y Ramón Oliver. Quiero agradecer a los dos su inestimable ayuda y paciencia. Gracias a sus conocimientos y experiencia he podido introducirme en el mundo de la investigación en Física Solar. Particularmente agradezco a Ramón Oliver y Josep Lluís Ballester la oportunidad que me brindaron en el año 2005 de formar parte de su Grupo.

También querría agradecer al resto de miembros su contribución al gran ambiente de trabajo. En particular, a Iñigo Arregui, Toni Díaz, Roberto Soler, Samuel Rial, Pep Forteza y Marc Carbonell. Por otra parte agradezco al Ministerio de Ciencia e Innovación por la beca FPI del proyecto AYA2003-0123. También agradezco el apoyo económico del Ministerio de Ciencia e Innovación y de la Conselleria d'Economia, Hisenda i Innovació del Govern de les Illes Balears con los proyectos: AYA2006-07637, PRIB-2004-10145 y PCTIB-2005-GC3-03, respectivamente.

Finally, I would to thank Profs. Marcel Goossens and Bernard Roberts for their kind hospitality during my visits to the Centre for Plasma Astrophysics of the Katholieke Universiteit Leuven, Belgium and to St. Andrews University, Scotland, respectively.

Manuel Luna Bennasar

14 de Mayo de 2009

Contents

Chapter 1

Introduction

The Sun is an ordinary star of spectral type G2 V and absolute stellar magnitude 4.8, but its proximity to the Earth makes it unique and its study is of central importance to understand the behaviour of stars and plasmas in general. It is a main-sequence star, one of over 100 thousand million stars in the Milky Way Galaxy. It takes the Sun over 200 million years to complete one orbit of the galaxy. At present it is located close to the Sagittarius-Carina spiral arm, in what is called the Orion spur.

The Sun, like all stars, is such a massive ball of plasma that it is held together and compressed under its own gravitational attraction. It consists mainly of H, with 73.4% in mass, and He, with 25%, mostly in an ionised state because of the high temperature; the remaining elements, such as C, N, O, etc. comprise about 1.6% and are present in roughly the same proportions as on Earth, which suggests a common origin. Roughly speaking, the Sun is structured in concentric layers. The innermost layer of the Sun is the *core*, which extends to $0.25R_\odot$ (where $R_\odot$ is the solar radius). Here, H is converted in He by nuclear fusion, providing the energy which is slowly transported outward by continuous absorption and re-emission of photons in the *radiative zone*, which extends approximately up to $0.7R_\odot$. At this point, the radiative transport of energy is ineffective and convective transport begins. This is the *convection zone*. At the bottom of the convection zone the magnetic field is generated by the combination of convection and solar rotation, by means of the so-called *dynamo process*. On top of the solar convection zone lies the solar atmosphere.

The solar atmosphere is typically divided in four layers according to its density and temperature characteristics. The lowest part of the solar atmosphere is an extremely thin layer of plasma of approximately 450 km, called *photosphere*, which is relatively dense and opaque. Its temperature is roughly 6000 K and it emits most of the solar radiation. Above it lies the *chromosphere*, which is rarer and more transparent and where the temperature rises from 6000 K to about 20000 K. The thickness of this layer is approximately 2500 km and comes to an abrupt end in a narrow *transition region* of only a few hundred kilometres thick. Here the temperature rises dramatically from 20000 K at the top of the chromosphere to a few million K in the *corona*. However, the picture of concentric layers of the solar atmosphere is very simplistic. It is much more complex and with rapid spatial and temporal variability.

1.1 The solar corona

The corona is the Sun's outer atmosphere. It is visible during total eclipses of the Sun as a white crown surrounding the Sun. Currently, it is also seen with the SOHO (SOlar and Heliospheric Observatory), TRACE (Transition Region and Coronal Explorer), HINODE and STEREO (Solar TErrestrial RElations Observatory) satellites among others (see Figure 1.1 for a picture taken with the EIT instrument on board SOHO). Early observations of the visible spectrum of the corona revealed bright emission lines at wavelengths that did not correspond to any known element. This led astronomers to propose the existence of "coronium" as the principal gas in the corona. The true nature of the corona remained a mystery until it was determined that the coronal gases are super-heated to temperatures greater than 1000000 K. At these high temperatures, even minor elements like C, N and O are stripped down to bare nuclei. Only the heavier trace elements like Fe and Ca are able to retain a few of their electrons in this intense heat. It is emission from these highly ionised elements that produces the spectral emission lines that were so mysterious to early astronomers. The nature of the processes that heat the corona and maintain it at these high temperatures is unknown. Usually temperatures fall as you move away from a heat source. This is true in the Sun's interior right up to the visible surface. Then, over a relatively small distance, the temperature suddenly rises to extremely high values. Several mechanisms have been suggested as the source of this heating but there is no consensus on which one, or combination, is actually responsible.

1.2 Active regions and coronal loops

Several magnetic field structures exist in the solar corona on a wide range of spatial scales, with sizes of a few thousand km, such a bright points, to large coronal streamers which extend to several solar radii. We focus our attention in *active regions*, (AR) that are areas of strong magnetic field concentrations where most of the solar activity takes place (see Figures 1.1 and 1.2). In visible wavelengths AR are seen as sunspot groups in the solar surface, i.e. the photosphere.

In AR there are myriads of coronal loops that outline the magnetic field lines. Coronal loops are filled with hotter and denser plasma than the background corona producing bright emission in extreme ultraviolet (EUV) and soft X-rays wavelengths. Coronal loops are closed magnetic arches that connect magnetic regions of opposite magnetic polarity on the solar surface (see Figure 1.2a). Coronal loops are usually seen forming *bundles* or *arcades*. Bundles are disordered sets of relatively close loops (see Figure 1.2a) and arcades are relatively ordered configurations of aligned loops (see Figure 1.2b). In this

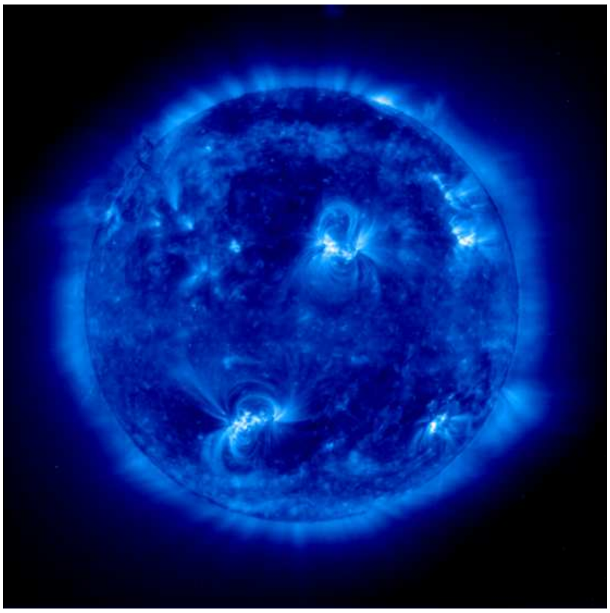

Figure 1.1: SOHO-EIT image in resonance lines of eight and nine times ionised iron (Fe IX/X) at 171 Å in the extreme ultraviolet showing the solar corona at a temperature of about 1 million K. This image was recorded on 11 September 1997. It is dominated by two large active regions, composed of numerous magnetic loops.

work we are interested in coronal loops with typical lengths of 200 Mm and temperatures of the order of 1000000 K. Loop densities are roughly $(2-10)\times 10^{-12}$ kg m^{-3}, i.e. a density enhancement of 2 – 30 times with respect to the surrounding corona.

It is currently debated whether AR coronal loops have an unresolved fine structure or not (see, e.g., Aschwanden et al., 2000; Warren et al., 2002; Schmelz et al., 2005; Aschwanden and Nightingale, 2005; Klimchuk, 2006; DeForest, 2007; Warren et al., 2008). The loop model with fine structure is the so-called *multistranded* or *multithreaded* loop. In this model it is suggested that loops are formed by several tens or hundreds of strands considered as miniloops (see Figure 1.3) for which the heating plasma properties are approximately uniform in the transverse direction. This multistrand fine structure is below the spatial resolution of the current telescopes (TRACE and HINODE). Recent observations from the EUV Imaging Spectrometer (EIS) on HINODE support the multistranded loop model (e.g., Warren et al., 2008).

1.3 Waves and loop oscillations. Magnetohydrodynamic coronal seismology

On 14 July 1998, the imaging telescope on board TRACE registered, in both 171 Å and 195 Å lines, spatially resolved decaying oscillating displacements of coronal loops in the

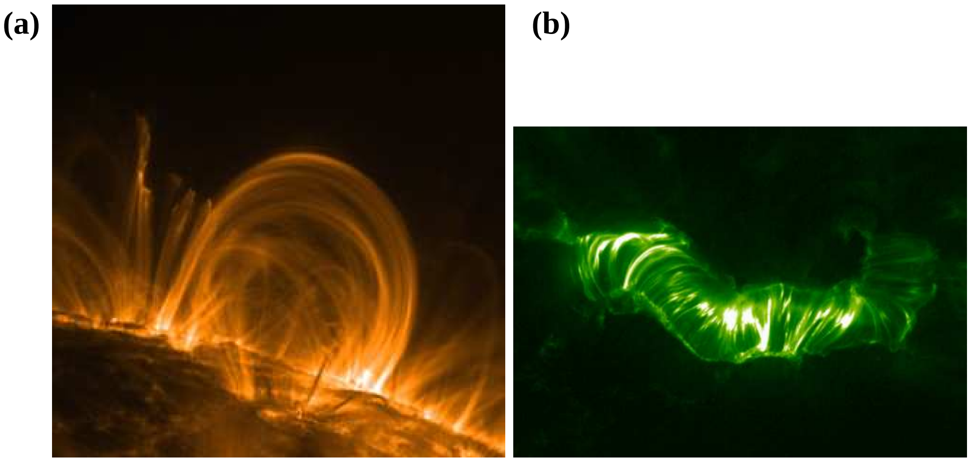

Figure 1.2: In (**a**) the structure of coronal loops is seen perfectly. They consist of curved flux tubes with their feet anchored in the photosphere. Loops are found forming bundles (**a**) or arcades (**b**). In (**b**) we see an arcade from the top (over the disk). These images were taken with TRACE in EUV light.

active region AR 8270 (see Figure 1.4). This direct detection of loop oscillation was first published in Aschwanden et al. (1999). These oscillations had periods of approximately 5 min with a strong damping. Evidences of oscillations had been reported previously by Schrijver et al. (1999) in an overview of TRACE first results. Nakariakov et al. (1999) studied the damping of the transverse loop oscillations and found a damping time close to 15 min. Schrijver and Brown (2000) analysed an event that occurred on 4 July 1999 and found an oscillations with approximately 5 min period and a damping time of 15 min. The authors reported oscillations in phase or antiphase in a bundle of closer loops. Since their first direct observation, transverse oscillations have been routinely observed with TRACE and recently with HINODE (see, e.g., Van Doorsselaere et al., 2008b) and STEREO (Verwichte et al., 2009).

A detailed and extensive study of the geometric parameters of loops and the transverse oscillations was made by Schrijver et al. (2002) and Aschwanden et al. (2002). In Table 1.1 a range of physical parameters of 26 oscillating loops are presented, extracted from 17 events taken with TRACE during 1998–2001 (Aschwanden et al., 2002). These oscillations took place shortly after a solar flare and, most probably, were generated by the flare. The mechanism of the excitation is not well understood, but it can be connected with a blast wave generated in the flare epicentre. Some of the loops seem to be more responsive to the oscillation than others and this fact could likely to be connected with the magnetic topology of the active region. The loop feet are anchored in the photosphere due to the enormous density contrast between the photospheric and coronal media (the photosphere is 10^9 times denser than corona): this is the so-called line tying effect. The loop oscillations are interpreted in terms of a standing wave. The largest oscillation amplitudes were seen near the loop apices in the transverse oscillations indicating that oscillations are mainly a fundamental mode (see Figure 1.5). Aschwanden et al. (1999),

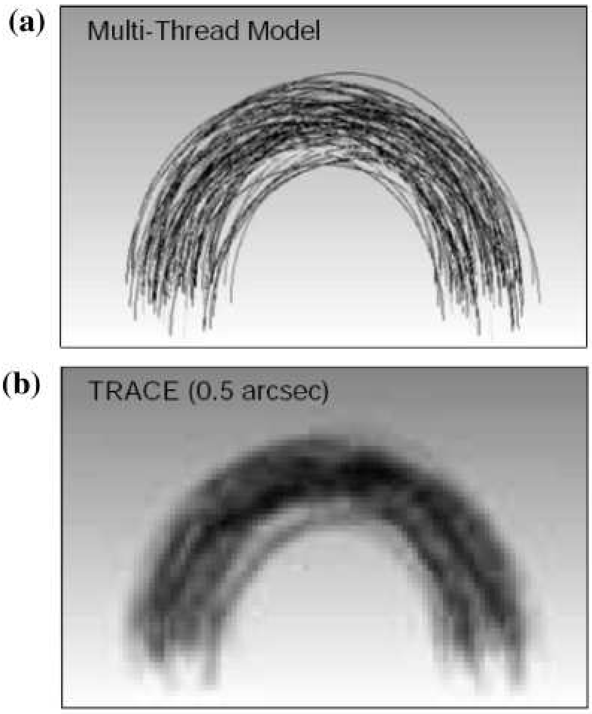

Figure 1.3: Multistranded or multithreaded loop model. In this figure the loop is a bundle of 100 fine strands with a width of $0.1''$. **(a)** shows the simulated image, while **(b)** renders the loop system with the TRACE telescope of approximately $0.5''$ resolution. We see that the loop fine structure is not well resolved and remains hidden to the observer. From Aschwanden et al. (2000).

Nakariakov et al. (1999) and Nakariakov and Ofman (2001) interpreted these transverse oscillations in terms of linear *fundamental fast magnetohydrodynamic kink modes* of a straight and cylindrical flux tube. In the fundamental standing transverse oscillation of a cylinder, the longitudinal component of the wave-vector is fixed to $k_z = \pi/L$, where L is the length of the loop. The loop width, a, is very small compared with the loop length, so that $a/L \leq 0.05$ (see Table 1.1). In coronal loops, it is a good approximation to consider $a/L \ll 1$ (or equivalently $k_z a \ll 1$), in the so-called thin tube (TT) approximation. The TT approximation allows to make considerable simplifications in the theoretical models. Transverse coronal loop oscillations are strongly damped with a mean exponential decay time of three oscillation periods. There are several possible damping mechanisms: non-ideal magnetohydrodynamic effects, lateral wave leakage, footpoint wave leakage, phase mixing and resonant absorption. However, it is the last mechanism, *resonant absorption*, that offers a consistent explanation of the rapid damping of the transverse oscillations (Goossens et al., 2002). Resonant absorption consists in the transfer of energy from the magnetohydrodynamic oscillation of the whole loop to the local resonant Alfvén waves.

On the other hand, travelling slow magnetohydrodynamic waves were observed in

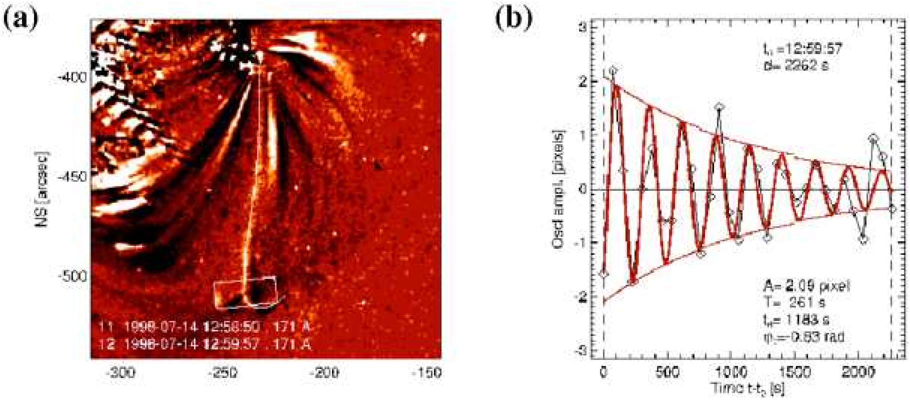

Figure 1.4: **(a)** Time difference image from TRACE 171 Å showing the AR 8270. Difference images are created by subtracting two images at different times. White areas indicate flux increase, while black areas indicate flux decrease. In **(b)** the detrended oscillation of the loop outlined with a thin white curve in **(a)** is shown. The dots are the measured displacements with respect to the equilibrium position and the color curve is an exponentially decaying sinusoid fit. Extracted from Aschwanden et al. (2002).

Parameters	Range
Loop half length ($L/2$)	37 – 291 Mm
Loop width (a)	5.5 – 16.8 Mm
a/L	0.01 – 0.05
Oscillation period	137 – 694 s
Decay time	191 – 1246 s
Oscillation duration	400 – 5388 s
Oscillation amplitude	100 – 8800 km
Number of periods	1.3 – 8.7
Maximum transverse speed	3.6 – 229 km s^{-1}

Table 1.1: Ranges of physical parameters of 26 oscillating loops observed with TRACE; extracted from Aschwanden et al. (2002).

coronal loops with TRACE (Nightingale et al., 1999; Schrijver et al., 1999; De Moortel et al., 2000) and EIT/SOHO (Berghmans and Clette, 1999). These quasi-periodic disturbances were observed, generally, in the lower parts of large, quiescent coronal loops, placed at the edges of AR or situated above sunspot umbrae. In all the cases, only propagating waves away from the loop footpoints were observed with an average speed of 122 ± 43 km s^{-1}. The observed periodicities were of the order of 5 min (O'Shea et al., 2001; De Moortel et al., 2000). A detailed study carried out by De Moortel et al. (2002) shows a distinct separation between periods of those loops above sunspot umbrae of ap-

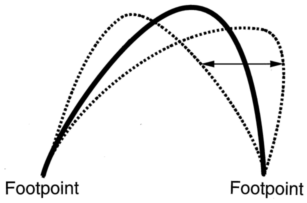

Figure 1.5: Scheme of transverse loop oscillations. It is seen that the maximum displacement happens at the apex. The foot-points are fixed in the photosphere. From Nakariakov et al. (1999).

proximately 3 min and those away from with periods of 5 min. The authors argue that loop footpoints can be coupled to the lower layers of the solar atmosphere. The oscillations of the underlying layers drive the observed slow propagating waves.

In addition, observations of hot coronal loops from SUMMER spectrometer onboard SOHO satellite, revealed large Doppler shift velocities (up to 200 km s^{-1}), which exhibit damped oscillations (Wang et al., 2002, 2003a,b). The observed oscillation periods are in the range 11–31 min and the damping time is in the range 5.5–29 min. These oscillations were interpreted in terms of *standing slow* magnetosonic modes. However, the source of the dissipation was established in Ofman and Wang (2002). The authors found that for the typical observational solar parameters of these loops, the dominant wave damping mechanism is most probably thermal conduction.

Recently, spatially and temporally ubiquitous waves have been discovered in the solar corona in the Doppler images from the COMP instrument (Tomczyk et al., 2007). Propagating waves have been reported with periods of 5 min with phase speed of approximately 1000 km s^{-1}. These waves have been interpreted as *propagating Alfvén waves* by the authors. In Tomczyk and McIntosh (2009) a detailed study of the wave propagation direction with respect to the magnetic field has been carried out. They separate outward propagation waves and inward propagation waves and have found that the energy of outward is larger than that of inward waves. This fact indicates that the travelling waves are damped as they travel into the corona. The damping time must be of the order of the travel time along the loop, which amounts to just a few wave periods. The authors also conclude that the ubiquitous waves are driven by solar *p*-modes. Van Doorsselaere et al. (2008a) and Hindman and Jain (2008) disagree with the interpretation in terms of Alfvén waves and suggest that the observed propagating disturbances are fast magnetohydrodynamic waves.

The detection of oscillations and waves in magnetic structures of the solar corona provides us with a tool for the determination of physical parameters (Uchida, 1970; Roberts et al., 1984). Measurement of the properties of magnetohydrodynamic oscillations (periods, wavelengths, amplitudes, temporal and spatial signatures, characteristic scenarios of the wave evolution), combined with a theoretical modelling of the wave phenomena (dispersion relations, evolutionary equations, etc.), leads to a determination of the mean parameters of the corona, such as the magnetic field strength and density. This is the *magnetohydrodynamic coronal seismology* (see Figure 1.6 for an outline of the seismological method). Magnetohydrodynamic coronal seismology is based upon three different wave modes, namely, Alfvén, slow and fast magnetoacoustic modes. These magnetohydrodynamic modes have quite different dispersive, polarisation and propagation properties, which makes this approach even more powerful. However, in real conditions the coronal seismology is more complicated because the three modes are coupled and have mixed properties (Goossens et al., 2009).

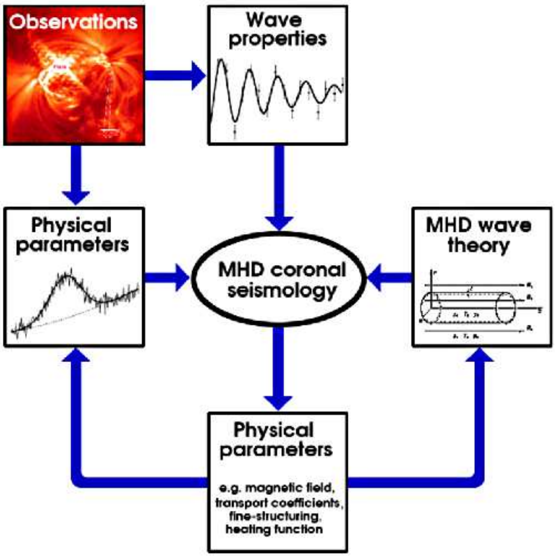

Figure 1.6: Outline of the magnetohydrodynamic coronal seismology method which is based on relating the theoretical models with the observations and thus allows us to extract physical parameters. Observations provide us with wave properties (periods, damping times, etc.) and physical parameters (loop length, radius, etc.). These data permit us to select appropriate models and to extract non-observable or derived magnitudes. This is a feedback process of mutual improvement in which the extracted parameters are included in the new observations and in the new models. Figure extracted from Nakariakov and Verwichte (2005).

1.4 Motivation and Thesis outline

In many cases the observed coronal loops belong to complex active regions and are not isolated but forming bundles or arcades. The collective joint dynamics of the system can be different from the individual loop oscillation. For example, in Schrijver and Brown (2000) antiphase transverse oscillations of adjacent loops were reported. In addition, in Verwichte et al. (2004) phase and antiphase motions were observed in a post-flare arcade (see Figure 1.7). These motions could indicate collective oscillations of the loop system. Unfortunately, additional observations are needed for a complete observational study. In addition, as we have seen in Section 1.2 coronal loops could be a composite structure of strands. These strands can be coupled and affect the whole motion of the loop.

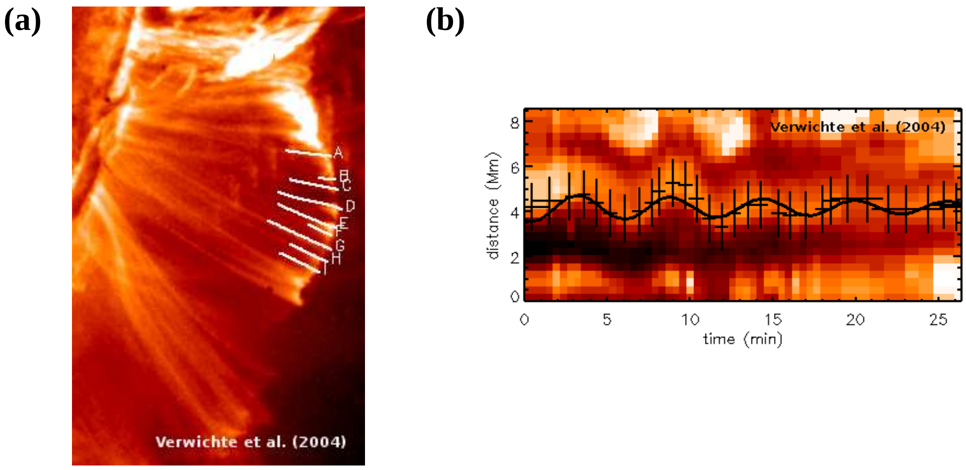

Figure 1.7: **(a)** A frame from a movie recorded by TRACE on April 15th, 2001, of a post-flare loop arcade with nine outstanding loops called A-I. **(b)** Transverse displacement of loop G near the apex. To produce this figure an 8 Mm-long segment perpendicular to loop G has been considered and its intensity has been plotted as a function of time. Extracted from Verwichte et al. (2004).

Most analytical studies about transverse loop oscillations have only considered the properties of individual loops. Only a few works have considered composite structures. Berton and Heyvaerts (1987) studied the magnetohydrodynamic normal modes of a periodic magnetic medium. Murawski (1993) and Murawski and Roberts (1994) studied numerically the propagation of fast waves in two slabs unbounded in the longitudinal direction. In Díaz et al. (2005) the oscillations of the prominence thread structure were investigated. These authors found that in a system of equal fibrils the only non-leaky mode is the symmetric one, which means that all the fibrils oscillate in spatial phase with the same frequency. Arregui et al. (2007), have studied the effects on the dynamics of the possibly unresolved internal structure of a coronal loop composed of two very close, parallel, identical coronal slabs in Cartesian geometry with non-uniform density in the transverse direction. They found small differences in the period and damping time, with respect to a single slab with the same density contrast or a single slab with the same total mass.

With these considerations, it is thus necessary a precise study of the oscillations of composite structures of several loops or strands and how the dynamics can be influenced by the collectivity. The motivation of this Thesis is to provide magnetohydrodynamic coronal seismology with theoretical models in order to compare with and to extract information from the observations. The outline of the Thesis is as follows:

- In Chapter 2 we introduce the plasma definition, i.e. we describe the state in which the gas of the Sun is found and particularly the corona. We also introduce the ideal magnetohydrodynamic equations, valid in the solar corona. In addition, the propagation of waves in a homogeneous plasma is studied. The linear theory, based on a first order approximation of the magnetohydrodynamic equations with respect to an equilibrium configuration, is presented.

- In Chapter 3 we study the loop oscillations of the slab model. Firstly, we consider the cases of a single slab and two slabs and the main properties of such systems are discussed. The normal modes are analytically calculated. The dispersion relation is derived and the eigenfunctions are obtained. Secondly, the temporal analysis is also investigated by means of numerical simulations in the case of two slabs. This study covers two parts. In the first part, we perturb the system with an initial condition in order to excite the normal modes separately. In the second part we excite the system with an arbitrary pulse. The results shown in this Chapter have been published in Luna et al. (2006).

- In Chapter 4 we consider a system of two identical cylindrical flux tubes. First, the normal modes of the system are found numerically. Second, we study the temporal evolution of the system after an initial disturbance and we investigate its dependence with the angle of the initial pulse with respect to the two loop system. The results of this investigation have been published in Luna et al. (2008).

- In Chapter 5 arbitrary flux tube systems are investigated. First, we introduce the T-matrix theory, needed to find the collective normal modes of an arbitrary flux tube system analytically. Second, we investigate the dependence of the coupling with respect to the tube parameters in systems of two and three flux tubes. Observational implications of these results are discussed. The results of this work have been published in Luna et al. (2009).

- In Chapter 6 we use the T-matrix theory to study analytically the collective normal modes of a multistranded loop system. We first consider a system of ten identical strands and classify the collective normal modes according to their frequencies and spatial structure. Second, we study a multistranded loop model composed by ten non-identical strands. Finally a much more complex system of forty strands is considered.

- Finally, in Chapter 7 the results of the work are summarised and the main conclusions are drawn. A brief discussion about future work is also presented.

Chapter 2

The plasma and the magnetohydrodynamic equations. Waves in plasmas

2.1 Plasma definition and magnetohydrodynamic description

A plasma is formed by neutral and charged particles, ions and electrons. In general a plasma is *electrically neutral* overall, but the presence of charged particles means that a plasma can support electric currents and interact with electric and magnetic fields. A useful plasma definition is (see, e.g., Chen, 1984; Goossens, 2003; Goedbloed and Poedts, 2004):

A plasma is a quasi-neutral gas (macroscopically neutral) of charged particles and neutrals that exhibits a collective behaviour.

The meaning of "collective behaviour" is as follows. There is a fundamental difference between a neutral gas and a plasma, coming from the different nature of the interaction between particles. In a neutral gas, the interaction is strong and of short-range. Hence, the dynamics is governed by the contact collisions. In a plasma, which has charged particles, the situation is different. These charges and their motion produce electric and magnetic fields. These fields exert a force and affect the motion of other charged particles far away. Then, by "collective behaviour" we mean motions that depend not only on the local conditions but on the state of the plasma in remote regions as well. The dynamics of a plasma interacting with magnetic and electric fields is described by quite different theoretical models. Which one is to be chosen depends on the kind of phenomenon one is interested in. In this work we use *the magnetohydrodynamic (MHD) model*, in which we postulate a hypothetical medium called "plasma" governed by the MHD equations. The validity of such equations is justified by physical and mathematical arguments.

The *MHD model* is a macroscopic, classical and non-relativistic theory that treats the global phenomena of a plasma considered as a single fluid interacting with a magnetic field. In addition we consider the fluid as inviscid and adiabatic. Maxwell's equations describe the electromagnetic field and the gas dynamics is governed by the fluid equations. However, these equations are not a closed set and we need an additional equation. This equation is the *generalised Ohm's law* that links the electrical density current **j** to the fields **E**, **B** and **v** in the MHD approximation,

$$\mathbf{j} = \sigma (\mathbf{E} + \mathbf{v} \times \mathbf{B}) \tag{2.1}$$

where σ is the electrical conductivity of the fluid. Combining this equation with the Faraday's and the modified Ampere's law, the *induction equation* is obtained,

$$\frac{\partial \mathbf{B}}{\partial t} = \nabla \times (\mathbf{v} \times \mathbf{B}) + \eta \nabla^2 \mathbf{B} \, , \tag{2.2}$$

where $\eta = 1/\mu\sigma$ is the magnetic diffusivity, which has been taken constant. The induction equation governs the temporal evolution of the magnetic field. There are two contributions on the right-hand side of the previous equation. The first one is the *advection term* and the second one is the *diffusive term*. The magnetic Reynolds number R_m determines the relative importance of both terms,

$$R_m = \frac{|\nabla \times (\mathbf{v} \times \mathbf{B})|}{\eta \, |\nabla^2 \mathbf{B}|} \approx \frac{vB/l}{\eta B/l^2} = \frac{vl}{\eta} \, . \tag{2.3}$$

In this Thesis we consider magnetic structures in the solar corona where the magnetic Reynolds number is $R_m \approx 10^8 - 10^{12}$ (see, e.g., Aschwanden et al., 2004). Hence, the solar corona is in the limit $R_m \gg 1$ and the diffusive term of Equation (2.2) can be neglected and the advection term dominates in the magnetic field evolution. The induction equation takes the form

$$\frac{\partial \mathbf{B}}{\partial t} = \nabla \times (\mathbf{v} \times \mathbf{B}) \, . \tag{2.4}$$

Under these conditions magnetic field lines move with the plasma, a result which is known as Alfvén's frozen-flux theorem (see, e.g., Priest, 1987). The limit of large Reynolds number ($R_m >> 1$) is equivalent to considering a perfectly conducting fluid with $\sigma \to \infty$. In this limit the model is the so-called *ideal* MHD. If the conductivity is not large and the full induction equation is valid the model is called *resistive* MHD.

2.2 The ideal magnetohydrodynamic model

The magnetised plasma of the solar corona is well described by the *ideal* MHD model. Thus, the governing equations are

$$\frac{\partial \rho}{\partial t} + \nabla \cdot (\rho \mathbf{v}) = 0, \tag{2.5}$$

$$\rho \frac{\partial \mathbf{v}}{\partial t} + \rho\,(\mathbf{v}\cdot\nabla)\mathbf{v} = -\nabla p + \frac{1}{\mu}\,(\nabla\times\mathbf{B})\times\mathbf{B}, \tag{2.6}$$

$$\frac{\partial p}{\partial t} + \mathbf{v}\cdot\nabla p = -\gamma p \nabla\cdot\mathbf{v}, \tag{2.7}$$

$$\frac{\partial \mathbf{B}}{\partial t} = \nabla\times(\mathbf{v}\times\mathbf{B})\,, \qquad \nabla\cdot\mathbf{B} = 0. \tag{2.8}$$

These are a set of nine non-linear partial differential equations for eight variables $\rho(\mathbf{r}, t)$, $\mathbf{v}(\mathbf{r}, t)$, $p(\mathbf{r}, t)$ and $\mathbf{B}(\mathbf{r}, t)$.

The Lorentz force term $(\nabla\times\mathbf{B})\times\mathbf{B}/\mu$ of Equation (2.6), can be decomposed in the following manner

$$\frac{1}{\mu}\,(\nabla\times\mathbf{B})\times\mathbf{B} = (\mathbf{B}\cdot\nabla)\frac{\mathbf{B}}{\mu} - \nabla\left(\frac{B^2}{2\mu}\right)\,, \tag{2.9}$$

where the first term on the right-hand side represents the effects of a tension due to the magnetic field line curvature and the second term is a magnetic pressure force acting from regions of high to low magnetic pressure and with magnitude $B^2/(2\mu)$. We define the total pressure as the sum of the fluid pressure and the magnetic pressure,

$$p_T = p + \frac{B^2}{2\mu}\,. \tag{2.10}$$

With this decomposition of the Lorentz force, we obtain the new version of Equation (2.6)

$$\rho \frac{\partial \mathbf{v}}{\partial t} + \rho\,(\mathbf{v}\cdot\nabla)\mathbf{v} = -\nabla p_T + (\mathbf{B}\cdot\nabla)\,\frac{\mathbf{B}}{\mu}\,. \tag{2.11}$$

From this equation we see that the forces acting on a plasma element are the total pressure and the magnetic tension, while other contributions like gravity, viscosity, etc. are not considered here.

Zero-β plasma limit

In many applications, specially in the solar corona, there is an important simplification that can be done in the MHD equations. In the rearranged motion Equation (2.11) there is a gradient of the total pressure. The total pressure is the sum of the gas pressure and the magnetic pressure and the relative importance of the two terms can be estimated by the plasma β parameter, defined as

$$\beta = \frac{\text{gas pressure}}{\text{magnetic pressure}} = \frac{p}{B^2/2\mu} \tag{2.12}$$

In the corona this parameter is very small ($\beta_{corona} \ll 1$) and, therefore, in coronal plasmas we assume $\beta \approx 0$. This is called the *zero-β plasma limit* or cold plasma approximation, in which the plasma is completely dominated by the magnetic field and the *gas pressure is negligible*. In this limit Equations (2.5)–(2.8) can be written as

$$\frac{\partial \rho}{\partial t} + \nabla \cdot (\rho \mathbf{v}) = 0, \tag{2.13}$$

$$\rho \frac{\partial \mathbf{v}}{\partial t} + \rho\,(\mathbf{v} \cdot \nabla)\mathbf{v} = \frac{1}{\mu}\,(\nabla \times \mathbf{B}) \times \mathbf{B}, \tag{2.14}$$

$$\frac{\partial \mathbf{B}}{\partial t} = \nabla \times (\mathbf{v} \times \mathbf{B})\,, \quad \nabla \cdot \mathbf{B} = 0\,. \tag{2.15}$$

These are the *ideal MHD equations in the zero-β approximation*. The energy Equation (2.7) is not needed in this approximation.

2.3 Fast magnetohydrodynamic waves in homogeneous plasma

In a gas, a disturbance produces compressions and rarefactions that are propagated isotropically at the sound speed of the medium and that produce pressure, density and temperature variations. In a magnetised plasma the situation is more complicated. The charged particles of the plasma interact with the magnetic field and variations in the gas pressure will generally lead to magnetic field disturbances. In a perfectly conducting fluid considered in this work, the magnetic field lines and the fluid are frozen together, so any disturbance in the fluid produces changes in the magnetic field. In addition, the magnetic field exerts a restoring force on the fluid through the magnetic pressure and tension. Then, the interaction of the fluid and magnetic disturbances produces a rich variety of waves. A convenient way to find the response of a system to excitations is to consider small perturbations with respect to an equilibrium situation. Mathematically this means that we can linearise the governing equations of the system, assuming that we are only interested in the dynamics caused by small distortions (linear terms) of the plasma equilibrium.

2.3.1 Linear waves

Consider a uniform and static equilibrium configuration ($\partial/\partial t = 0$, $\mathbf{v} = 0$), that satisfies the MHD equations in the *zero-β plasma limit* (Equations 2.13 to 2.15). Since the plasma is homogeneous the equilibrium variables, which are hereafter labelled with the subscript “0”, do not depend on the position. Next, the physical variables are assumed to suffer a small displacement (see, e.g., Priest, 1987)

$$\mathbf{B}(\mathbf{r}, t) = \mathbf{B}_0 + \mathbf{B}_1(\mathbf{r}, t)\,, \tag{2.16}$$

$$\mathbf{v}(\mathbf{r}, t) = \mathbf{0} + \mathbf{v}_1(\mathbf{r}, t)\,, \tag{2.17}$$

$$\rho(\mathbf{r}, t) = \rho_0 + \rho_1(\mathbf{r}, t)\,. \tag{2.18}$$

Notice that the equilibrium velocity has been set to zero and, although this is not strictly necessary, in the models of coronal structures studied here equilibrium flows are not included. Now Equations (2.13)–(2.15) are linearised and squares and products of the small quantities (second order terms) are neglected, giving as a result

$$\begin{aligned} \frac{\partial \rho}{\partial t} + \rho_0 \nabla \cdot \mathbf{v} &= 0, && (2.19) \\ \rho_0 \frac{\partial \mathbf{v}}{\partial t} - \frac{1}{\mu} (\nabla \times \mathbf{B}) \times \mathbf{B}_0 &= \mathbf{0}, && (2.20) \\ \frac{\partial \mathbf{B}}{\partial t} - \nabla \times (\mathbf{v} \times \mathbf{B}_0) &= \mathbf{0}, && (2.21) \\ \nabla \cdot \mathbf{B} &= 0, && (2.22) \end{aligned}$$

where the subscript “1” in the perturbed quantities has been dropped. The spatial derivatives of the equilibrium configuration are taken zero because we have assumed a homogeneous medium. Notice that the continuity Equation (2.19) is no longer necessary except for the calculation of the density perturbation.

The magnetic field is uniform and the z-axis is placed along it, then $\mathbf{B}_0 = B_0 \mathbf{e}_z$. It is easy to see from Equation (2.20) that the time derivative of the velocity, $\partial \mathbf{v}/\partial t$, is perpendicular to the equilibrium magnetic field $\mathbf{B}_0$. Then, we have $\partial v_z/\partial t = 0$ or $v_z =$ const, but here constant flows are not taken into account (see Equation 2.17), so we just take

$$v_z = 0. \qquad (2.23)$$

This result implies that the velocity is always perpendicular to the equilibrium magnetic field, i.e. $\mathbf{v} \perp \mathbf{B}_0$. In the following development, the symbol $\perp$ stands for the components of the perturbed quantities perpendicular to $\mathbf{B}_0$, i.e. in the xy-plane. Then the velocity is $\mathbf{v} = \mathbf{v}_\perp$. When the gas pressure is included the component of the velocity along $\mathbf{B}_0$ is not zero because an extra term associated to the perturbed gas pressure gradient appears in Equation (2.6).

The Lorentz force perturbation in Equation (2.20) can be decomposed in the gradient of the perturbed magnetic pressure and the perturbed magnetic tension (see Equation 2.11),

$$\rho_0 \frac{\partial \mathbf{v}}{\partial t} = -\nabla \left(\frac{\mathbf{B}_0 \cdot \mathbf{B}}{\mu} \right) + (\mathbf{B}_0 \cdot \nabla) \frac{\mathbf{B}}{\mu} , \qquad (2.24)$$

where the magnetic pressure perturbation is

$$p_m = \frac{\mathbf{B}_0 \cdot \mathbf{B}}{\mu} , \qquad (2.25)$$

that coincides with the total pressure perturbation in the zero-β limit (see Equation 2.10),

$$p_T = p_m . \qquad (2.26)$$

The second term of Equation (2.24) is the magnetic tension perturbation,

$$\tau = (\mathbf{B}_0 \cdot \nabla)\,\frac{\mathbf{B}}{\mu}\ . \tag{2.27}$$

The set of Equations (2.20)–(2.22) can be reduced to a single equation for the velocity alone by eliminating the magnetic field. Then, after some manipulation a *wave equation* is derived

$$\rho_0 \frac{\partial^2 \mathbf{v}_\perp}{\partial t^2} - \frac{1}{\mu}\left[(\nabla \times (\nabla \times (\mathbf{v}_\perp \times \mathbf{B}_0))) \times \mathbf{B}_0\right] = \mathbf{0}\ , \tag{2.28}$$

On the other hand, Equations (2.20)–(2.22) are expressions for the perturbed magnetic field and velocity field. Depending on the considered problem it is more useful to rewrite the equations in terms of other quantities. Particularly, we are interested in the magnetic pressure perturbation (p_T) and fluid velocity ($\mathbf{v}$) fields. After some algebra these equations are

$$\left(\frac{\partial^2}{\partial t^2} - v_A^2 \nabla^2\right) p_T \quad = \quad 0\ , \tag{2.29}$$

$$\rho_0 \left(\frac{\partial^2}{\partial t^2} - v_A^2 \frac{\partial^2}{\partial z^2}\right) \mathbf{v}_\perp + \nabla_\perp \frac{\partial p_T}{\partial t} \quad = \quad 0\ , \tag{2.30}$$

where the v_A is the Alfvén velocity of the magnetised medium defined as

$$v_A = \frac{B_0}{\sqrt{\mu \rho_0}}\ . \tag{2.31}$$

Equation (2.29) is a wave equation for the magnetic pressure perturbation that propagates isotropically in a homogeneous plasma. From Equation (2.30) we see that disturbances in the velocity produce disturbances in the magnetic pressure and vice versa.

2.3.2 Plane-wave solutions and dispersion relation

In order to gain insight into the properties of MHD waves, we seek plane-wave and harmonic time dependence solutions of the previous equations of the form

$$a(\mathbf{r}, t) = \hat{a}\ e^{i(\mathbf{k}\cdot\mathbf{r} - \omega t)} \tag{2.32}$$

where a represents p_T, ρ or the components of the $\mathbf{v}$, $\mathbf{B}$ fields, $\mathbf{k}$ is the wavevector that is $\mathbf{k} = k_x \mathbf{e}_x + k_y \mathbf{e}_y + k_z \mathbf{e}_z$ in Cartesian coordinates and ω is the angular frequency. We introduce these assumptions in our equations. This is equivalent to performing the following transformations

$$\frac{\partial}{\partial t} \quad \rightarrow \quad -i\omega\ \ , \tag{2.33}$$

$$\nabla \quad \rightarrow \quad i\,\mathbf{k}\ \ . \tag{2.34}$$

Then Equation (2.28) can be written as

$$\rho_0\omega^2\hat{\mathbf{v}} - \frac{1}{\mu}\left[(\mathbf{k}\times(\mathbf{k}\times(\hat{\mathbf{v}}\times\mathbf{B}_0)))\times\mathbf{B}_0\right] = 0\,,\ \ \mathbf{k}\cdot\hat{\mathbf{B}} = 0\,. \tag{2.35}$$

The result $\mathbf{k}\cdot\hat{\mathbf{B}} = 0$ means that the magnetic field perturbations are transverse to the propagation direction. After some manipulation and using Equation (2.23), i.e. $v_z = 0$, we find the following *dispersion relation*

$$\left(\omega^2 - k_z^2 v_A^2\right)\hat{\mathbf{v}}_\perp - (\mathbf{k}\cdot\hat{\mathbf{v}})v_A^2\mathbf{k}_\perp = 0\,, \tag{2.36}$$

where we see that the parallel component to the equilibrium magnetic field of Equation (2.35) is identically zero. Assuming a wave-vector $\mathbf{k}$ in the xz-plane, i.e. $k_y = 0$, the x- and y-component of Equation (2.36) become

$$\left(\omega^2 - k^2 v_A^2\right)\hat{v}_x = 0\,, \tag{2.37}$$

$$\left(\omega^2 - k_z^2 v_A^2\right)\hat{v}_y = 0\,, \tag{2.38}$$

where $k^2 = k_x^2 + k_y^2 + k_z^2$. Equations (2.37) and (2.38) are a homogeneous linear system of equations. In order to have a solution different from $\hat{v}_x = 0$ and $\hat{v}_y = 0$, the determinant of the coefficients must be zero,

$$\left(\omega^2 - k^2 v_A^2\right)\left(\omega^2 - k_z^2 v_A^2\right) = 0\,, \tag{2.39}$$

which yields two solutions. The first root is the *fast-wave dispersion relation*

$$\omega^2 = k^2 v_A^2\,, \tag{2.40}$$

and from Equation (2.38) we have $\hat{v}_y = 0$, indicating that $\hat{\mathbf{v}}_\perp \parallel \mathbf{k}_\perp$ and that fluid motions are in the plane containing $\mathbf{k}$ and $\mathbf{B}_0$. The second root of Equation (2.39) is the *Alfvén-wave dispersion relation,*

$$\omega^2 = k_z^2 v_A^2\,, \tag{2.41}$$

and from Equation (2.37) we have $\hat{v}_x = 0$ or $\hat{\mathbf{v}}_\perp \perp \mathbf{k}_\perp$, so that fluid displacements are in the direction perpendicular to the plane containing $\mathbf{k}$ and $\mathbf{B}_0$.

We expand Equations (2.29) and (2.30) in terms of plane-waves (Equation 2.32) and obtain the magnetic pressure perturbation

$$\hat{p}_T = -\frac{\rho_0 v_A^2}{\omega}\left(\mathbf{k}_\perp\cdot\hat{\mathbf{v}}_\perp\right). \tag{2.42}$$

In addition, we can find the density perturbation from Equation (2.19) as

$$\hat{\rho} = -\frac{\rho_0}{\omega}\left(\mathbf{k}_\perp\cdot\hat{\mathbf{v}}_\perp\right)\,, \tag{2.43}$$

and together Equation (2.42) we find

$$\hat{p}_T = v_A^2\,\hat{\rho}\,, \tag{2.44}$$

indicating that the density and magnetic pressure perturbations are proportional. Equations (2.42) and (2.43) relate the magnetic pressure perturbation and density variations, respectively, with $\mathbf{k}_\perp \cdot \hat{\mathbf{v}}_\perp$. Thus, the *fast* and *Alfvén* waves produce different perturbations in the magnetic pressure and density fields. *Fast* waves produce the maximum perturbations of those fields because $\mathbf{k}_\perp \parallel \hat{\mathbf{v}}_\perp$. However, *Alfvén* waves do produce no disturbance in the magnetic pressure and density fields because $\mathbf{k}_\perp \perp \hat{\mathbf{v}}_\perp$.

As we have seen in the previous analysis there are two kinds of waves in the zero-β plasma limit, whose main properties are summarised here:

- *Alfvén waves*. Driven by tension forces with no magnetic pressure or density variations (incompressible). Plasma motion is transverse to both the applied magnetic field and the direction of propagation. Highly anisotropic mode, unable to propagate across the field, with energy flowing along field lines at the Alfvén speed v_A.
- *Fast waves*. Driven by tension and magnetic pressure forces, with magnetic pressure and density variations. Isotropic, although propagating faster across the field in the $\beta \neq 0$ case.

If the zero-β plasma limit is not assumed ($\beta \neq 0$) there is a third kind of wave:

- *Slow waves*. Driven by tension and pressure forces, with pressure and density variations too. Anisotropic, unable to propagate across field lines, the energy flow is confined to the vicinity of certain magnetic field lines.

2.3.3 Boundary conditions

The equilibrium systems considered in this Thesis consist of several uniform media having different equilibrium features and the waves in each media are described by the equations seen in the previous Sections. We must impose boundary conditions (or “jump” conditions) on the perturbed plasma parameters at the contact surface of the different media. The ideal MHD model includes the set of Equations (2.19)–(2.22) but also the boundary conditions. We shall use the convention $[m] = m_2 - m_1$ for the jump of the magnitude m at the interface between two plasmas, labelled “1” and “2”. These boundary conditions include $\mathbf{n}$, the vector normal to the interface. In our systems $\mathbf{n} \cdot \mathbf{B}_0 = 0$, then the boundary conditions are (see, e.g., Goedbloed and Poedts, 2004)

$$\mathbf{n} \cdot [\mathbf{v}] = \mathbf{n} \cdot [\mathbf{B}] = 0, \;\; [p_T] = 0. \qquad (2.45)$$

We see that the normal component of velocity and magnetic field are continuous whereas the other components may have discontinuities. The boundary conditions take different expressions according to the considered loop geometry (see Chapters 3, 4 and 5).

Chapter 3

Two slab model[1]

In this Chapter we consider the oscillations of a system of two identical coronal loops modelled as slabs. We do not consider gravity, neither as restoring force nor its effect on plasma stratification. The dynamics of a curved magnetised tube are too complex and it is customary to consider a simplified model consisting of a slab that extends infinitely in one direction (the y-direction in our case) and is bounded by two parallel planes representing the photosphere. The influence of the photospheric line-tying is incorporated by imposing the vanishing of velocity perturbations at the ends of the slabs. We assume that their oscillations are linear and can be described by the linearised MHD equations of Chapter 2.

This Chapter is organised as follows. In Section 3.1 the loop model and the basic MHD equations describing fast waves are presented in a system of one slab and the normal modes are described. In Section 3.2 the system of two identical slabs is presented and in Section 3.3 the normal modes are computed. The features of trapped and leaky modes are analysed in detail. In Section 3.4 the time-dependent problem is considered and the resulting velocity profiles are studied for several initial perturbations. An analytical analysis of the beating that takes place when a combination of both normal modes of the system are excited, is given in Section 3.5. Finally, in Section 3.6 the main conclusions are drawn.

3.1 Single slab model

In this Section we show the results for the single slab system, which was first studied by Edwin and Roberts (1982). The magnetic field is homogeneous everywhere and parallel

---

[1] The novel results in this Chapter have been published in Luna et al. (2006)

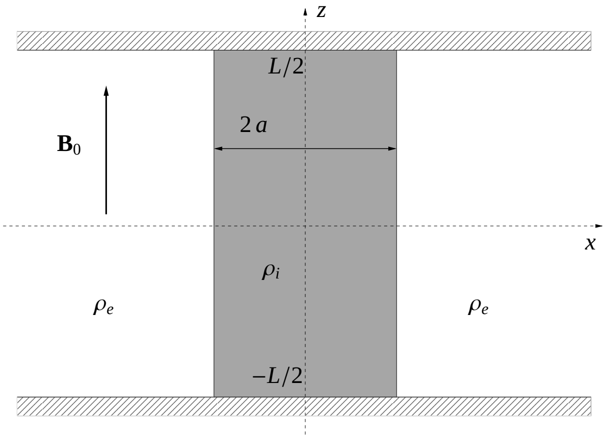

Figure 3.1: Equilibrium configuration of a system of one slab representing a coronal loop. The shaded region is the density enhancement in the slab. The internal (or slab) density is ρ_i and the external (or coronal) density is ρ_e. The equilibrium magnetic field, $\mathbf{B}_0$, is along the slab (z-axis). The slab is anchored in the photosphere (hatched area), that fixes the feet and produces the line-tying effect. The slab length is L and its width is $2a$.

to the z-axis ($\mathbf{B}_0 = B_0\mathbf{e}_z$). The density profile is (see Figure 3.1)

$$\rho(x) = \begin{cases} \rho_i, & \text{if } |x| \leq a, \\ \rho_e, & \text{if } |x| > a, \end{cases} \tag{3.1}$$

where a is the half-width of the slab. From Equations (2.28) we obtain two *decoupled* wave equations for the fast and Alfvén waves, respectively. The fast wave equation is for the v_x component that propagates isotropically in the x- and z-direction and the Alfvén wave equation is for the v_y component that propagates mainly along the magnetic field (z-axis) as we have seen in Section 2.3.2. We do not consider wave propagation along the y-axis, so that $k_y = 0$ or equivalently $\partial/\partial y = 0$ (see Section 2.3.2). This means that we only consider perturbations in the x-axis and the Alfvén waves are avoided. We propose solutions of the form $v_x(x, z, t) = \hat{v}_x(x, t)e^{-ik_z z}$, i. e. we Fourier analyse in the z-direction. From Equation (2.28) and the previous assumptions the wave equation can be written as

$$\frac{\partial^2 v_x}{\partial t^2} = v_A^2 \frac{\partial^2 v_x}{\partial x^2} - \omega_c^2\, v_x, \tag{3.2}$$

where the symbol ˆ has been dropped and ω_c is the cut-off frequency defined as $\omega_c = k_z v_A$. Equation (3.2) is a Klein-Gordon equation for fast waves. Selecting an appropriate value of k_z we include the effect of photospheric line-tying, i.e. we consider standing waves in the z-direction. We concentrate in the fundamental standing wave with $k_z = 2\pi/2L$ where the maximum amplitude is in the loop apex as in the majority of observations of transverse loop oscillations (see Section 1.3).

3.1.1 Normal mode analysis

We consider that the time and x-dependence are of the form $e^{-i\omega t}$ and $e^{ik_x x}$, respectively. Then, from Equation (3.2) we obtain

$$k_x^2 = \frac{\omega^2}{v_A^2} - k_z^2 \,, \tag{3.3}$$

that links the oscillating frequency ω with k_x (see Equation 2.40).

Equation (3.2) is valid in both regions (internal or external) with its Alfvén velocity $v_{Ai} = B_0/\sqrt{\mu\rho_i}$ and $v_{Ae} = B_0/\sqrt{\mu\rho_e}$. The solution of the perturbed velocity is

$$v_x(x) = \begin{cases} A\, e^{k_e x}, & \text{if } x < -a, \\ B_1\, e^{-ik_i x} + B_2\, e^{ik_i x}, & \text{if } -a \le x \le a, \\ C\, e^{-k_e x}, & \text{if } x > a, \end{cases} \tag{3.4}$$

where incoming waves are not considered. Here k_e and k_i are the external and internal wavenumbers. The internal wavenumber is given by

$$k_i = \sqrt{\frac{\omega^2}{v_{Ai}^2} - k_z^2}. \tag{3.5}$$

Depending on the character of k_e and ω there are two types of solutions. *Trapped modes* confine energy within the slab and are characterised by real k_e and ω, with

$$k_e = \sqrt{k_z^2 - \frac{\omega^2}{v_{Ae}^2}}. \tag{3.6}$$

Leaky modes do not confine energy, which is radiated in the environment, and are characterised by complex k_e and ω, where

$$k_e = -\sqrt{k_z^2 - \frac{\omega^2}{v_{Ae}^2}}, \tag{3.7}$$

(see, e.g., Terradas et al., 2005a). With the velocity profile of Equation (3.4) and the boundary conditions Equations (2.45), we can obtain the dispersion relation and the velocity profile, i.e. the constants A, B_1, B_2, C. From Equations (2.20) and (2.21) the boundary conditions Equations (2.45) are

$$[v_x] = \left[\frac{\partial v_x}{\partial x}\right] = 0, \text{ at } x = \pm a. \tag{3.8}$$

We impose both boundary conditions at the two interfaces located at $x = \pm a$, thus obtaining two equations for the velocity and two equations for its x-derivative. These equations form a homogeneous linear system of four equations with four unknowns, i.e. A, B_1, B_2, C. For this system of equations to have a non-trivial solution, its determinant must be zero. This gives the dispersion relation,

$$\left[\tan(a\,k_i) - \frac{k_e}{k_i}\right]\left[\tan(a\,k_i) + \frac{k_i}{k_e}\right] = 0, \tag{3.9}$$

which produces

$$\tan(a\,k_i) = -\frac{k_i}{k_e}, \tag{3.10}$$

that is, the *sausage* mode dispersion relation, and

$$\tan(a\,k_i) = \frac{k_e}{k_i}, \tag{3.11}$$

that is, the *kink* mode dispersion relation. *Sausage* modes have an antisymmetric velocity profile with respect to $x = 0$ (the slab axis) and *kink* modes have a symmetric profile. Moreover, the solutions of the homogeneous set of equations, i.e. the constants in Equation (3.4), are the kernel of the matrix of the system. With this procedure the velocity profiles of Figure 3.2 are found.

Transcendental Equations (3.10) and (3.11) are solved and ω is calculated for different values of the slab half-width, a/L, finding two types of curves (Figure 3.3). Figures 3.3a and 3.3b correspond to the real and imaginary part of the frequency, that has been written as $\omega = \omega_R + i\omega_I$. Here we only represent the fundamental and first harmonic of the kink and sausage modes. The frequency of trapped modes is real and smaller than the external cut-off frequency, $\omega_{ce} = \omega_c = k_z v_{Ae}$. Since $\omega_I = 0$ for trapped modes, these solutions correspond to standing oscillations of the system and the oscillation is confined near the slab (see Figures 3.2a and 3.2b). Leaky modes have complex frequency with $\omega_I > 0$, so that they represent damped oscillations, the origin of the damping being that perturbations carry the energy away from the slab. The leaky modes also present spatial oscillations growing in amplitude as $x \to \pm\infty$ (see Figures 3.2c and 3.2d). Figure 3.3a shows that the fundamental kink mode (solid line) is trapped for all a/L. On the other hand, the fundamental sausage mode (dashed line) starts as leaky for small values of a/L and, as a/L is increased, its curve crosses the external cut-off frequency, bifurcates and gives rise to two branches. At the bifurcation point the imaginary part of the frequency becomes zero (Figure 3.3b) and the two branches have $\omega_I = 0$. Both branches are physically meaningless because they have $\omega_I = 0$ and k_e is real and negative, which implies an oscillatory solution in time with an exponential growth in space. For even larger slab half-widths the upper branch reaches the external cut-off and the mode becomes trapped (thick dashed line), becoming a physically relevant solution. All the harmonics (both kink and sausage) have the same behaviour as the fundamental sausage mode, although in the range of half-widths plotted in Figure 3.3 they are leaky. From Figure 3.3b we see that the damping time, $\tau = \omega_I^{-1}$, increases with a. Following Terradas et al. (2005b), it is possible

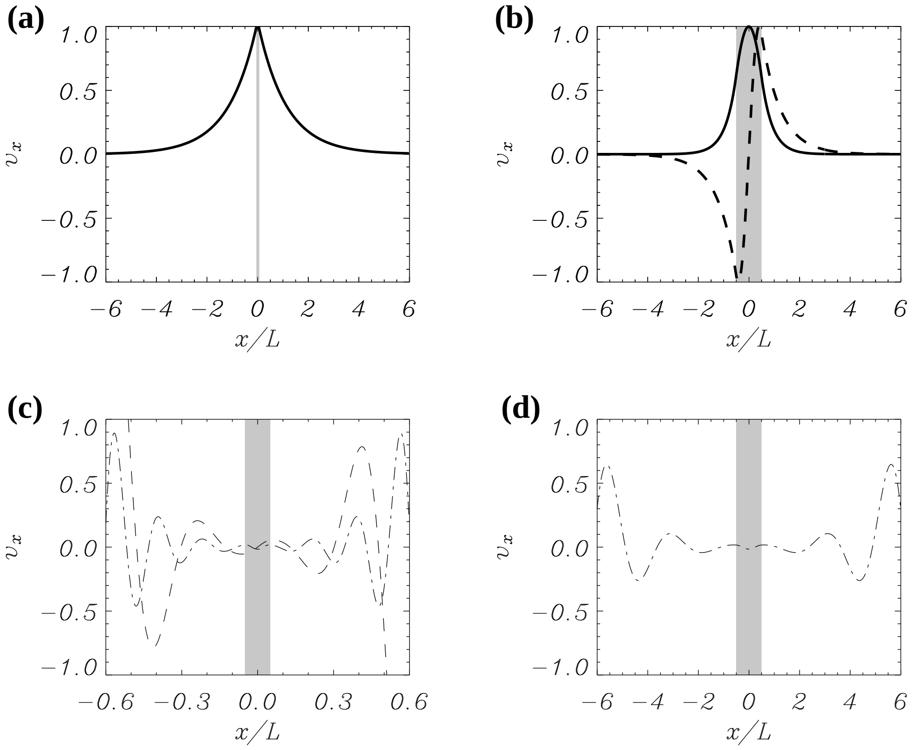

Figure 3.2: Plot of the eigenfunction v_x for **(a)** and **(b)** the trapped modes (thick curves) and **(c)** and **(d)** some leaky modes (thin curves) (Terradas et al., 2005a). Continuous line for the fundamental kink mode, dashed line for the sausage mode and dot-dashed line for the first kink harmonic. **(a)** and **(c)** correspond to a slab with $a/L = 0.05$ while for **(b)** and **(d)** $a/L = 0.5$. Note that the sausage mode, that is trapped in a thick slab, becomes leaky in a thin one; also note the different spatial scale for the plot of the leaky modes with $a/L = 0.05$. The grey area represents the slab.

to find an analytical expression for this damping time in the limit of thin slabs ($a \ll L$) valid in coronal loops

$$\tau \approx \frac{2a}{v_{Ai}} \left(\ln \left| \frac{1 + v_{Ai}/v_{Ae}}{1 - v_{Ai}/v_{Ae}} \right| \right)^{-1} . \tag{3.12}$$

Note that the damping time is independent of the normal mode considered, so that in the limit $a/L \ll 1$ all leaky harmonics have the same damping time (see Figure 3.3b). Moreover, when $v_{Ai} \ll v_{Ae}$ the damping time reduces to

$$\tau \approx a\, \frac{v_{Ae}}{v_{Ai}^2}. \tag{3.13}$$

From these equations we see that the leaky modes radiate their energy very rapidly. In coronal loop conditions it is of the order of several seconds.

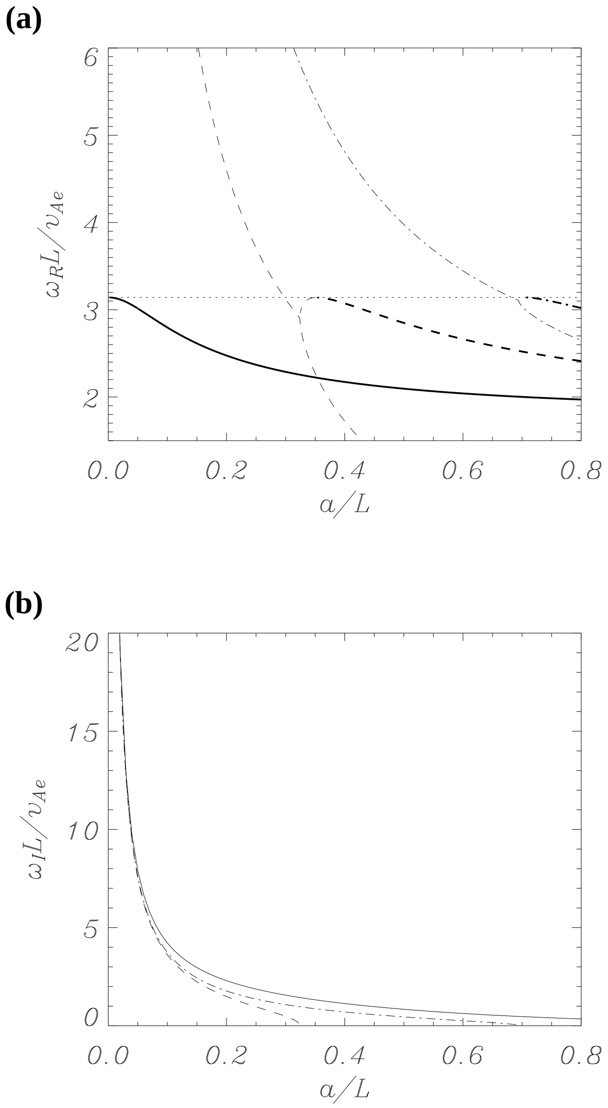

Figure 3.3: Dispersion diagram calculated from the numerical solution of the dispersion relations, Equations (3.10) and (3.11), for a slab model with density contrast $\rho_i/\rho_e = 3$ (Terradas et al., 2005a). Line styles follow from Figure 3.2: **(a)** variation of the real part of the normalised frequency, ω_R, versus the normalised half loop width a, for the fundamental kink mode (solid line), the fundamental sausage mode (dashed line) and the first kink harmonic (dot-dashed line). The cut-off frequency, ω_c, is represented by a horizontal dotted line. **(b)** Variation of the imaginary part of the normalised frequency, ω_I, versus the normalised loop half-width.

3.2 Two slab model

The situation is similar to that of a single slab, but now we consider a system of two slabs whose centres are separated by a distance d, so the distance between their inner edges is $d - 2a$. The density profile is (see Figure 3.4)

$$\rho(x) = \begin{cases} \rho_e, & \text{if } 0 \leq |x| < d/2 - a, \\ \rho_i, & \text{if } |x \pm d/2| \leq a, \\ \rho_e, & \text{if } |x| > d/2 + a. \end{cases} \tag{3.14}$$

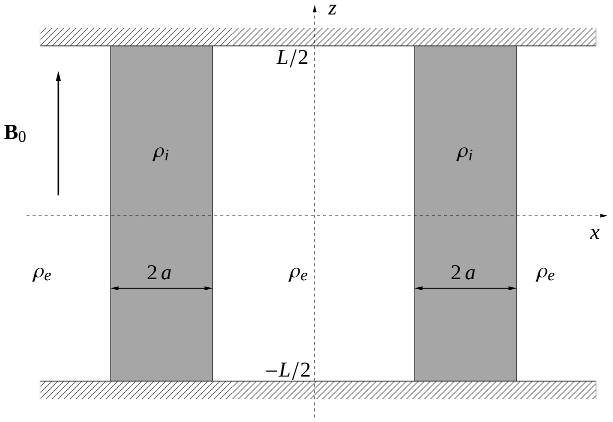

Figure 3.4: Sketch of the two slab system. The shaded area represents the density enhancement of the two slabs while the hatched area represents the photospheric medium, that fixes the feet of the slabs and produces the line-tying effect.

The wave equation is given by Equation (3.2), where the Alfvén velocity is

$$v_A(x) = \begin{cases} v_{Ae} = \frac{B_0}{\sqrt{\mu\rho_e}}, & \text{if } 0 \leq |x| < d/2 - a, \\ v_{Ai} = \frac{B_0}{\sqrt{\mu\rho_i}}, & \text{if } |x \pm d/2| \leq 2a, \\ v_{Ae} = \frac{B_0}{\sqrt{\mu\rho_e}}, & \text{if } |x| > d/2 + a. \end{cases} \tag{3.15}$$

3.3 Normal mode analysis

Normal mode solutions to Equation (3.2) in a uniform medium have a dependence of the form $e^{i(k_x x - \omega t)}$, with $k_x^2 = \omega^2/v_A^2 - k_z^2$ as in the previous Section (Equation 3.3). In the present structure, the eigenfunctions have the form $v_x(x,t) = v_x(x)\, e^{-i\omega t}$, with

$$v_x(x) = \begin{cases} A\, e^{k_e x}, & \text{if } x < -d/2 - a, \\ B_1\, e^{-ik_i x} + B_2\, e^{ik_i x}, & \text{if } -d/2 - a \le x \le -d/2 + a, \\ C_1\, e^{k_e x} + C_2\, e^{-k_e x}, & \text{if } |x| < d/2 - a, \\ D_1\, e^{-ik_i x} + D_2\, e^{ik_i x}, & \text{if } d/2 - a \le x \le d/2 + a, \\ E\, e^{-k_e x}, & \text{if } x > d/2 + a. \end{cases} \tag{3.16}$$

Here k_e and k_i are the external and internal wavenumbers, defined by Equations (3.5), (3.6) and (3.7).

We impose the boundary conditions given by Equation (3.8) and apply the same procedure as for the single slab model discussed before. Now the boundary conditions are applied on the four interfaces located at $x = -d/2 \pm a$ and $x = d/2 \pm a$, thus obtaining four equations for the velocity and four equations for its x-derivative. These equations form a homogeneous linear system of eight equations with eight unknowns, namely A, B_1, B_2, C_1, C_2, D_1, D_2, E. For this system of equations to have a non-trivial solution, its determinant must be zero. This gives the dispersion relation, which appears as a product of two factors. One of these factors must vanish, which leaves us with the following expressions,

$$\left(k_e^2 + k_i^2\right) \tan(2\,a\,k_i) - e^{(d-2\,a)\,k_e} \left[\tan(a\,k_i) - \frac{k_e}{k_i}\right] \left[\tan(a\,k_i) + \frac{k_i}{k_e}\right] = 0, \tag{3.17}$$

or

$$\left(k_e^2 + k_i^2\right) \tan(2\,a\,k_i) + e^{(d-2\,a)\,k_e} \left[\tan(a\,k_i) - \frac{k_e}{k_i}\right] \left[\tan(a\,k_i) + \frac{k_i}{k_e}\right] = 0. \tag{3.18}$$

As in Section 3.1.1 we display some velocity profiles, Figure 3.5, and a dispersion diagram, Figure 3.6. There are two kinds of normal modes: solutions to Equation (3.17) are symmetric with respect to $x = 0$ and so both slabs move in phase (see Figures 3.5a and 3.5b). On the other hand, solutions to Equation (3.18) are antisymmetric with respect to $x = 0$ and, both slabs move in antiphase (see Figures 3.5c and 3.5d). In addition, Figure 3.5 shows that normal modes can either be trapped (as in panels a, b and d) or leaky (as in panel c). Trapped modes attain their maximum amplitude in or near the slabs, but leaky modes present oscillations growing in amplitude as $x \to \pm\infty$ (see Section 3.1.1).

We reproduce the analysis of Section 3.1.1 for the solutions of the dispersion relations, Equations (3.17) and (3.18). We solve these equations and calculate ω for different values of the slab separation, d, for the fundamental and first harmonic of the symmetric and antisymmetric modes (see Figure 3.6a for the real part of the frequency and Figure 3.6b for the imaginary part). The frequency of trapped modes is real and smaller than the external cut-off frequency. The symmetric mode (solid line in Figure 3.6) is trapped for all distances. On the other hand, the fundamental antisymmetric mode (dashed line) is leaky for small values of d/L and, as d/L is increased, it crosses the external cut-off frequency and bifurcates in two branches. For larger distances ($d/L \gtrsim 1$) the upper branch

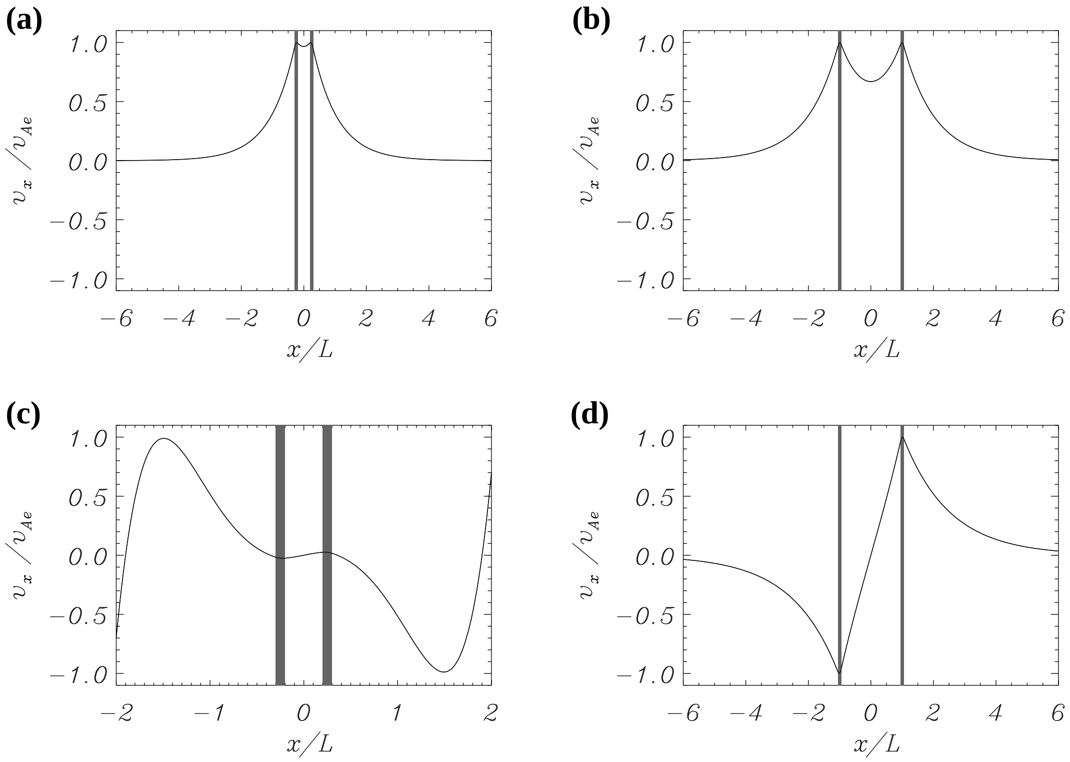

Figure 3.5: Velocity profile, $v_x(x)$, for the fundamental symmetric mode (upper row) and the fundamental antisymmetric mode (lower row) for a slab half-width $a = 0.05L$ and a density enhancement $\rho_i/\rho_e = 3$. The left and right columns correspond to a distance between slabs $d = 0.5L$ and $d = 2L$, respectively. **(a)** and **(b)** show that the symmetric mode is trapped for the two separations, but **(c)** and **(d)** indicate that the antisymmetric mode becomes leaky for small separations or distances between slabs. The shaded surface corresponds to the density enhancement of the slabs.

reaches the external cut-off and the mode becomes trapped (thick dashed line). The other harmonics (symmetric and antisymmetric) have the same behaviour but in the domain plotted in Figure 3.6 they do not cross the cut-off line and are leaky. The imaginary part of the frequency decreases for increasing distances. This implies that the damping time increases with the slabs separation, d.

The behaviour of solutions for small and large separations between slabs can be derived from Equations (3.17) and (3.18). For d slightly larger than $2a$ ($d \gtrsim 2a$), we have $e^{(d-2a)\,k_e} \approx 1$ and from Equation (3.17) we recover the sausage mode dispersion relation for one slab,

$$\tan(2ak_i) = -\frac{k_i}{k_e}, \tag{3.19}$$

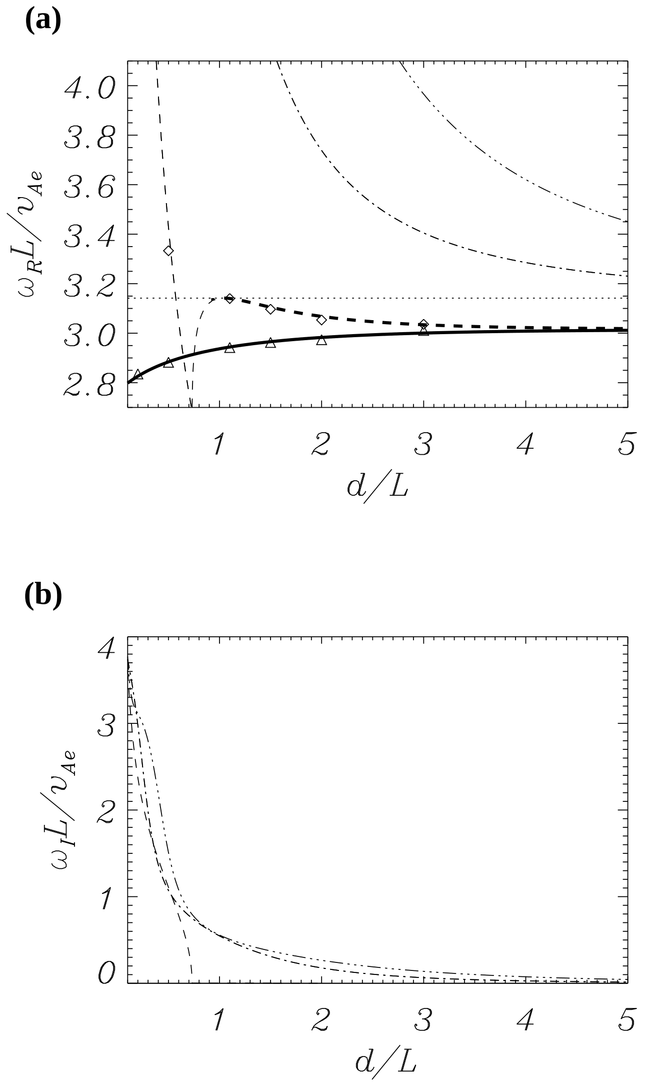

Figure 3.6: Equivalent to Figure 3.3 for two slabs. **(a)** Real part, ω_R and **(b)** imaginary part, ω_I, of the frequency as functions of the separation, d, for a density enhancement $\rho_i/\rho_e = 3$ and a half-width $a = 0.05L$. The line styles correspond to the fundamental symmetric mode (solid line), the fundamental antisymmetric mode (dashed line), the first symmetric harmonic (dot-dashed line) and the first antisymmetric harmonic (three-dot-dashed line). The dotted line is the external cut-off frequency, ω_{ce}. Thick curves represent trapped modes while thin lines correspond to leaky modes. $\omega_R L/v_{Ae}$ and $\omega_I L/v_{Ae}$ are normalised frequencies. In **(a)** the calculated frequency from the time-dependent results for the symmetric (triangles) and antisymmetric (diamonds) modes is also represented.

and from Equation (3.18) the kink mode dispersion relation for one slab,

$$\tan(2ak_i) = \frac{k_e}{k_i}. \tag{3.20}$$

These expressions are identical to Equations (3.10) and (3.11), although now a is replaced by $2a$. Therefore, for the minimum separation between slabs, $d = 2a$, the system of two slabs is equivalent to a single slab but with half-width $2a$. We also see that the symmetric mode tends to the kink mode for $d \to 2a$ and the antisymmetric mode tends to the sausage mode. Hence, we expect a gradual transition from the solutions of one slab to those of a system of two slabs as the separation is increased.

For very large separation between slabs ($d \ll a$), we have $e^{(d-2a)\,k_e} \to \infty$ and Equations (3.17) and (3.18) lead to

$$\left[\tan(a\,k_i) - \frac{k_e}{k_i}\right]\left[\tan(a\,k_i) + \frac{k_i}{k_e}\right] = 0. \tag{3.21}$$

This is the dispersion relation of one slab (see Equation 3.9). This is the expected behaviour, too, since for large separations the interaction between both slabs is negligible and they behave as independent loops.

3.4 Time-dependent analysis: numerical simulations

Normal modes provide with information about the oscillatory state and parameters of the system, but coronal oscillations are often produced by an impulsive event and time dependent simulations are more appropriate to describe the evolution of the system. In the case of a single slab (Terradas et al., 2005a) an impulsive disturbance leads, after a time of the order of the Alfvén transit time across the slab, to a distribution of its energy into one or more normal modes. The question that arises is how this picture will be modified for a two slab structure: after an impulsive event, does the system oscillate in a normal mode (or a sum of some normal modes) or do the modes of a single slab appear?

To study the effect of an arbitrary initial perturbation we consider the system of two slabs with a typical density enhancement ($\rho_i/\rho_e = 3$) and a typical slab half-width ($a = 0.05L$). Perturbations with different velocity profiles are excited.

To solve Equation (3.2) numerically, the code PDE2D (Sewell, 2005) based on finite elements, has been used. This code, which gives a numerical approximation to $v_x(x,t)$, makes use of a second order implicit Crank-Nicholson method with adaptive time step control. Since we consider a finite numerical domain, reflections at the domain boundaries may affect the dynamics of the system of slabs. We have solved this problem by locating the edges of the numerical domain far from the two slabs. Given that the size of the domain is much larger than the loop thickness, a non-uniform grid with 4000 grid points in the full domain, 45 of them located inside each slab ($|x \pm d/2| \leq a$), has been used. In addition, we have made sure that the artificial diffusion introduced by the numerical scheme is small enough. This is a critical point since the artificial damping can be larger than the physical damping, in our case arising from energy leakage, and may lead to the wrong interpretation of the results. We have performed different simulations by increasing the number of grid points and have found that the solutions converge, which is an indication that numerical diffusion does not affect considerably the results. In addition, we have checked that the same results are obtained by solving the initial-value problem with a standard explicit method based on finite differences.

The initial condition is the sum of two Gaussian profiles centred in each of the slabs,

$$v_x(x, t = 0) = \left\{ A \exp\left[\left(\frac{x - d/2}{\Delta}\right)^2\right] + B \exp\left[\left(\frac{x + d/2}{\Delta}\right)^2\right]\right\}, \tag{3.22}$$

where Δ is the width of the Gaussian function and A and B are the amplitudes of the right and left Gaussian pulses, respectively. Firstly, we generate two types of initial conditions, namely a symmetric initial pulse ($A = B = 1$) and an antisymmetric initial pulse ($A = -B = 1$). Later, we excite the system with an individual pulse with $A = 1$ and $B = 0$. In all the performed numerical simulations, the width of the initial pulses is $\Delta = 0.1L$.

3.4.1 Symmetric or antisymmetric excitation

Let us start with the symmetric initial condition and a separation between slabs $d = 0.5L$. To see which normal modes can be excited, we only need to care about the symmetric ones, since the antisymmetric modes are not excited because their symmetry is opposite to that of the initial perturbation. So we inspect the dispersion diagram (Figure 3.6) and see that for $d = 0.5L$ there is only a symmetric trapped mode (the fundamental symmetric mode) and infinite leaky symmetric modes (of which only one is shown in this plot). The results of the simulation are displayed in Figure 3.7, where we have plotted the velocity, v_x, as a function of x for different times (t is given in units of the external Alfvén transit time, $\tau_{Ae} = L/v_{Ae}$). The initial perturbation produces travelling disturbances to the left and right and these disturbances show some dispersion as they propagate: short wavelengths are at the front and long wavelengths at the back of the travelling disturbances (Figures 3.7c and 3.7d). A comparison of Figures 3.5a and 3.7d in the range $-5 \le x \le 5$ indicates that, for long times, the system settles down into the trapped mode. To gain more insight into the time evolution we plot the velocity at the centre of the right slab (i.e. at $x = d/2$) in Figure 3.8a. In this figure we see clearly two phases, a transient (for $0 \le t/\tau_{Ae} \lesssim 3$) and an oscillatory phase (for $t/\tau_{Ae} \gtrsim 3$). The transient is produced by two effects: firstly, perturbations reflect and refract at the two slabs until the energy contained in the initial impulse is transferred into the normal modes. This phase has a duration, which we call the relaxation time, of the order of a few times the Alfvén travel time between the two slabs, i.e. a few times $0.5\tau_{Ae}$; secondly, the excited leaky modes carry their energy towards $x \to \pm\infty$ and so decay in a time of the order of τ_I. In Terradas

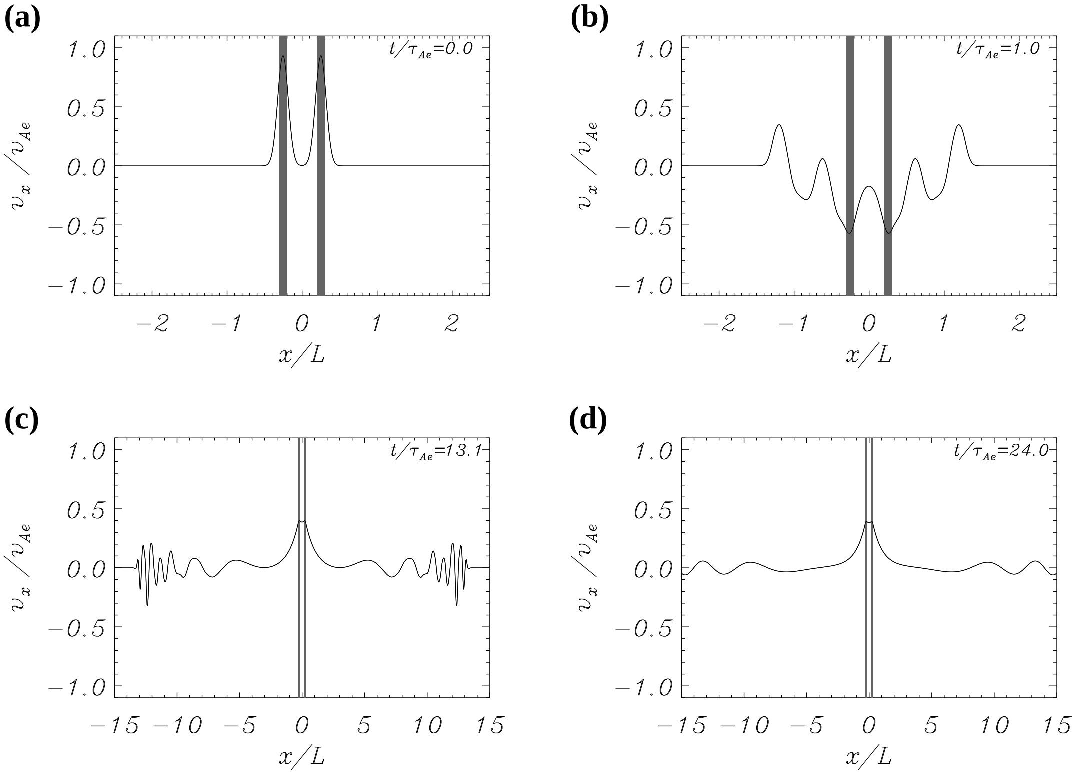

Figure 3.7: Time-evolution of the velocity, v_x, for a distance between slabs $d = 0.5L$ and a symmetric initial impulse with $A = B = 1$. The dashed areas show the location of the two slabs.

et al. (2005a) this phase was called the impulsive leaky phase. From Figure 3.6b we see that $\tau_I/\tau_{Ae} \simeq 1$ for the first leaky harmonic, which means that this mode damps out in a time comparable to the relaxation time. The very short duration of this and all other leaky modes makes them practically undetectable in Figure 3.8a. Further confirmation of this interpretation of Figure 3.8a is given by its power spectrum (Figure 3.8b), which displays a single power peak whose frequency exactly matches that of the trapped symmetric mode, while the power at the frequencies of leaky modes is negligible. As a conclusion, the trapped fundamental symmetric mode is excited in this simulation and there is a good agreement in the frequency and velocity profile with the normal mode results. If leaky modes are excited, they cannot be detected because of their very rapid damping.

Next, we perturb the same system with an antisymmetric initial condition, so now only the antisymmetric normal modes are excited. The results of the simulation, which again show the propagation of perturbations in both directions along the x-axis, are displayed in Figure 3.9. In this case the amplitude of the oscillations in both slabs decreases in time because all antisymmetric modes are leaky for the selected separation between slabs ($d/L = 0.5$). In Figure 3.10a the velocity measured in the centre of the right slab, $x = d/2$, is plotted. After the relaxation time, which again is of the order of $3\tau_{Ae}$, the signal

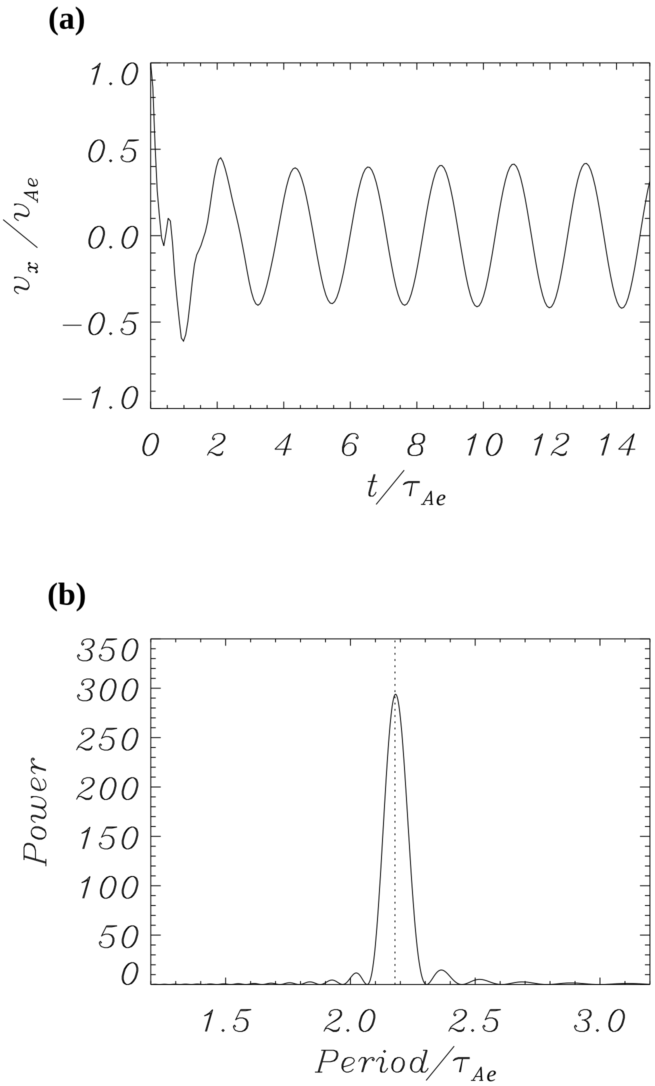

Figure 3.8: **(a)** Measured velocity at the centre of the right slab, $x = d/2$, for the symmetric initial perturbation of Figure 3.7. After a short transient the system oscillates in a trapped mode, with period close to $2\tau_{Ae}$, and the oscillatory amplitude remains unchanged. **(b)** As expected, the periodogram of the signal in **(a)** features a large power peak at a period around $2\tau_{Ae}$. There is an excellent agreement between the period of this peak and the period of the normal mode obtained from Equation (3.17) (dotted line). The periodogram lacks other power peaks.

is an attenuated oscillation, as expected for leaky modes. In Figure 3.10b we see the periodogram of this signal, where the dashed line gives the theoretical frequency of the fundamental leaky antisymmetric mode (from Figure 3.6) and as in the previous case coincides with the peak of the power spectrum. Nevertheless, now the power peak is broad due to the exponential attenuation of the signal. Regarding the spatial velocity profile, it is

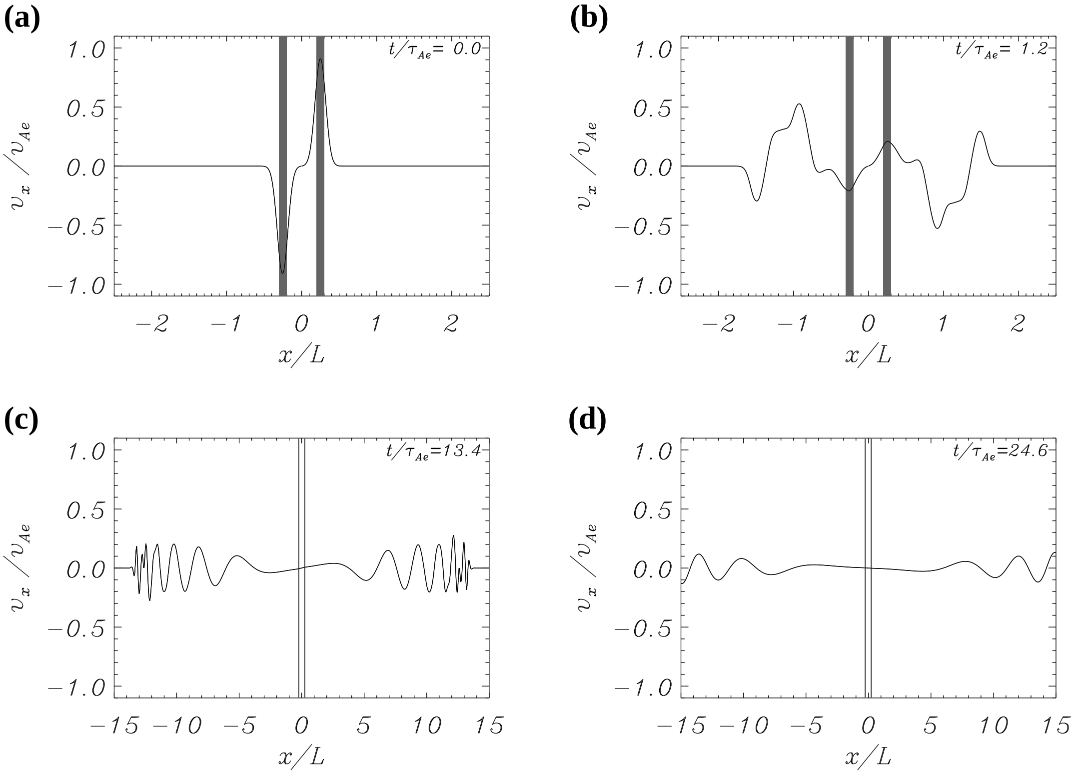

Figure 3.9: Time-evolution of the velocity, v_x, for a distance between slabs $d = 0.5L$ and an antisymmetric initial impulse with $A = -B = 1$. The dashed areas show the location of the two slabs.

not easy to compare the results of the simulation with those of the normal mode analysis, but still Figures 3.9c and 3.9d bear some resemblance with Figure 3.5c. We conclude that the considered antisymmetric disturbance mostly excites the fundamental antisymmetric leaky mode.

We next repeat this analysis for different slab separations and obtain an estimation of the real part of the frequency of the normal mode, ω_R, from the power spectrum of the simulations. With these data we have superimposed in Figure 3.6a, the value of ω_R calculated from the numerical simulations (see triangles and diamonds) on top of the theoretical dispersion diagram. The agreement is outstanding for all values of d/L, so we conclude that when the system is excited with a symmetric or antisymmetric initial condition, it later oscillates in a normal mode predicted by the theory. As a corollary, the system acquires a collective oscillation, given by a normal mode and does not oscillate with the modes of an individual slab.

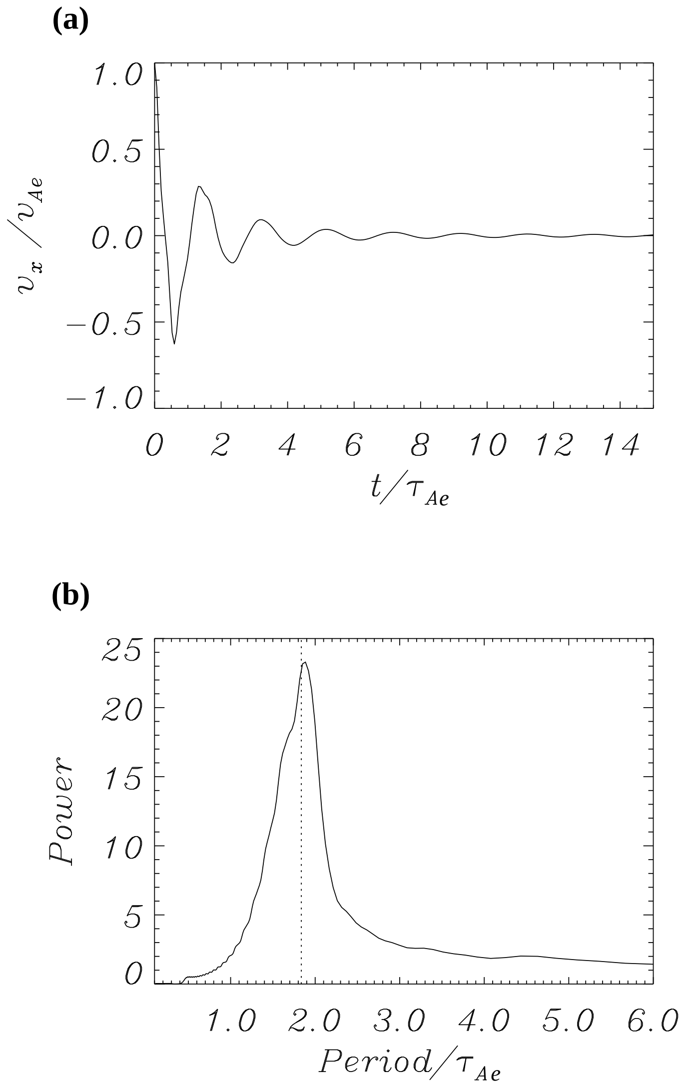

Figure 3.10: **(a)** Measured velocity at the centre of the right slab, $x = d/2$, for the antisymmetric initial perturbation of Figure 3.9. After a short transient the system oscillates in a leaky mode and so the perturbation attenuates exponentially. **(b)** The periodogram of the signal in **(a)** has a power peak whose period is in excellent agreement with that of the normal mode obtained from Equation (3.18) (dotted line). The periodogram lacks other power peaks.

3.4.2 Arbitrary excitation

Now, the system is excited using an initial condition with no particular symmetry about $x = 0$. The initial condition that we consider is a Gaussian pulse centred in the right slab. This initial pulse is given by Equation (3.22) with $A = 1$, $B = 0$ and, therefore, can be decomposed into the sum of a symmetric and an antisymmetric excitation. Since

Equation (3.2) is linear, we expect that this kind of initial disturbance will give rise to a superposition of the solutions arising from the corresponding symmetric and antisymmetric excitations. In this Section we consider the slab separations $d = 0.5L$ and $d = 2L$.

Firstly, we consider the case $d = 0.5L$ (Figure 3.11), which implies that the initial condition (Figure 3.11a) is half the sum of the symmetric and antisymmetric initial conditions previously seen. During the initial stages of the temporal evolution (Figures 3.11b and 3.11c) v_x has no definite symmetry with respect to $x = 0$ because the solution is the sum of the symmetric and antisymmetric modes. Let us recall that these modes are the fundamental symmetric and the fundamental antisymmetric, which are trapped and leaky, respectively. As a consequence, after some time (Figure 3.11d) the antisymmetric mode amplitude is negligible in the vicinity of the slabs and the system oscillates in a symmetric manner. In Figure 3.12 the time dependence of the velocity, v_x, is plotted in both slab centres. Because of the superposition of the antisymmetric leaky mode and the symmetric trapped mode both slabs oscillate with different phases and amplitudes until $t \simeq 10\tau_{Ae}$. Then, according to Figure 3.10a, the antisymmetric perturbation extinguishes and the two slabs oscillate in phase. The periodogram of the two curves in this plot coincides with that of Figure 3.8b because the leaky mode is a very short duration signal and so its contribution to the periodogram is very small. In addition, Figure 3.12 gives us a way of recovering the signals in Figures 3.8a and 3.10a. By summing the signals in Figure 3.12 the contribution of the antisymmetric modes vanishes because they have the same amplitude and opposite sign in the slab centres, so we are left with the symmetric mode, i.e. with Figure 3.8a. In the same manner, the difference of the signals in Figure 3.12 leads to Figure 3.10a. We thus conclude that the initial condition excites the symmetric and antisymmetric modes, as expected, and that the system oscillates in its collective modes and not in the modes of a single slab.

Secondly, we perturb the system with the same initial condition but now the distance between the slab centres is $d = 2L$. As can be appreciated in Figure 3.6, this choice of the slab separation results in the fundamental antisymmetric mode becoming trapped. The evolution of the system is again presented for different times (Figure 3.13) and, although after some time the two slabs seem to move in phase (Figure 3.13b), in a later stage the right slab has given all its energy to the left slab and so is motionless (Figure 3.13c). At an even later time (Figure 3.13d) the picture is just the opposite, with the left slab fixed and the right slab in motion. Hence, the two slabs are continuously exchanging energy and the transition between the states depicted in Figures 3.13c and 3.13d takes place through a situation similar to that in Figure 3.13b, where both slabs are oscillating. This behaviour is repeated periodically. This phenomenon is more clearly represented in Figure 3.14a, where the velocity, v_x, is plotted at the centre of both slabs. Contrary to the behaviour in the stationary regime for symmetric or antisymmetric initial perturbations (Figures 3.8a and 3.10a), the oscillations do not attain a constant amplitude, but they instead display a sinusoidal modulation. This is a well known collective beating phenomenon, like, for instance, that of two weakly coupled oscillators. It is due to the simultaneous excitation of the symmetric and antisymmetric modes with alike frequencies. These frequencies are re-

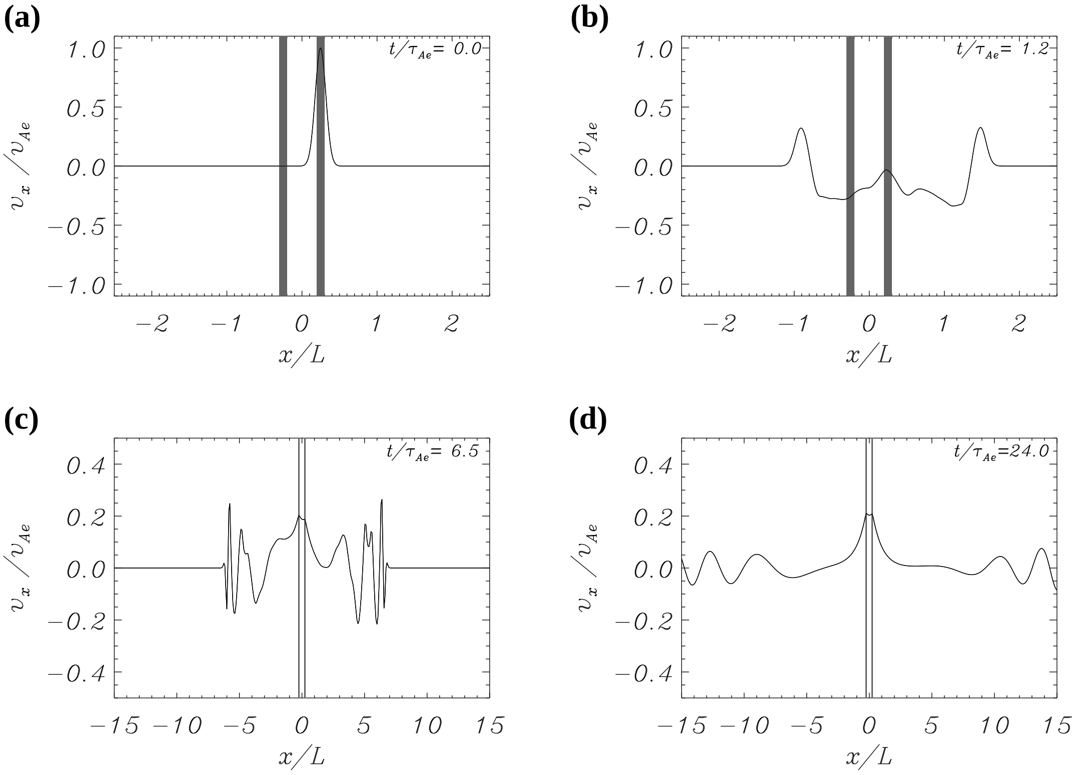

Figure 3.11: Time-evolution of v_x for $d = 0.5L$ and a non-symmetric initial excitation with $A = 1$ and $B = 0$. The dashed areas show the location of the two slabs.

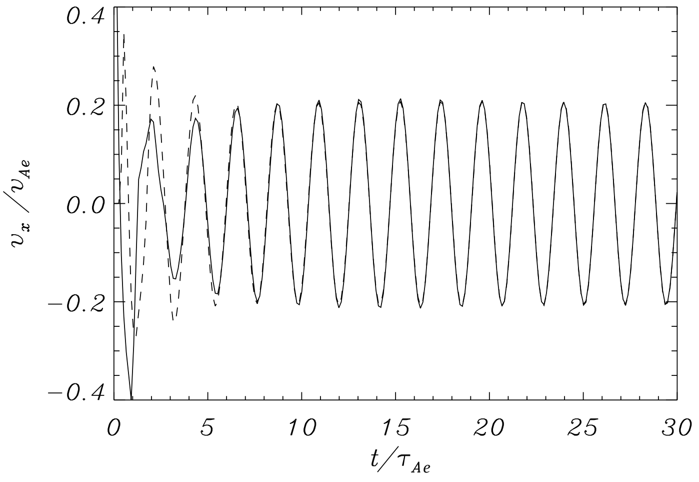

Figure 3.12: v_x measured at the centres of the slabs for the simulation shown in Figure 3.11. The solid and dashed lines correspond to the right and left slabs, respectively.

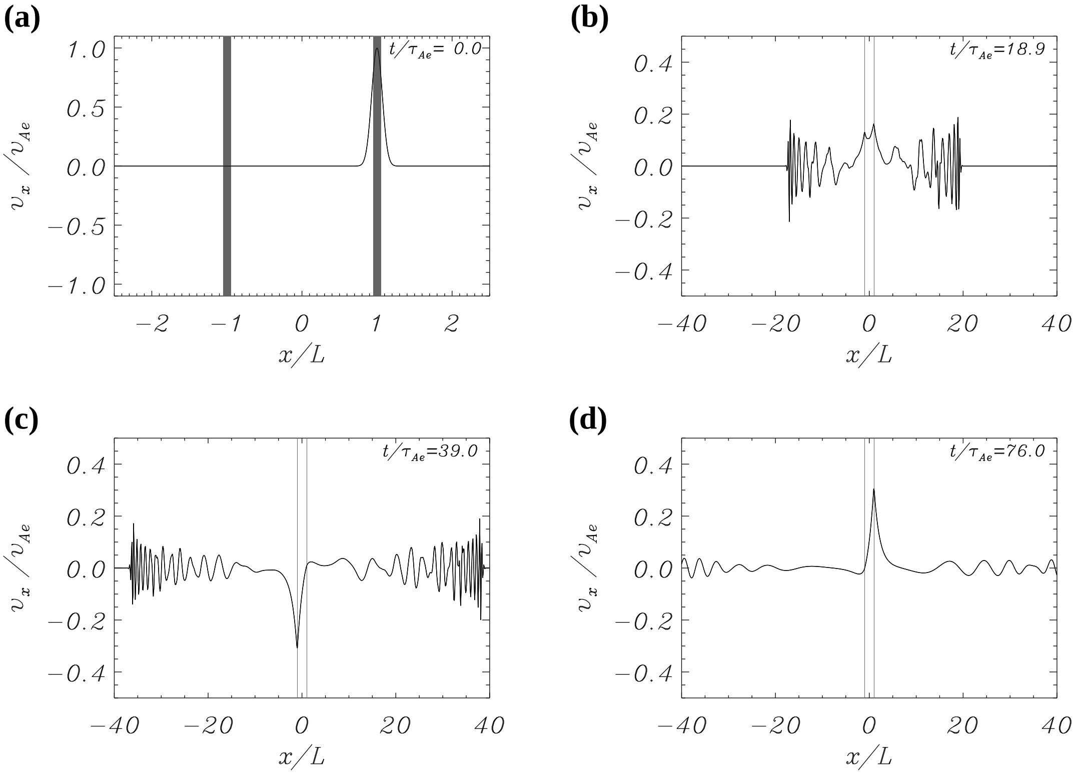

Figure 3.13: Time evolution of v_x for $d = 2L$ and a non-symmetric initial disturbance with $A = 1$ and $B = 0$. The dashed areas show the location of the two slabs. Note the interchange of energy between the two slabs in the last two frames.

covered from the power spectrum of the velocity at the centre of right slab (Figure 3.14b), which shows two power peaks with periods almost identical to those of the fundamental antisymmetric mode ($2.048\tau_{Ae}$) and the fundamental symmetric mode ($2.106\tau_{Ae}$). The corresponding frequencies are ($3.068 v_{Ae}/L$) and ($2.983 v_{Ae}/L$), respectively. This match between the frequency of the normal modes and the oscillations in the numerical simulation is also evident in Figure 3.6a. Finally, both peaks in the power spectrum have similar height, which allows us to conclude that the two normal modes have been excited with similar amplitude.

In fact, from Figure 3.6 we see that there exists a range of slab separations for while both trapped modes, i.e. the fundamental symmetric and antisymmetric, coexist and possess very close frequencies. In this range of separations, which goes from $d \approx 1.04L$ to infinity, the beating appears when non-symmetric initial disturbances are applied. Hereafter we refer to this range of d as the band of beating and to the separation where the band starts as the minimum distance of beating (d_{min}). Then, our analysis yields $d_{min} \simeq 1.04L$ for $a/L = 0.05$ and $\rho_i/\rho_e = 3$. In Section 3.5.1, we shall study the beating properties for other density ratios and will show that this band can extend to even smaller separations.

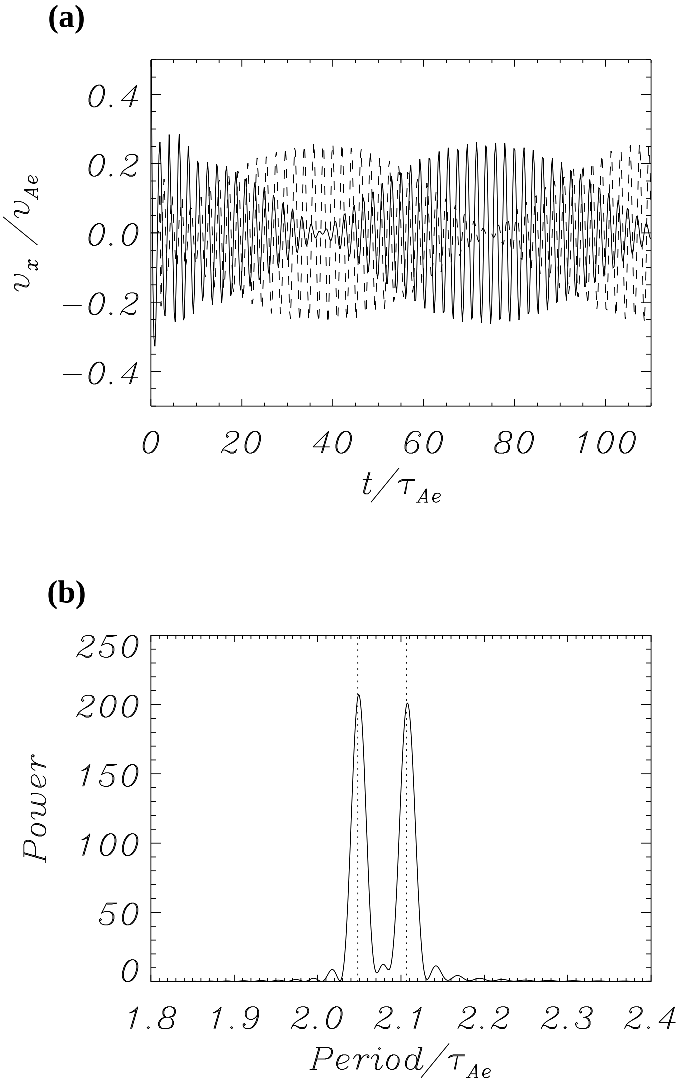

Figure 3.14: **(a)** v_x measured at the centre of the slabs for the simulation shown in Figure 3.13. The solid and dashed lines correspond to the right and left slabs, respectively. **(b)** Power spectrum of the previous signal (solid line). The two vertical dotted lines indicate the periods of the fundamental antisymmetric mode (at $2.048\tau_{Ae}$) and the fundamental symmetric mode ($2.106\tau_{Ae}$).

3.5 Analytical study of beating

For a slab separation in the beating band the system oscillates in a superposition of the trapped symmetric and antisymmetric modes. Then, in the stationary state, the system behaves as

$$v_x(x,t) = \alpha_s f_s(x)\cos(\omega_s t + \phi_0) + \alpha_a f_a(x)\cos(\omega_a t), \tag{3.23}$$

where the subscripts s and a refer to the symmetric and antisymmetric modes, respectively. The spatial functions $f_s(x)$ and $f_a(x)$ are the corresponding eigenfunctions, for instance the velocity profiles of Figures 3.5b and 3.5d (for $d/L = 2$). The parameters α_s and α_a are scaling factors that correspond to the amplitude of the normal modes.

We define

$$\Omega_+ = \frac{\omega_a + \omega_s}{2}, \tag{3.24}$$

$$\Omega_- = \frac{\omega_a - \omega_s}{2}, \tag{3.25}$$

and

$$f_1(x) = \alpha_a f_a(x) + \alpha_s f_s(x), \tag{3.26}$$

$$f_2(x) = \alpha_a f_a(x) - \alpha_s f_s(x). \tag{3.27}$$

After some algebra we find

$$\begin{aligned} v_x(x,t) = {} & f_1(x)\cos(\Omega_+ t + \phi_0/2)\cos(\Omega_- t - \phi_0/2) \\ & - f_2(x)\sin(\Omega_+ t + \phi_0/2)\sin(\Omega_- t - \phi_0/2). \end{aligned} \tag{3.28}$$

We next consider

$$v_{x1}(x,t) = f_1(x)\cos(\Omega_+ t + \phi_0/2)\cos(\Omega_- t - \phi_0/2), \tag{3.29}$$

$$v_{x2}(x,t) = -f_2(x)\sin(\Omega_+ t + \phi_0/2)\sin(\Omega_- t - \phi_0/2), \tag{3.30}$$

so that Equation (3.28) can be written as

$$v_x(x,t) = v_{x1}(x,t) + v_{x2}(x,t). \tag{3.31}$$

We now focus on the situation that led to beating in Section 3.4.2, that is, a system with $d/L = 2$ and the two trapped modes excited with identical amplitude. Then $f_1(x)$ and $f_2(x)$ (see Figure 3.15) come from the eigenfunctions $f_s(x)$ and $f_a(x)$ of Figures 3.5b and 3.5d and the mode amplitudes are identical, so we take $\alpha_s = \alpha_a = 1$. In Figure 3.15 we see that $f_1(x)$ and $f_2(x)$ are peaked functions around the right and left slabs, respectively. Therefore, the function $v_{x1}(x,t)$, for example, is also relevant in the neighbourhood of the right slab and is negligible in the vicinity of the left one (the opposite applies to $v_{x2}(x,t)$). This confers an intrinsic meaning to these functions that, although not directly measurable, reproduce some features of the numerical simulations. For example, at $t_1 = 38.9\tau_{Ae}$ in the numerical simulation (Figure 3.13c) the left slab reaches its maximum velocity and so the main contribution to the analytical approximation of the velocity (Equation 3.31) comes through $v_{x2}(x,t_1)$, i.e. through $-f_2(x)$. For this reason, the spatial distribution of

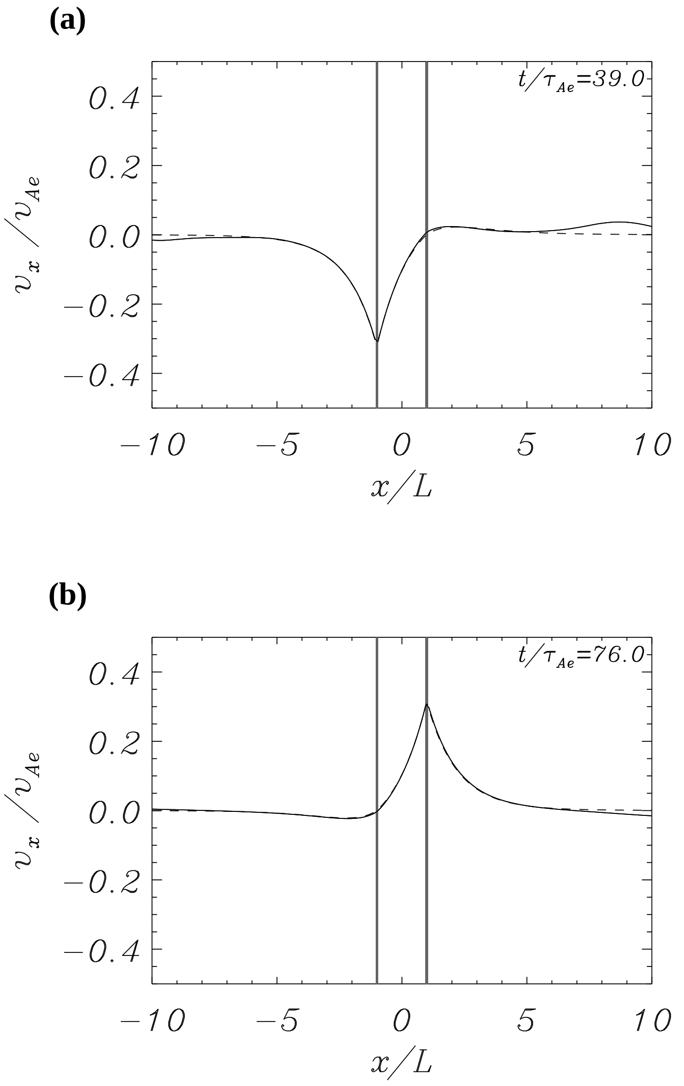

Figure 3.15: **(a)** and **(b)** The solid lines are a rescaled close-up view of Figures 3.13d and 3.13c, respectively. The dashed lines correspond to $f_1(x)$ and $f_2(x)$, respectively. The analytical approximation then reproduces the velocity profile obtained in the time-dependent simulation when a substantial amount of energy is concentrated in a single slab. The difference among both curves to the right and left of the slabs arises from the system not having reached the stationary state. For greater times the difference becomes smaller.

v_x in Figure 3.13c is very well reproduced by $-f_2(x)$, as can be seen in Figure 3.15b. Moreover, Figure 3.15a shows a similar agreement for the left slab at $t_2 = 75.9\tau_{Ae}$.

Given the spatial structure of v_{x1} and v_{x2}, the velocity in the centre of the right and left slabs obtained in the numerical simulations should be similar to $v_{x1}(x = d/2, t)$ and $v_{x2}(x = -d/2, t)$, respectively, so we have plotted these two functions together with their numerical counterparts (Figure 3.16). During the transient phase, the analytical approximation differs from the time-dependent results, but once the stationary state is reached (around $t = 12\,\tau_{Ae}$) the fitting is very good. The small difference between the two solutions in the stationary phase is caused by the slight amplitude difference of the two normal modes in the numerical simulation (see Figure 3.14b).

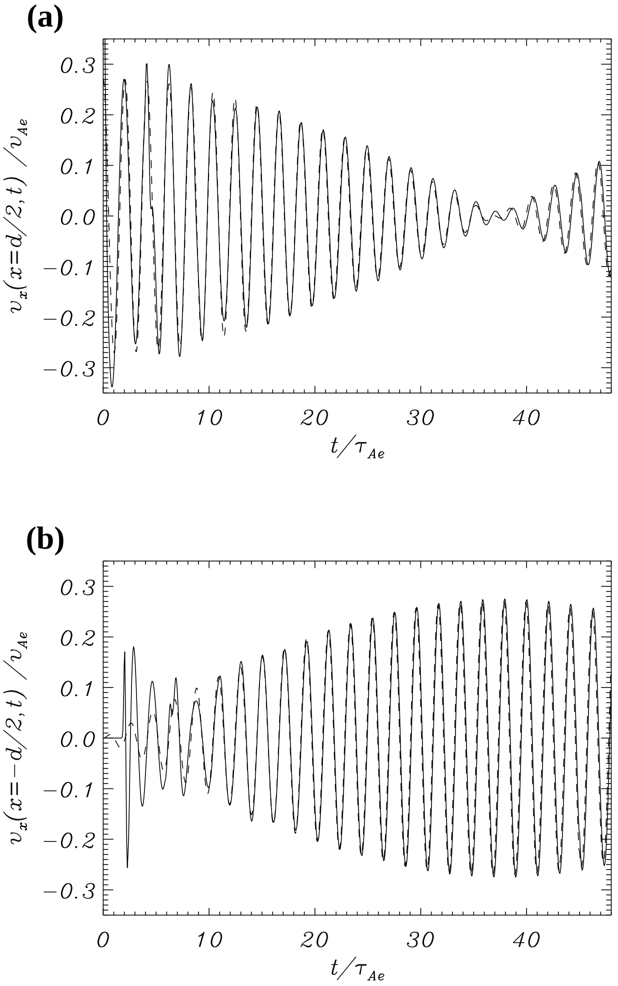

Figure 3.16: **(a)** Superposition of v_x measured at the centre of the right slab from the time-dependent numerical simulation (solid line) and the analytical approximation (dashed line). **(b)** The same for the left slab.

The beating oscillatory curve is a sinusoidal function multiplied by a sinusoidal envelope whose period (the beating period) is

$$T_{beating} = \frac{2\pi}{\Omega_-} = \frac{4\pi}{\omega_a - \omega_s}. \tag{3.32}$$

In addition, the period of oscillation of the system is

$$T = \frac{2\pi}{\Omega_+} = \frac{4\pi}{\omega_a + \omega_s}. \tag{3.33}$$

From the agreement found between the numerical simulations and the behaviour of v_{x1} and v_{x2} (see Figure 3.16) it is clear that the beating period and oscillation period calculated from these simulations is in perfect agreement with Equations (3.32) and (3.33) respectively.

In addition, it is useful to define the number of oscillations within a pulsation period, or beating factor (b_f),

$$b_f \equiv \frac{T_{beating}}{T} = \frac{\Omega_+}{\Omega_-} = \frac{\omega_a + \omega_s}{\omega_a - \omega_s}. \tag{3.34}$$

This factor is the number of peaks in a beating period. Small beating factors indicate strong beating behaviour. The beating factor is a good parameter to assess the beating phenomenon since it is easily measurable from the time-dependent results. In our example of Figure 3.14b, the number of peaks in a full beating period is approximately 71; this coincides with the theoretical beating factor given by the last expression, $b_f = 71.5$.

3.5.1 Parameter dependence of the beating

We investigate the beating properties of two identical slabs with different separations and density contrasts (the slabs width is held fixed and given by $a/L = 0.05$). In the previous Section we have seen that the dispersion relation allows us to extract information about the beating with the help of Equations (3.32), (3.33) and (3.34). For this reason we start plotting the real and imaginary parts of the frequency as functions of d for different values of ρ_i/ρ_e (see Figure 3.17). In these plots we can appreciate that the minimum distance of beating (i.e. the slab separation for which the fundamental antisymmetric mode transforms from leaky into trapped) decreases as the density ratio increases. This means that denser slabs can display beating for smaller separations. The oscillatory period obtained from Equation (3.33) is plotted in Figure 3.18a. For all the considered values of ρ_i/ρ_e, the oscillatory period is more or less independent from the slab separation when this quantity is larger than the length of the loops. Nevertheless, for $d < L$ (and for sufficiently high values of the density contrast, like for example $\rho_i/\rho_e = 8$ or 10) the oscillatory period decreases as the separation is reduced.

Another two parameters worth studying are the beating period, $T_{beating}$, and the beating factor, b_f, extracted from the dispersion relation data and Equations (3.32) and (3.34). These parameters are plotted in Figures 3.18b and 3.18c, respectively. We see that the beating period grows to infinity with d/L, which is the expected behaviour of two slabs that tend to oscillate independently. On the other hand, we see that for small slab separations b_f becomes rather small, implying that each beating period contains only a few

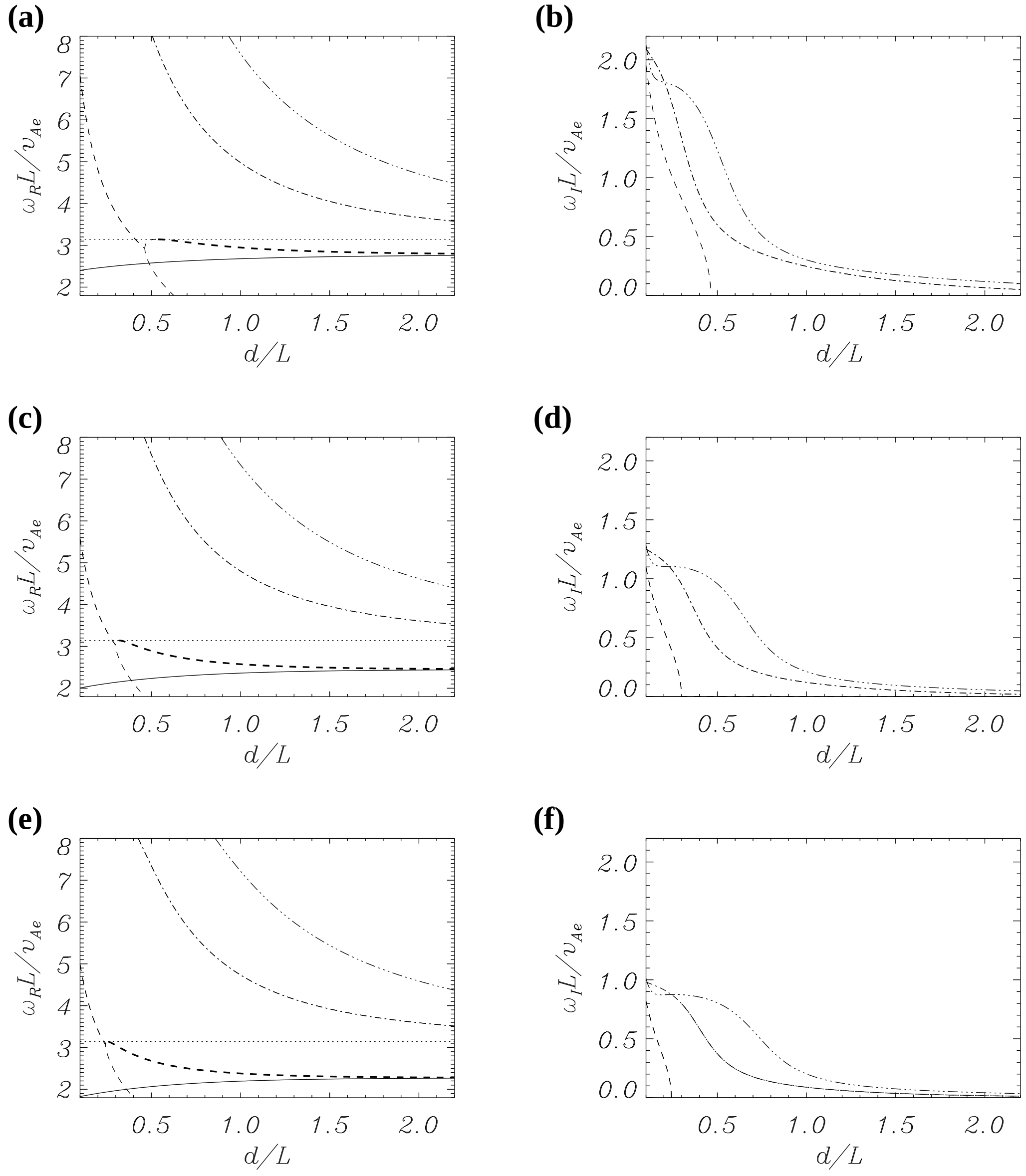

Figure 3.17: Plots of ω_R (left column) and ω_I (right column) as functions of the slab separation for different values of the density enhancement, ρ_i/ρ_e. **(a)** and **(b)** $\rho_i/\rho_e = 5$; **(c)** and **(d)** $\rho_i/\rho_e = 8$; **(e)** and **(f)** $\rho_i/\rho_e = 10$.

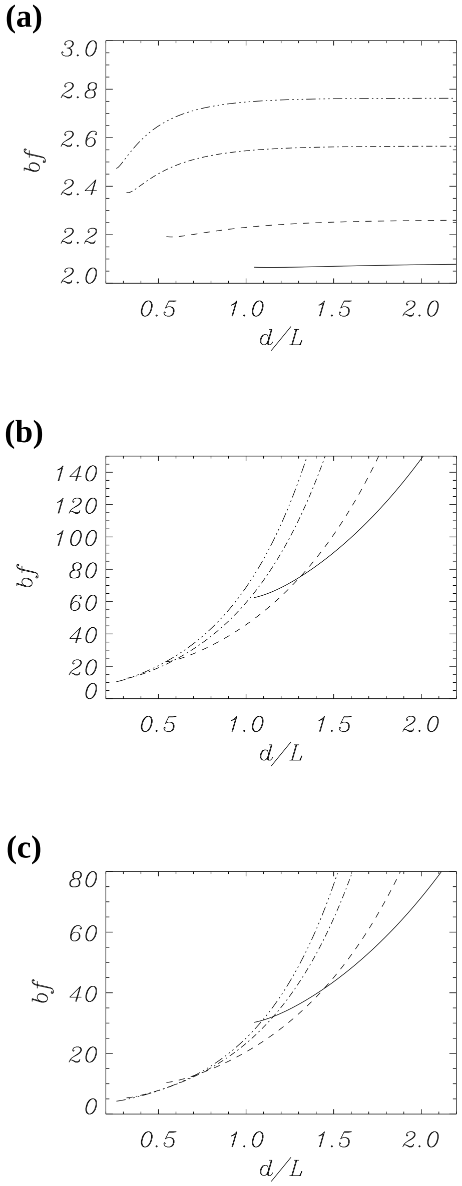

Figure 3.18: **(a)** Oscillatory period, **(b)** beating period and **(c)** beating factor, for the density contrasts $\rho_i/\rho_e = 3$ (solid line), $\rho_i/\rho_e = 5$ (dashed line), $\rho_i/\rho_e = 8$ (dot-dashed line) and $\rho_i/\rho_e = 10$ (three-dot-dashed line). Note that the curves start at the slab separation for which the fundamental antisymmetric mode transforms from leaky into trapped.

oscillatory periods. In particular, we find that slabs with high density contrast can show strong beating for small distances in comparison with slabs with small density contrasts.

3.6 Conclusions

In this Chapter we have studied the transverse oscillations of a single and two slab structures. We have found a strong interaction between loops in the two loops case. We have investigated the main features of a simple two slabs configuration (without gravity and curvature) and the results of this work can be summarised as follows:

1. We have analysed in detail the normal modes of the system. We have derived analytical expressions for the dispersion relation and have found, in agreement with the results of Díaz et al. (2005), that the symmetric mode is the only trapped mode for any distance between the slabs. On the other hand, the antisymmetric mode is leaky for small slab separations, but there exists a wide range of slab separations (larger than the critical distance) for which both trapped modes, i.e. the fundamental symmetric and antisymmetric, coexist and possess very close frequencies. Thus, trapped and/or leaky modes are excited according to the ratio d/L, but also according to the shape of the initial perturbation. It is then expected that initial disturbances with odd parity with respect to the centre of the system excite antisymmetric modes, whereas even disturbances lead to the excitation of symmetric modes.

2. We have also studied the temporal evolution of symmetric, antisymmetric and arbitrary excitations for a typical coronal loop with $a/L = 0.05$ and $\rho_i/\rho_e = 3$ and different slab separations. We have found that for symmetric disturbances and after a short transient all that remains is the undamped trapped mode, with energy confined to both slabs. On the other hand, since there are no trapped antisymmetric modes for slab separations smaller that d_{min}, an antisymmetric-like initial disturbance can only deposit energy in the leaky antisymmetric modes. The excitation of the fundamental antisymmetrical trapped mode is only possible for $d > d_{min}$.

3. An arbitrary excitation in the regime $d > d_{min}$ leads to the simultaneous excitation of the symmetric and antisymmetric modes. Since their frequencies are quite similar the oscillations do not attain a constant amplitude and show a sinusoidal modulation. This is a well known collective beating phenomenon which is completely equivalent to the behaviour of two weakly coupled oscillators. The frequency of oscillation of the system is $\frac{\omega_a+\omega_s}{2}$ with an envelope frequency or beating frequency $\frac{\omega_a-\omega_s}{2}$, where ω_a and ω_s are the antisymmetric and symmetric normal mode frequencies, respectively. The beating is the result of the continuous exchange of energy between the two slabs. We have also shown that slabs with high density contrast can show strong beating for small distances in comparison with slabs with small density contrasts.

It is important to remark that for moderate slab separations and any type of initial excitation, the system acquires a collective motion and does not oscillate with the modes of an individual slab. For this reason and specially in coronal arcades, formed by ensembles of loops, it seems much more appropriate to describe the oscillations in terms of collective motions instead of individual loop oscillations. Nevertheless, since our model is too simple, it has no sense to perform a quantitative comparison with the observations of loop oscillations in coronal arcades. However, it is worth noticing that the most clear example of such kind of oscillations (see Verwichte et al., 2004, Section 1.4) suggests that initially some loops of the arcade oscillate in phase while at later times the motions are in antiphase. This can be an indication of a beating phenomenon as a result of the collective oscillation of some of the loops. Unfortunately, it is not possible to extract more conclusions since the amplitude of the oscillations is quickly damped and only a few periods are observed. Additional observations of oscillations in coronal arcades will be very useful.

One of the most significant improvements to the model is to consider two cylindrical loops instead of Cartesian slabs. Since the eigenfunction of transverse oscillations in cylindrical tubes is much more confined than in slabs, the interaction between the tubes will be in general smaller and the beating time will be much longer. In addition, instead of the two modes of the Cartesian slab (symmetric and antisymmetric), the system of cylindrical tubes will have four different modes of oscillation. Two of these modes will be symmetric while the other two will be antisymmetric in the x- and y-directions. The normal mode analysis and the temporal evolution of two identical cylindrical flux tubes are the subject of the following Chapter.

Chapter 4

Two cylinder model[1]

In the previous Chapter we have studied transverse loop oscillations using the slab model. We have seen that loops interact strongly and their oscillations are affected by the presence of another loop. The loops of the system are able to interchange all their energy periodically according to their separation and initial excitation as well. The interaction between the loops takes place through the intermediate magnetised plasma and therefore it depends on the geometry of the model. Since the individual oscillations of a realistic curved loop are very similar to those of a straight tube (see Van Doorsselaere et al., 2004; Terradas et al., 2006), the cylindrical loop geometry provides a very good approximation for comparing with the observations. In this Chapter we extend our study to cylindrical geometry and show how two loops interact and how the coupling manifests in the system dynamics. This is the first investigation in which loop coupling in cylindrical geometry is considered.

The outline of this Chapter is as follows. In Section 4.1 we describe the transverse oscillations of a single cylindrical loop. In Section 4.2 the two loop model is presented. In Section 4.3 the normal modes of such a system are calculated and the frequencies and spatial distribution of the eigenfunctions are studied. The time-dependent problem is considered in Section 4.4, where the velocity and pressure field distribution are analysed for different incidence angles of an initial perturbation. In Section 4.5 the loop motions are studied and the beating is analysed. Finally, in Section 4.6 the results are summarised and the main conclusions are drawn.

4.1 Cylindrical model of a single loop

In order to understand the basic characteristics of transverse loop oscillations we first introduce the individual oscillations of a cylindrical flux tube, whose governing equations are the zero-β, ideal linear MHD equations for the magnetic pressure perturbation and

---

[1] The novel results in this Section have been published in Luna et al. (2008)

velocity field (Equations 2.29 and 2.30). In the zero-β limit the slow waves are absent and only the Alfvén and fast waves exist. In this Thesis we concentrate in the fast wave oscillations and in particular in the fast kink mode (however, it should be noted that this mode is highly Alfvénic, since the main restoring force is magnetic tension and the compression is very small; see Goossens et al., 2009, for detailed discussion). By solving Equations (2.29) and (2.30) it is possible to find the normal modes of the individual loop (see, e.g., Spruit, 1982; Edwin and Roberts, 1983; Cally, 1986). The model considered here is a cylindrical loop with length L and radius a (see Figure 4.1). We assume the following density profile

$$\rho_e(x,y) = \begin{cases} \rho_e, & \text{if } r > a, \\ \rho_i, & \text{if } r \leq a, \end{cases} \tag{4.1}$$

where x, y are the Cartesian coordinates in the direction perpendicular to the cylinder axis and r, defined by $r = \sqrt{x^2+y^2}$, is the radial distance from the point $\mathbf{r} = (x,y)$ to the loop centre. Now, ρ_i and ρ_e are the internal (loop) and external (coronal) densities respectively ($\rho_i > \rho_e$). Along this Chapter, we use a density contrast $\rho_i/\rho_e = 10$. The tube and the environment are permeated by a uniform magnetic field along the z-direction ($\mathbf{B} = B_0\mathbf{e_z}$). The Alfvén speed, $v_A = B_0/\sqrt{\mu\rho}$, takes the value v_{Ai} inside the loop and v_{Ae} in the surrounding corona ($v_{Ai} < v_{Ae}$).

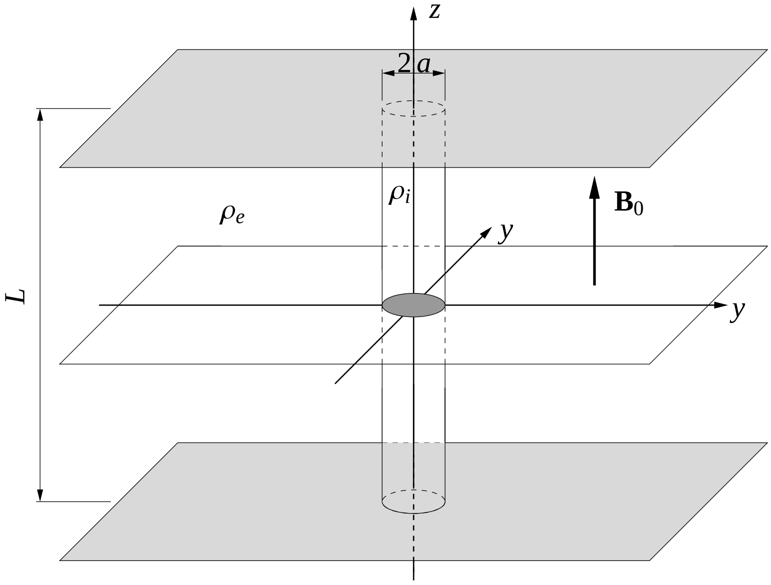

Figure 4.1: Sketch of the model, that consists of a straight cylinder immersed in the coronal medium. Both shaded planes represent the photosphere, where the loop feet are anchored. Hereafter the perturbed total pressure and the velocity fields are plotted in the xy-plane, shown as a white slice.

4.1.1 Normal mode analysis

We are seeking the normal modes of the straight flux tube. The appropriate coordinate system to describe the associated perturbations are the cylindrical coordinates (r, ϕ, z), in which the loop boundary is given by $r = a$. From the governing Equations (2.29) and (2.30) we see that it is enough to solve Equation (2.29) for the total pressure perturbation, p_T, and later to obtain the perturbed velocity, $\mathbf{v}_\perp$, from Equation (2.30). In cylindrical coordinates, the pressure perturbation can be written as

$$p_T = R(r)\,\Phi(\phi)\,Z(z)\,e^{-i\omega t}\,, \tag{4.2}$$

where we have assumed a harmonic time dependence with a frequency ω. Introducing these expressions in Equation (2.29) we obtain the following equations for the functions $R(r)$, $\Phi(\phi)$ and $Z(z)$,

$$\begin{aligned}
\frac{1}{r}\frac{\partial}{\partial r}\left(r\frac{\partial R}{\partial r}\right)+\left(\lambda_n^2-\frac{m^2}{r^2}\right)R &= 0\,, & (4.3)\\
\frac{\partial^2\Phi}{\partial\phi^2}+m^2\Phi &= 0\,, & (4.4)\\
\frac{\partial^2 Z}{\partial z^2}+\left(\frac{\omega^2}{v_A^2}-\lambda_n^2\right)Z &= 0\,, & (4.5)
\end{aligned}$$

where λ_n and m are two separation constants; the meaning of the subscript n will be clear below. The last two equations are easily solvable, yielding

$$\Phi_m(\phi) = e^{im\phi} \tag{4.6}$$

and

$$Z_p(z) = \sin(k_z\, z), \tag{4.7}$$

where $m, p \in \mathbb{Z}$ and $k_z = p\pi/L$ is the longitudinal wave number. We have applied the line-tying condition in Equation (4.7), assuming a zero pressure perturbation at the loop footpoints, i.e. $p_T(z = -L/2) = p_T(z = L/2) = 0$. From Equations (4.5) and (4.7) we find the following relation for the radial wave number λ_n,

$$\lambda_n^2 = \frac{\omega^2}{v_A^2} - k_z^2\,. \tag{4.8}$$

Equation (4.3) is the well-known Bessel differential equation of order m. The solution is written as a combination of Bessel functions,

$$R(r) = A_m J_m(\lambda_n r) + B_m Y_m(\lambda_n r), \tag{4.9}$$

or in terms of Hankel functions

$$R(r) = C_m H_m^{(1)}(\lambda_n r) + D_m H_m^{(2)}(\lambda_n r), \tag{4.10}$$

where the coefficients A_m and B_m or C_m and D_m are functions of λ_n, k_z and ω.

In order to find the normal modes of the cylindrical loop of Figure 4.1, we apply the boundary conditions (Equation 2.45) at the interphase between the internal loop medium and the external or coronal medium ($r = a$). These boundary conditions can be rewritten as

$$[p_T]_{r=a} = 0\,, \tag{4.11}$$

$$[v_r]_{r=a} = 0\,, \tag{4.12}$$

where v_r is the radial component of the velocity in cylindrical coordinates. From Equation (2.30) we find that the radial component of the velocity is

$$v_r = -\frac{i\,\omega}{\rho v_A^2 \lambda_n}\; p_T'\,, \tag{4.13}$$

where $p_T' = \frac{\partial p_T(\lambda_n r)}{\partial(\lambda_n r)}$ is the derivative with respect to the argument. In addition, we find the azimuthal component of the velocity,

$$v_\phi = \frac{m\,\omega}{\rho \lambda_n^2 v_A^2 r}\; p_T\,. \tag{4.14}$$

Inside the loop ($r \leq a$), the radial function $R(r)$ is

$$R_m^{(i)}(r) = A_m J_m\left(\lambda_n^{(i)} r\right)\,, \tag{4.15}$$

where we have considered $B_m = 0$ because Y_m is singular at $r = 0$. In the coronal medium ($r \geq a$) this function is

$$R_m^{(e)}(r) = C_m H_m^{(1)}\left(\lambda_n^{(e)} r\right)\,, \tag{4.16}$$

where $D_m = 0$ because $H_m^{(2)}$ represents an incoming wave and we assume that there is no propagation of energy towards the cylinder. It is interesting to note that this condition is not assumed in case of two or more interacting cylinders (Chapter 5) where the incoming wave on a cylinder is the scattered waves of the other. With Equations (4.13), (4.14), (4.15), (4.16) and the boundary conditions (Equations 4.11 and 4.12) the dispersion relation is obtained

$$\frac{J_m'\left(\lambda_n^{(i)} a\right)}{\lambda_n^{(i)} J_m\left(\lambda_n^{(i)} a\right)} = \frac{H_m^{(1)\prime}\left(\lambda_n^{(e)} a\right)}{\lambda_n^{(e)} H_m^{(1)}\left(\lambda_n^{(e)} a\right)}\,. \tag{4.17}$$

By solving this dispersion relation we find the frequencies of the transverse normal modes of oscillation of a magnetised cylinder. In general, solutions can be of the so-called surface or body type, although in the zero-β limit only body waves are allowed (see Edwin and Roberts, 1983). Two kinds of body waves exist, the *trapped* and *leaky* normal modes, similar to the slab eigenmodes of Section 3.1. In the trapped modes the radial wave number (Equation 4.8) is imaginary,

$$\lambda_n^{(e)} = i\sqrt{k_z^2 - \frac{\omega^2}{v_{Ae}^2}}\,, \tag{4.18}$$

where ω is real. Here $\omega \leq \omega_{ce}$ and $\omega_{ce} = k_z v_{Ae}$ is the external cut-off frequency defined in Section 3.1. Trapped modes are non-damped solutions of the eigenvalue problem, their amplitude being constant in time and their energy being confined in the tube and its close environment. Leaky modes are solutions with a complex wave number of the form

$$\lambda_n^{(e)} = -i\sqrt{\frac{\omega^2}{v_{Ae}^2} - k_z^2}\,, \tag{4.19}$$

where the frequency ω is a also complex number. Leaky modes radiate away their energy and are damped solutions with a decreasing amplitude in time (see, e.g., Spruit, 1982; Edwin and Roberts, 1983; Cally, 1986, 2003, and Chapter 3).

With Equation (4.17) the trapped and leaky eigenmodes of a cylindrical flux tube are found. These normal modes are labelled by three integers n, m and p associated to their radial, azimuthal and longitudinal wave structure respectively. Solutions with $n > 1$ are leaky with a rapid damping. According to Cally (1986, 2003), the damping time is

$$\tau \approx a\,\frac{v_{Ae}}{v_{Ai}^2}. \tag{4.20}$$

where $v_{Ai} \ll v_{Ae}$ and $k_z a \ll 1$ are assumed. In coronal loop conditions, this damping time is of order of several seconds and so these modes cannot be detected with present day instruments. This is the reason why we do not consider $n > 1$ in this work. In addition, there is a leaky mode with $n = 1$ called principal fundamental leaky mode with a long damping time. However, this mode is very difficult to excite after an initial disturbance and there is no evidence of its existence in time-dependent solutions (see Terradas et al., 2007; Terradas, 2009). With respect to the longitudinal number, we consider $p = 1$ because the observations reveal that in many cases the maximum amplitudes of the oscillations are in the loop apex as we have seen in Section 1.3. The normal mode with $m = 0$ is the so-called sausage mode and in coronal loops it is leaky with a very rapid damping. With the previous considerations, hereafter, we focus on trapped modes with $n = p = 1$ and $m \geq 1$. The mode with $m = 1$ is the so-called *kink mode* and there are evidences that this mode is excited in coronal loop oscillations (see Section 1.3). Other trapped modes ($m > 1$) are the so-called fluting modes but there are no observational evidences of these oscillations. It is possible to find an approximate analytical expression for the frequency of the $m \leq 1$ trapped modes in the thin tube (TT) approximation. If $m \geq 1$ and $k_z a \to 0$, Equation (4.17) becomes after some algebra

$$\frac{\omega L}{v_{Ai}} = \sqrt{\frac{2}{1+\frac{\rho_e}{\rho_i}}}\,\pi\,, \tag{4.21}$$

where we see that all $m \geq 1$ modes share their frequencies, that depend exclusively on the density contrast, ρ_i/ρ_e. Equation (4.2) is the so-called kink frequency, usually denoted by ω_k.

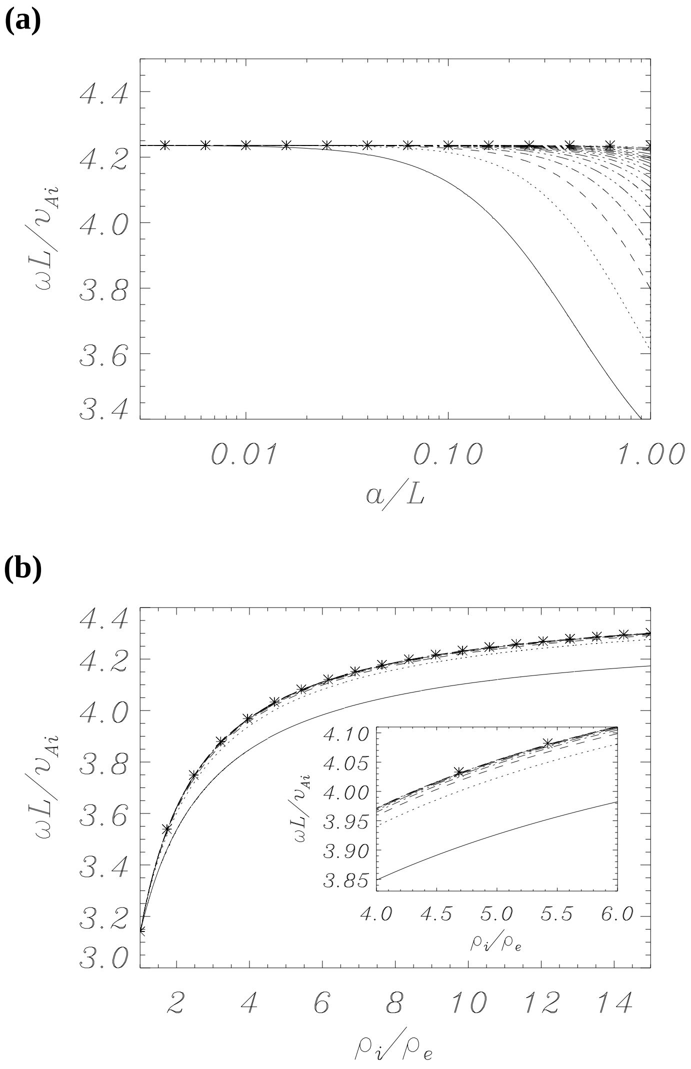

Figure 4.2: Normalised frequency of the trapped modes, $\omega L/v_{Ai}$, as a function of the loop radius **(a)** and density contrast **(b)**. The solid curves corresponds to the kink mode ($m = 1$) and the dotted and dashed lines corresponds to the fluting modes ($m > 1$). In **(a)** we have considered a system with $\rho_i = 10\rho_e$ and in **(b)** the loop radius is fixed to $a = 0.1L$. The asterisks mark the frequencies computed with Equation (4.21) of the TT approximation ($k_z a \ll 1$).

In Figure 4.2, the frequencies of the trapped normal modes (i.e. those with $m \geq 1$) computed by numerically solving Equation (4.17) are plotted as a function of the loop radius (Figure 4.2a) and density contrast (Figure 4.2b). From Figure 4.2a we clearly see that all the mode frequencies tend to the same value for $k_z a \to 0$ given by the TT frequency approximation of Equation (4.21). For typical loop radii ($a/L \leq 0.1$) the kink frequency of Equation (4.21) is a good approximation (see Section 1.3). In addition, from Figure 4.2a we see that the fluting mode frequencies tend to the kink frequency as $m \to \infty$. In

Figure 4.2b the dependence of the normal mode frequencies with the density contrast is shown. We see that they have a strong dependence for small values of this parameter, but reach a more or less constant value for sufficiently high values of the density contrast. This asymptotic value is easily computed with Equation (4.21), giving $\omega L/v_{Ai} = \sqrt{2}\pi \approx 4.44$. In the opposite limit ($\rho_i/\rho_e \to 1$), all the frequencies tend to the TT value. For $\rho_i/\rho_e = 1$ these frequencies are exactly π, indicating that the loop oscillates with the external cut-off frequency ($\omega_{ce}L/v_{Ai} = \pi$).

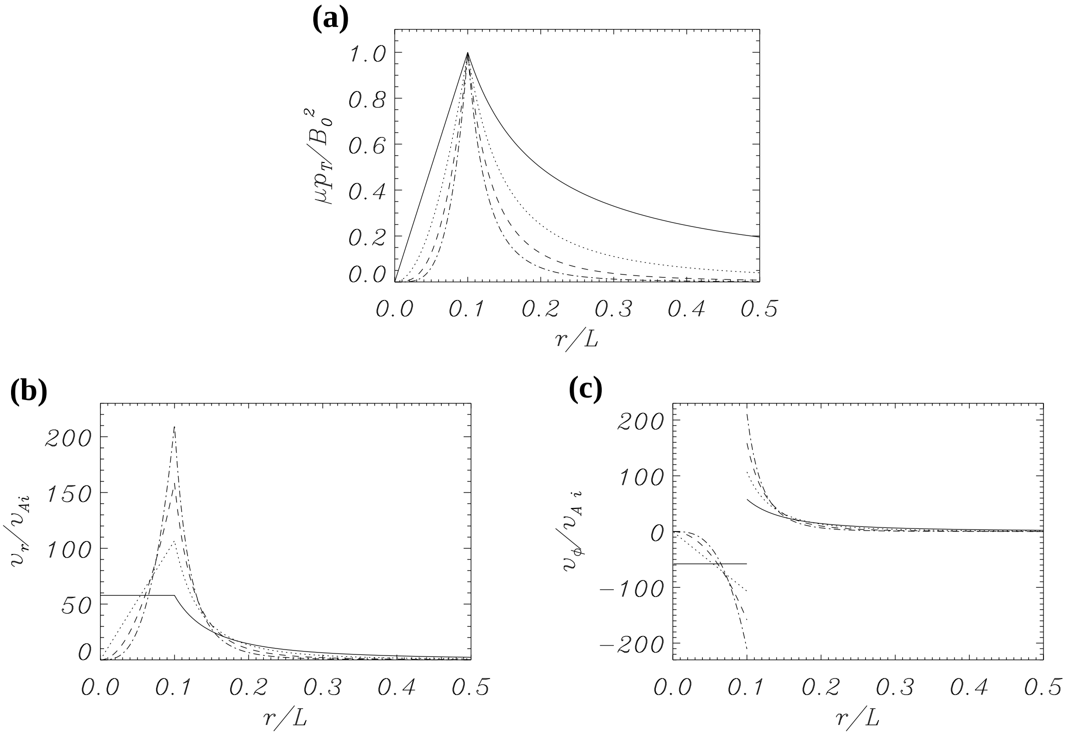

Figure 4.3: Radial dependence of the normalised eigenfunctions: **(a)** magnetic pressure perturbation, p_T, **(b)** radial velocity component, v_r, and **(c)** azimuthal velocity component, v_ϕ, for the *kink mode* (solid curves) and the $m = 2, 3, 4$ *fluting modes* (dotted and dashed lines) computed with Equations (4.2), (4.13) and (4.14) after solving the dispersion relation (Equation 4.17). The loop radius is $a/L = 0.1$ and the density contrast is $\rho_i/\rho_e = 10$.

With the frequencies of the normal modes it is possible to find their spatial structure from Equations (4.2), (4.13) and (4.14). In Figure 4.3 the eigenfunctions $p_T(r)$, $v_r(r)$ and $v_\phi(r)$ are plotted for the *kink mode* and for the *fluting modes* with $m = 2, 3, 4$. For the kink mode, the velocity components v_r and v_ϕ are uniform inside the tube. However, the fluting modes are confined near the tube surface ($r = a = 0.1L$). It is important to note from this figure that only the kink mode has a non zero velocity in the tube axis ($r = 0$). From Figures 4.3a and 4.3b, we clearly see the continuity of the magnetic pressure perturbation

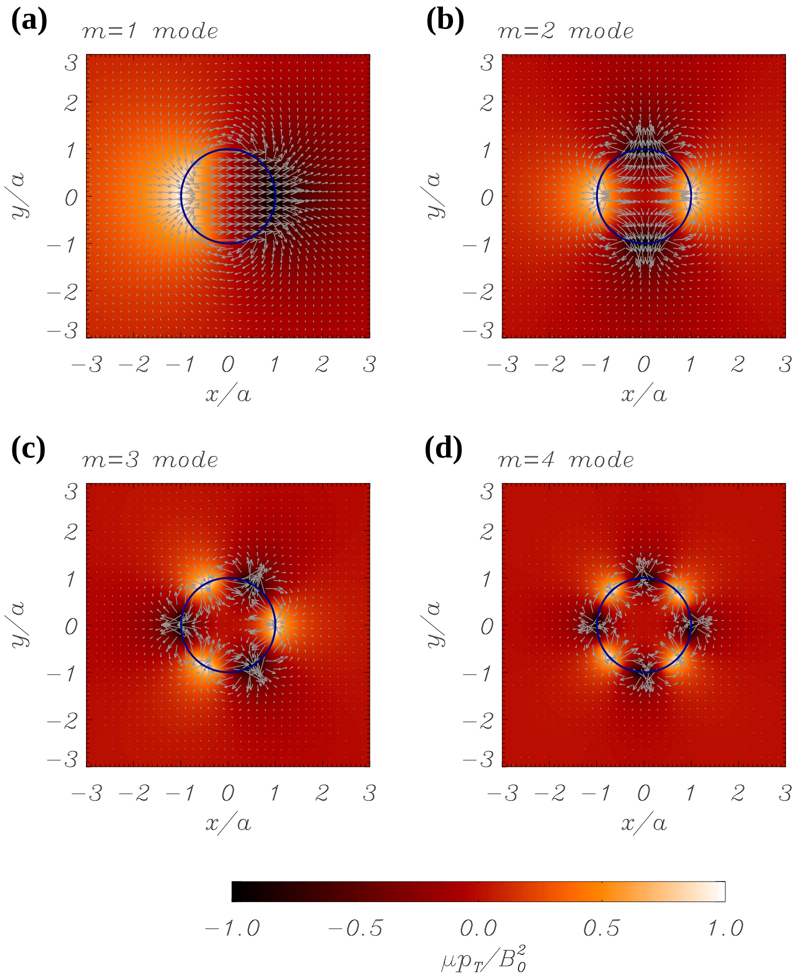

Figure 4.4: Transverse structure of the magnetic pressure perturbation (colour field) and velocity field (arrow field) for the first four fast MHD normal modes of a homogeneous tube $m = 1, 2, 3, 4$. **(a)** Kink mode with azimuthal number $m = 1$, fluting modes with **(b)** $m = 2$, **(c)** $m = 3$ and, **(d)** $m = 4$.

(p_T) and the radial component of the velocity (v_r) at the loop surface ($r = a$), such as required by the boundary conditions (Equations 2.45). However, from Figure 4.3c we see that the azimuthal component of the velocity (v_ϕ) has a jump at $r = a$ for all modes. Outside the tube, the trapped mode signature is shown and the perturbations p_T, v_r and v_ϕ decrease with the distance from the loop centre. The fluting mode eigenfunctions decrease more rapidly than those of the kink mode, indicating that the former are more confined. In Figure 4.4 the two dimensional magnetic pressure perturbation and velocity fields are plotted. The *kink mode* ($m = 1$) produces a displacement of the whole tube. The spatial structure of the *fluting modes* ($m > 1$) is more complex than the kink mode and such modes just distort the loop surface but do not produce a net displacement of the tube.

4.2 Two identical cylindrical loops

The equilibrium configuration considered here consists of a system of two parallel, homogeneous straight cylinders of radius a, length L and separation between centres d (see Figure 4.5). We assume the following equilibrium plasma density profile

$$\rho_e(x,y) = \begin{cases} \rho_e, & \text{if } r_1 > a \text{ and } r_2 > a, \\ \rho_i, & \text{if } r_1 \leq a \text{ or } r_2 \leq a, \end{cases} \tag{4.22}$$

where x, y are the Cartesian coordinates and r_1 and r_2, defined as $r_1^2 = (x+d/2)^2 + y^2$ and $r_2^2 = (x-d/2)^2 + y^2$, are the distances from the point (x, y) to the centres of the left and right loops, respectively. The loop centres lie on the x-axis at $x = d/2$ for the right loop and $x = -d/2$ for the left loop. The configuration is symmetric with respect to the yz-plane and the z-axis is parallel to the axes of the cylinders. As in Section 4.1, the loops and the environment are permeated by a uniform magnetic field along the z-direction. The line-tying effect is also incorporated by setting $k_z = \pi/L$.

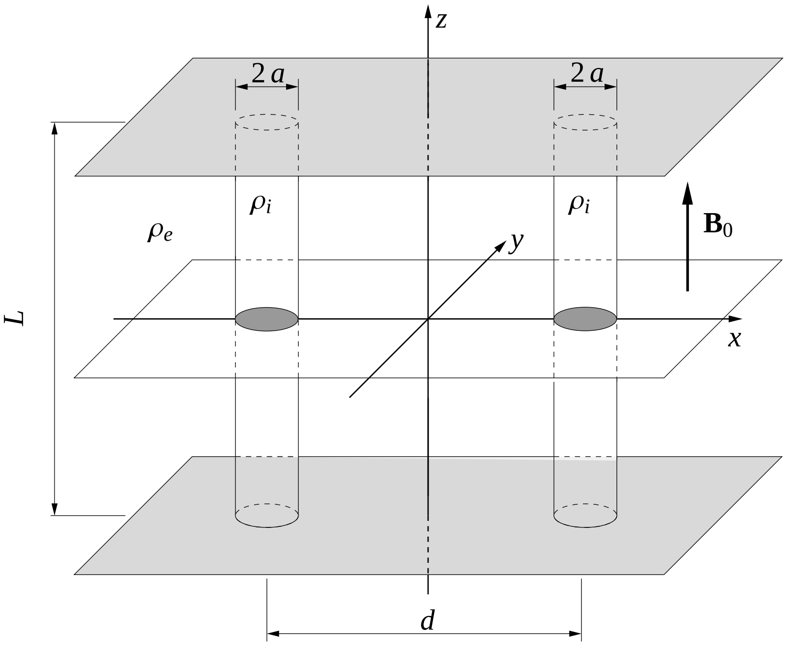

Figure 4.5: Sketch of the model, that consists of two straight cylinders immersed in the coronal medium. Hereafter the total pressure and the velocity fields are plotted in the xy-plane, shown as a white slice.

4.3 Normal modes

The methods used for a single cylinder (see Edwin and Roberts, 1983) cannot be applied to the study of two tubes. One way to solve the problem is to use scattering theory; see for example Bogdan and Zweibel (1985), Bogdan and Knoelker (1991), Bogdan and Fox (1991) and Keppens et al. (1994). Another way is to numerically solve the eigenvalue problem given by the ideal MHD equations. We have followed this approach and have calculated the normal modes with the PDE2D code (Sewell, 2005). We have concentrated in the trapped normal modes of the system. We have used bicylindrical orthogonal coordinates, defined by the transformation

$$x = \frac{b \sinh v}{\cosh v - \cos u}\ , \ y = \frac{b \sin u}{\cosh v - \cos u}\ , \ z \ = \ z, \tag{4.23}$$

where $0 \leq u < 2\pi$, $-\infty < v < \infty$, $-\infty < z < \infty$ and $b = \sqrt{\left(\frac{d}{2}\right)^2 - a^2}$. The u = const and v = const coordinate lines are shown in Figure 4.6. The loop boundaries are the coordinate lines $v = \pm \mathrm{arcsinh}\, \frac{\sqrt{d^2-4a^2}}{2a}$, where the positive and negative signs correspond to the right and left tubes, respectively. We impose a temporal dependence of the form $e^{-i\omega t}$ and a spatial dependence along the tube $e^{ik_z z}$ in Equations (2.20) and (2.21) for the velocity and magnetic perturbations. With the previous assumptions these equations can be written in bicylindrical components as

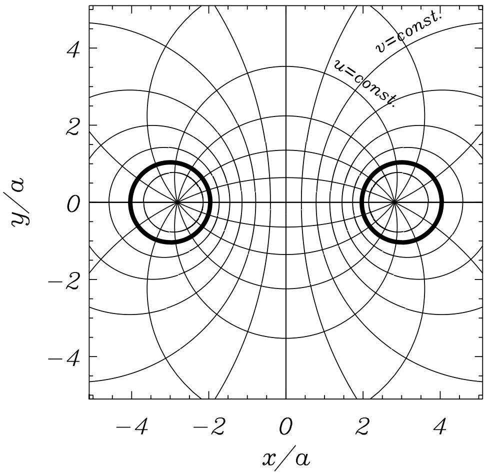

Figure 4.6: Bicylindrical coordinates (u, v, z). The coordinate lines u = const and v = const are plotted in an arbitrary plane z = const. The thick circles show the tube boundaries and coincide with two coordinate lines v = const. The separation between the tubes is $d = 6\ a$.

$$\omega\, v_u = -v_A^2\, k_z B_u + i\, v_A^2 \frac{(\cos u - \cosh v)}{b} \frac{\partial B_z}{\partial u}\ , \tag{4.24}$$

$$\omega\, v_v = -v_A^2\, k_z B_v + i\, v_A^2 \frac{(\cos u - \cosh v)}{b} \frac{\partial B_z}{\partial v}\ , \tag{4.25}$$

$$\omega\, B_u = -k_z B_0 v_u\ , \tag{4.26}$$

$$\omega\, B_v = -k_z B_0 v_v\,, \tag{4.27}$$

$$\omega\, B_z = +i\,\frac{B_0}{b}\left[\sin u\; v_u + \sinh v\; v_v + (\cos u - \cosh v)\left(\frac{\partial v_u}{\partial u} + \frac{\partial v_v}{v}\right)\right]. \tag{4.28}$$

These set of equations constitute the eigenvalue problem that we solve numerically with the PDE2D code to find the normal modes of the two-cylinder configuration.

We find four collective fundamental trapped modes (see Figure 4.7) where the velocity field is more or less uniform in the interior of the loops and so they move basically as a solid body, while the external velocity field has a more complex structure. The structure of the velocity field inside the tube is similar to the kink eigenmode velocity inside of a isolated tube. We call these as kink-like modes. The four velocity field solutions have a well defined symmetry with respect to the y-axis. In Figure 4.7a, we see that the velocity field inside the tubes lies in the x-direction and is symmetric with respect to the y-axis. We call this mode S_x, where S refers to the symmetry of the velocity field with respect to the y-axis and the subscript x refers to the direction of the velocity inside the tube. The same nomenclature is used for the other modes. In Figure 4.7b the velocity inside the cylinders is mainly in the x-direction and is antisymmetric with respect to the y-axis, so we call this mode A_x. Similarly, in Figure 4.7c the velocity lies in the y-direction and is symmetric with respect to the y-axis, while it is antisymmetric in Figure 4.7d. Hence, we call these modes S_y and A_y, respectively. The pressure field of the A_x and S_y modes is symmetric with respect to the y-axis, while that of the S_x and A_y modes is antisymmetric.

The frequencies of oscillation of these four modes as a function of the loop separation, d, are displayed in Figure 4.8. For large separations between the tubes, the mode frequencies tend to the kink mode of an individual loop (see dotted line). On the other hand, for smaller separations, they split in four branches associated to the four oscillatory modes described before. The splitting effect was noticed in Díaz et al. (2005) and Luna et al. (2006) (see Chapter 3) in a configuration of several slabs. The frequency difference between the modes increases when the interaction between the loops becomes stronger, i.e. when the distance between them smaller. When the loops are very close ($d \sim 2a$), the frequencies of the S_x and A_y modes tend to the value $\omega = 3.33/\tau_{Ai}$, which is similar to the internal cut-off frequency, $\omega_{ci} = k_z v_{Ai} = \pi/\tau_{Ai}$ (the difference is only around 6%). Here τ_{Ai} is the Alfvén transit time, defined as $\tau_{Ai} = L/v_{Ai}$. On the other hand, in this limit, the S_y and A_x frequencies are quite large in comparison to the kink mode frequency.

It is interesting to note that when both tubes move symmetrically in the x-direction, i.e. in the S_x mode, the fluid between them follows the loops motion (see Figure 4.7a). On the other hand, when the loops oscillate antisymmetrically, i.e. in the A_x mode, the intermediate fluid is compressed and rarefied (see Figure 4.7b), producing a more forced motion than that of the symmetric mode. This is the reason for the S_x (A_x) mode having a smaller (larger) frequency than that of the individual loop. For the modes polarised in the y-direction the behaviour is somehow similar, although in this case the antisymmetric mode (see Figure 4.7d) has a lower frequency than the symmetric mode (see Figure 4.7c).

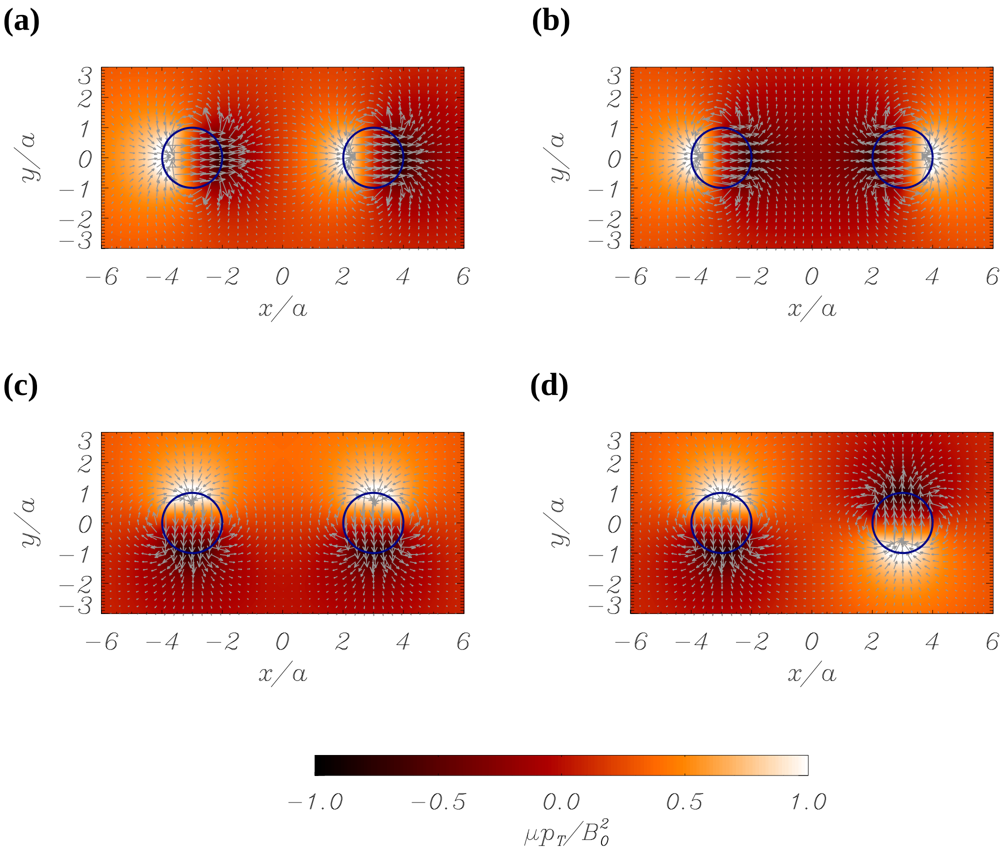

Figure 4.7: Total pressure perturbation (colour field) and velocity field (arrows) of the fast four collective normal modes (plotted in the *xy*-plane, see Figure 4.5). The modes are labelled as **(a)** S_x, with the loops moving in phase in the *x*-direction; **(b)** A_x, the tubes move in the *x*-direction but in antiphase; **(c)** S_y, the tubes move in the *y*-direction in phase; and finally **(d)** A_y, the loops move in antiphase in the *y*-direction. Here, the loop radii are $a = 0.1L$ and the distance between centres is $d = 6a$.

In the A_y mode, one of the loops moves upwards the surrounding fluid near the other loop moves downwards. This helps to push the second loop in this direction and produces the antisymmetric motion. The situation is the opposite for the S_y mode, for which the direction of motion of the surrounding fluid is opposite to that of the other tube. This explains why the frequency of the A_y solution is smaller than that of the S_y mode.

4.4 Time-dependent analysis: numerical simulations

In Section 4.3 we have studied the normal modes of the two identical loop system. Nevertheless coronal loop oscillations are often flare-initiated events and the normal modes

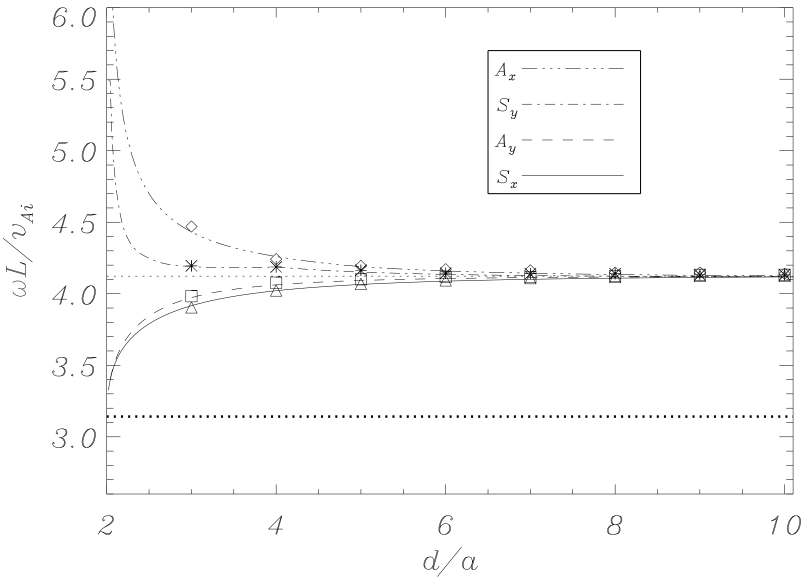

Figure 4.8: Frequency, ω, as a function of the separation between cylinders, d, for a density enhancement $\rho_i/\rho_e = 10$ and loop radius $a = 0.1L$. The lower horizontal thick dotted line is the internal cut-off frequency, $\omega_{ci} = \pi/\tau_{Ai}$. The thin dotted line is the kink frequency ($\omega = 4.12/\tau_{Ai}$) of an individual loop. The calculated frequencies from the time-dependent results in Section 4.4.1 are also plotted as triangles (S_x), squares (A_y), asterisks (S_y) and diamonds (A_x).

of the system are probably not a complete picture of such events. It is more appropriate to describe the evolution of the system after a perturbation by solving the initial value problem.

To solve the initial value problem of Equations (2.20) and (2.21) and an initial perturbation in our system, we use the CLAWPACK (Leveque, 2002) code based on finite volume methods. Since we consider a finite domain, we have evaluated the effect of reflections at the domain boundaries on the system dynamics. In our simulations flow-through boundary conditions are imposed (see Leveque, 2002). The system dynamics for sufficiently large domain sizes are studied and it is concluded that the reflections do not produce appreciable effects. The domain size is $3L \times 3L$ and the number of grid-points is 2100×2100.

The governing Equations (2.20) and (2.21) in Cartesian coordinates are

$$\frac{\partial v_x}{\partial t} = \frac{v_A^2}{B_0}\left(k_z\,\widetilde{B}_x - \frac{\partial B_z}{\partial x}\right), \tag{4.29}$$

$$\frac{\partial v_y}{\partial t} = \frac{v_A^2}{B_0}\left(k_z\,\widetilde{B}_y - \frac{\partial B_z}{\partial y}\right), \tag{4.30}$$

$$\frac{\partial \widetilde{B}_x}{\partial t} = -\, B_0\, k_z\, v_x\,, \tag{4.31}$$

$$\frac{\partial \widetilde{B}_y}{\partial t} = -\, B_0\, k_z\, v_y\,, \tag{4.32}$$

$$\frac{\partial B_z}{\partial t} = -B_0\left(\frac{\partial v_x}{\partial x} + \frac{\partial v_y}{\partial y}\right)\,, \tag{4.33}$$

where the line-tying effect is incorporated by setting the longitudinal wave number k_z. Here $B_x = -i\widetilde{B}_x$ and $B_y = -i\widetilde{B}_y$ are purely imaginary variables. This fact indicates that the x- and y-components of the magnetic field have a phase lag of $\pm\pi/2$ with respect to the temporal evolution of the other variables. The initial perturbation is a planar pulse in the velocity field of the form

$$\mathbf{v}_0 = \mathbf{K}\, e^{[-\mathbf{K}\cdot(\mathbf{r}-\mathbf{r}_0)/\Delta]^2}, \tag{4.34}$$

i.e. a Gaussian profile (of width $\Delta = 0.2L$ centred at $\mathbf{r}_0 = (d/2, 0, 0)$) and direction of propagation along $\mathbf{K} = -(\cos\alpha, \sin\alpha, 0)$, α being the angle between the wave vector and the x-axis. Here $\mathbf{K}$ also defines the initial polarisation of $\mathbf{v}$, which is perpendicular to the planar pulse. The initial value of the magnetic field perturbation is zero and thus the same applies to the total pressure perturbation.

In Figures 4.9, 4.10 and 4.11 three examples of the time evolution are shown for $\alpha = 90^\circ, 0^\circ$ and 45°, respectively, and for a fixed distance between loops, $d = 6a$, identical to the one used in Figure 4.7. These three cases illustrate the time evolution of the system after a perturbation, which consists of two regimes: the transient and the stationary phases. The stationary phase is characterised by oscillations in one or several fundamental trapped normal modes (see Section 4.3). On the other hand, in the transient phase there are leaky modes and internal reflections and refractions.

In Figure 4.9 (see Movie 1 in the accompanying CD) the time evolution for the $\alpha = 90^\circ$ initial disturbance is shown, for which the pulse front lies along the x-axis and excites the v_y component. The loops are perturbed at the same time (as can be appreciated in Figure 4.9b) and as a consequence they oscillate in phase. In Figure 4.9b the system is in the transient phase, characterised by internal reflections related with the emission of leaky modes. The external medium has not relaxed yet. Finally, the system reaches the stationary phase (see Figures 4.9c and 4.9d) and oscillates with the S_y trapped mode (compare the velocity field and the pressure distribution with those of Figure 4.7c).

In Figure 4.10 (and Movie 2 in the accompanying CD), the time evolution for the $\alpha = 0^\circ$ initial disturbance is shown. Now the pulse is centred on the right loop (see Figure 4.10a) and excites the v_x component. In Figure 4.10b, the pulse reaches the left tube and passes through it, the system still being in the transient phase. On the other hand, in Figures 4.10c and 4.10d the system oscillates in the stationary phase. It is interesting to note that this particular initial disturbance does not excite the left loop; neither at $t = 0$ nor during the transient phase. Nevertheless, the oscillatory amplitude in the left loop grows with time in the stationary phase, while the amplitude in the right loop decreases in the time interval shown in Figures 4.10c and 4.10d (see also Movie 2). Then, it is clear

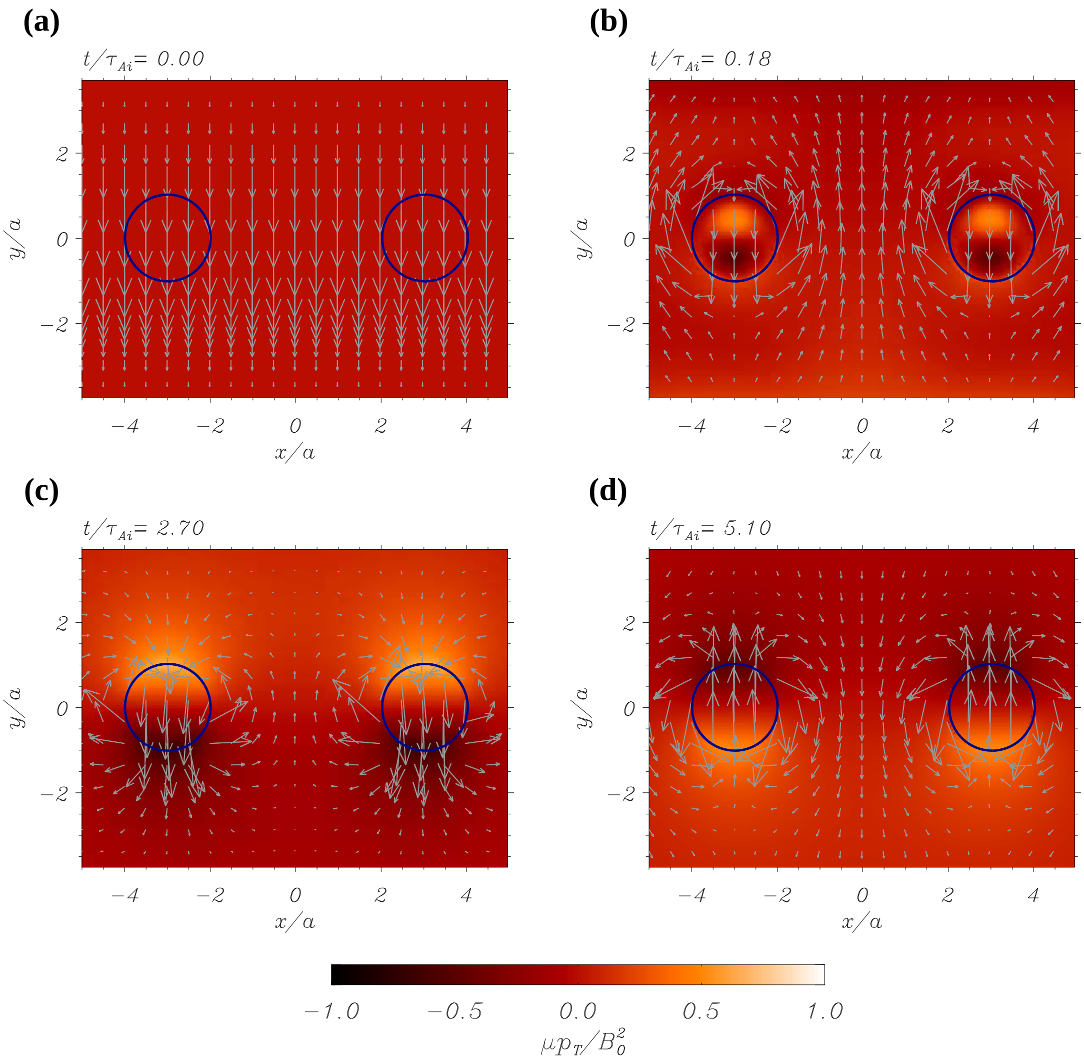

Figure 4.9: Time-evolution of the velocity field (arrows) and total pressure field (coloured contours) for a separation between loops $d = 6a$ and an initial pulse with an angle $\alpha = 90°$. The two circles mark the positions of the loops at $t = 0$. The panels show different evolution times. In **(a)** the initial condition over the velocity field is represented. In **(b)** the velocity and pressure field shortly after the initial disturbance, that is, during the transient phase, are shown. Both tubes are excited at the same time. In panels **(c)** and **(d)** the system oscillates in the stationary phase with the S_y normal mode. This time evolution is also available as an mpeg animation in Movie 1 in the accompanying CD.

that the left tube acquires its movement through the interaction with the right loop, i.e. by a transfer of energy from the right loop to the left loop. This process is reversed and repeated periodically: once the left loop has gained most of the energy retained by the loops system, so that the right loop is almost at rest, the left tube starts giving away its

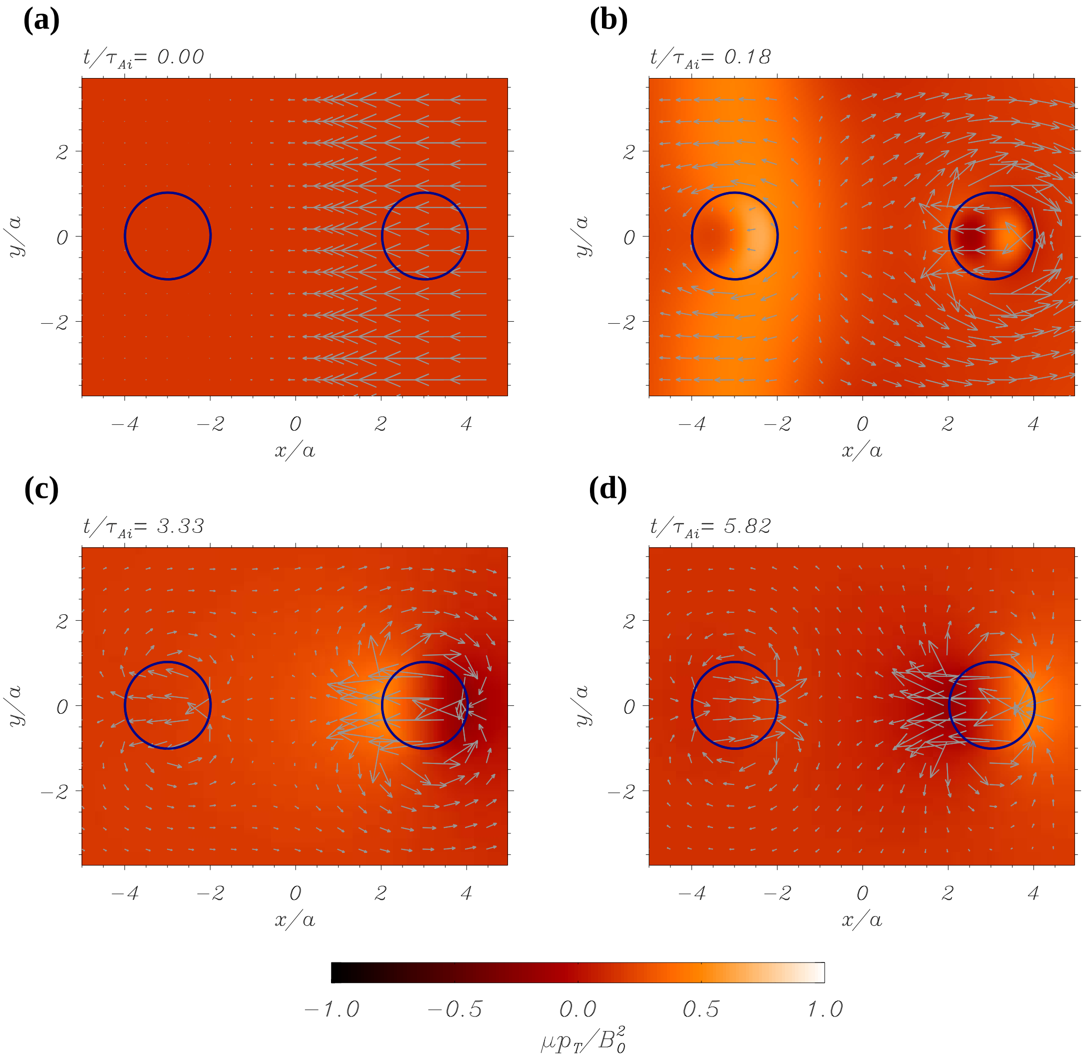

Figure 4.10: Same as Figure 4.9 for an initial pulse with an angle $\alpha = 0°$. Here the stationary phase is governed by a superposition of the S_x and A_x normal modes. The whole time evolution is presented in Movie 2 in the accompanying CD.

energy to the right cylinder and so on. This is simply a beating phenomenon, that can be explained in terms of the normal modes excited in this numerical simulation. In fact, the initial disturbance excites the S_x and A_x modes with the same amplitude and for this reason the excitation is initially maximum on the right tube and zero on the left tube. A more detailed discussion about this issue is given in Section 4.5.

Finally, we discuss the results for an excitation with $\alpha = 45°$. This simulation is the most complex and general of all (see Movie 3 in the accompanying CD). As we can see in Figure 4.11a now both components of the velocity are excited. In Figure 4.11b the initial pulse reaches the left tube and passes through it, but only leaky modes are

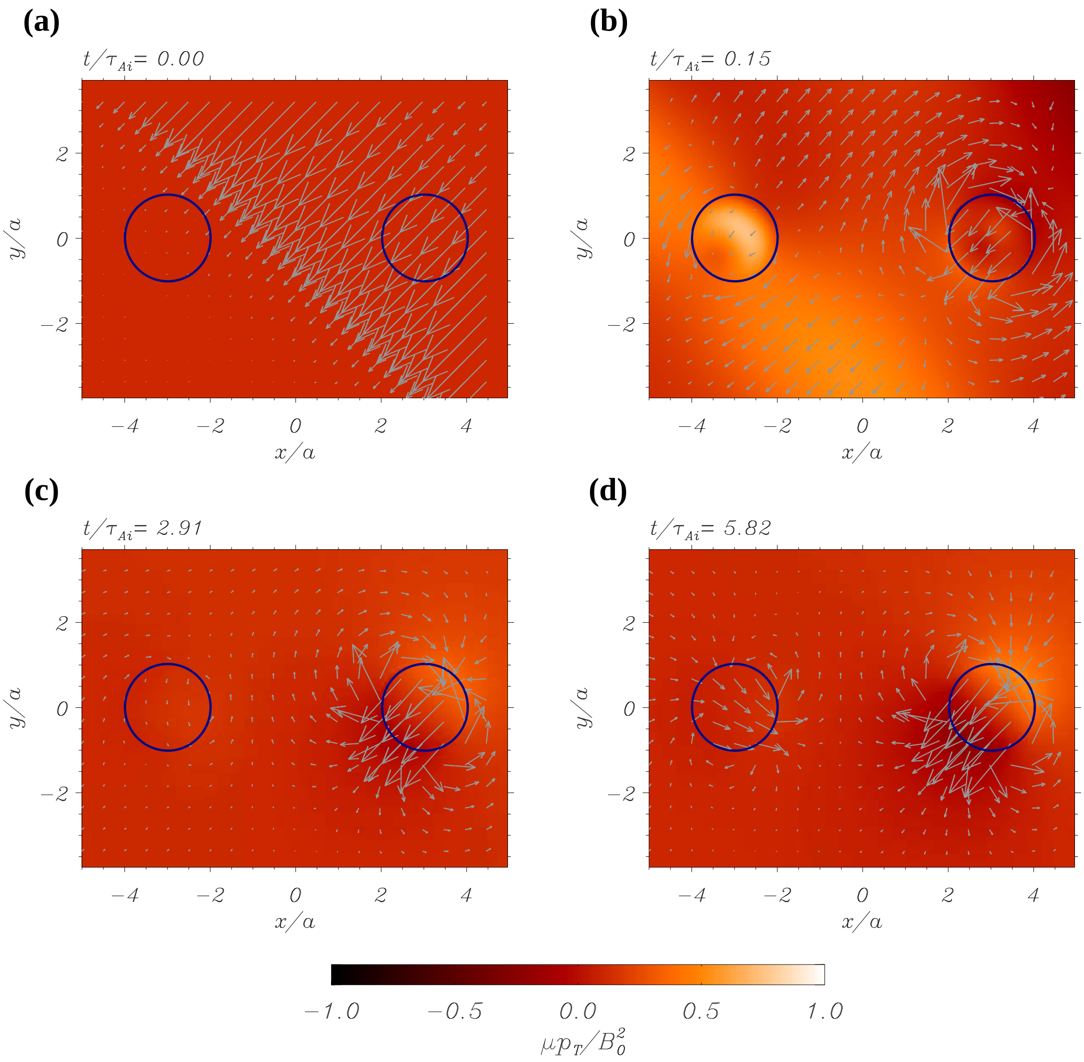

Figure 4.11: Same as Figure 4.9 for an initial pulse with an angle $\alpha = 45°$. Here the stationary phase is governed by a superposition of the S_x, A_x, S_y and A_y normal modes. The whole time evolution is presented in Movie 3 in the accompanying CD. Movie 4 contains the time evolution for much larger times.

excited. In Figures 4.11c and 4.11d the system oscillates in the stationary phase, which is a combination of the four modes S_x, A_x, S_y and A_y. As in the previous case, there is beating but now it is present in both the x- and y-velocity components. Like in the previous simulation, the left loop is almost at rest until the stationary phase (see also dotted curves in Figures 4.12a and 4.12c) despite that in this simulation the pulse directly hits the left loop without the obstacle of the right loop. In Section 4.5 details about the behaviour of the system are given.

Once we know the general features of the excitation of the two cylinders we can perform a parametric study of the effect of the distance between the loops and also the angle of excitation on the loops motion.

4.4.1 Effect of the distance between loops

We generate an initial disturbance with an angle of 45° for different loop separations, d, and measure the velocity in the loops as a function of time. From this information we can extract the frequencies of oscillation. As we have seen, since the velocity field inside the loops is more or less uniform (see Figure 4.7), it is enough to measure the velocity at the centre of the loops to describe their global motion. The reason for choosing the initial disturbance with $\alpha = 45^\circ$ is that it excites the four normal modes, so that with a single simulation we can measure their frequencies.

In Figures 4.12a and 4.12c the x- and y-components of the velocity at the centre of each loop are plotted. In these figures we see that, after a very brief transient characterised by short-period oscillations, the system oscillates with the sum of normal modes. The frequencies of the modes are quite similar and it is difficult to resolve them. Although the frequencies of these modes are present in the time-dependent signal, this information cannot be easily extracted from the data because in these simulations the maximum evolution time (which is determined by the numerical damping) is $T = 6\tau_{Ai}$. With this maximum time we have a frequency resolution $2/T \simeq 0.3/\tau_{Ai}$, but, as evidenced by Figure 4.8, the difference in frequency between the eigenmodes is typically less than $0.1/\tau_{Ai}$ so we have not enough frequency resolution. For this reason we extract the frequencies with another method, taking into account that the velocity field is the addition of normal modes with symmetric and antisymmetric spatial functions with respect to the y-axis. We measure the velocity in the loop centres $(x = -d/2, y = 0)$ and $(x = d/2, y = 0)$, i.e. two symmetric points with respect to $x = 0$. Then, the sum of both measured velocities in these points is twice the part of velocity components that are symmetric with respect to $x = 0$. Dividing this velocity by two we obtain the v_x component of the S_x mode and the v_y component of the S_y mode in these points. On the other hand, the subtraction of the measured velocities is twice the antisymmetric velocity components. Similarly, dividing this velocity by two we obtain the v_x component of the A_x mode and the v_y component of the A_y mode. The obtained mode velocities are plotted in Figures 4.12b and 4.12d. Next, we compute the periodogram of these four signals (plotted in Figures 4.13a and 4.13b), from which the frequencies of the collective modes are determined. The periodogram is preferred over the FFT as it allows to more precisely identify these frequencies. The above procedure has been applied to numerical simulations for different separations between loops and the frequencies of the four fundamental eigenmodes have been obtained. The calculated frequencies have been superimposed to the normal mode values in Figure 4.8 using symbols. A good agreement between the normal mode calculations and the time-dependent results can be appreciated.

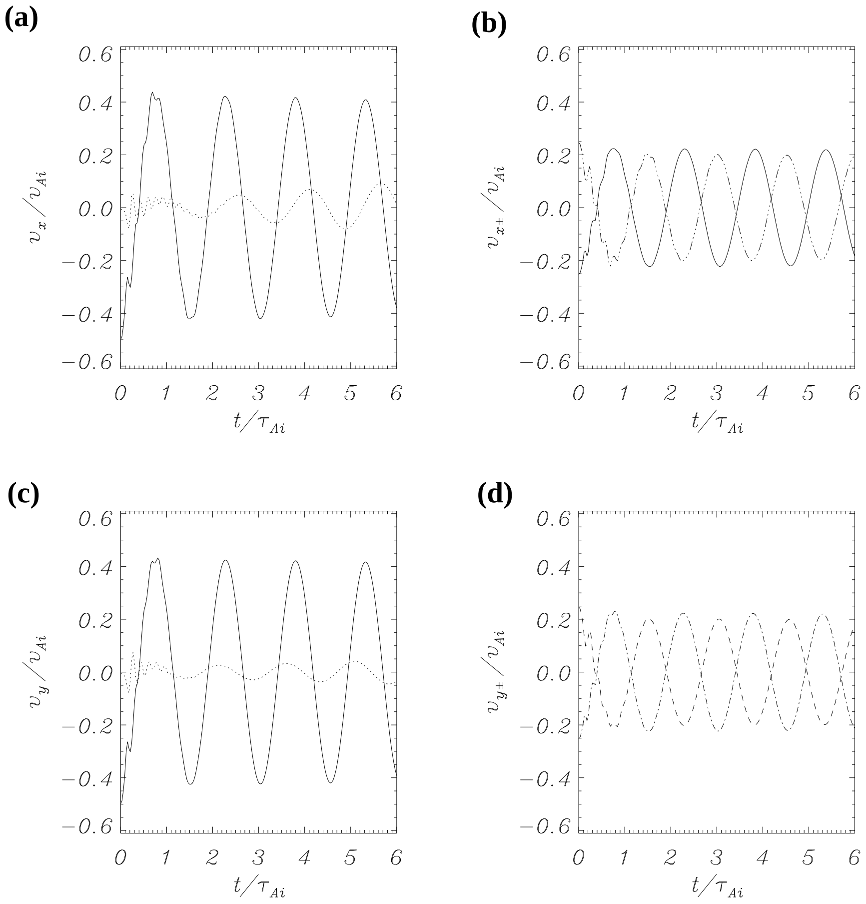

Figure 4.12: **(a)** x-component and **(c)** y-component of the velocity at the centre of the right (solid line) and left (dotted line) loops for the numerical simulation of Figure 4.11 (i.e. with an initial incidence angle $\alpha = 45°$). With the method explained in Section 4.4.1 the normal mode velocities are extracted and plotted in **(b)** for the S_x (solid line) and the A_x (three-dot-dashed line) modes and in **(d)** for the S_y (dashed line) and A_y (dot-dashed line) modes.

4.4.2 Effect of the incidence angle

We next study the evolution of the system for different incidence angles, α, of the planar pulse and a fixed distance between loops ($d = 6a$). Some examples of the time evolution have already been discussed and shown in Figures 4.9, 4.10 and 4.11. The amplitude of the excited normal modes depends on the width, Δ, the incidence angle, α and the position, $\mathbf{r}_0$, of the initial disturbance, but here we only consider the dependence on the incidence angle. The angles considered in our simulations vary from $\alpha = 0°$ to $90°$ with steps of $5°$. Using the method of Section 4.4.1 it is also possible to extract the amplitude of each normal mode, given by the amplitude of the sinusoidal oscillations in the stationary

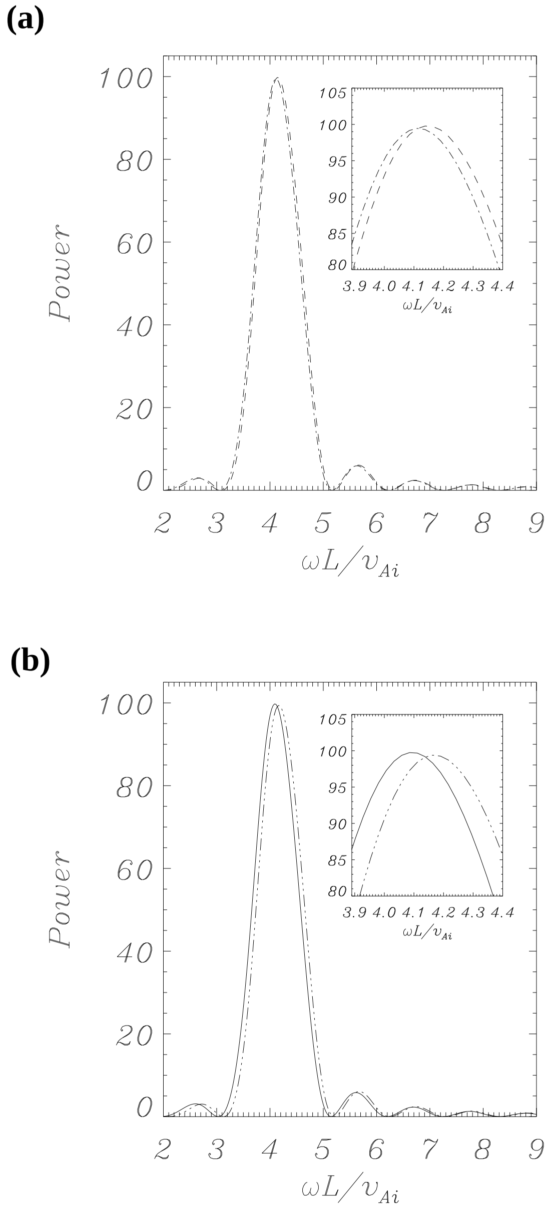

Figure 4.13: **(a)** and **(b)** corresponding power spectra of Figures 4.12b and 4.12d, respectively, plotted with the same line styles. The position of power maxima allow us to determine the frequency of the normal modes from the numerical simulation.

phase. Two examples of the extraction method are plotted in Figures 4.12 and 4.13, for $\alpha = 45°$ and Figures 4.14 and 4.15, for $\alpha = 70°$.

In Figure 4.16 the amplitude of the four collective modes is plotted as a function of the incidence angle. The behaviour of the amplitude can be divided in two parts, namely

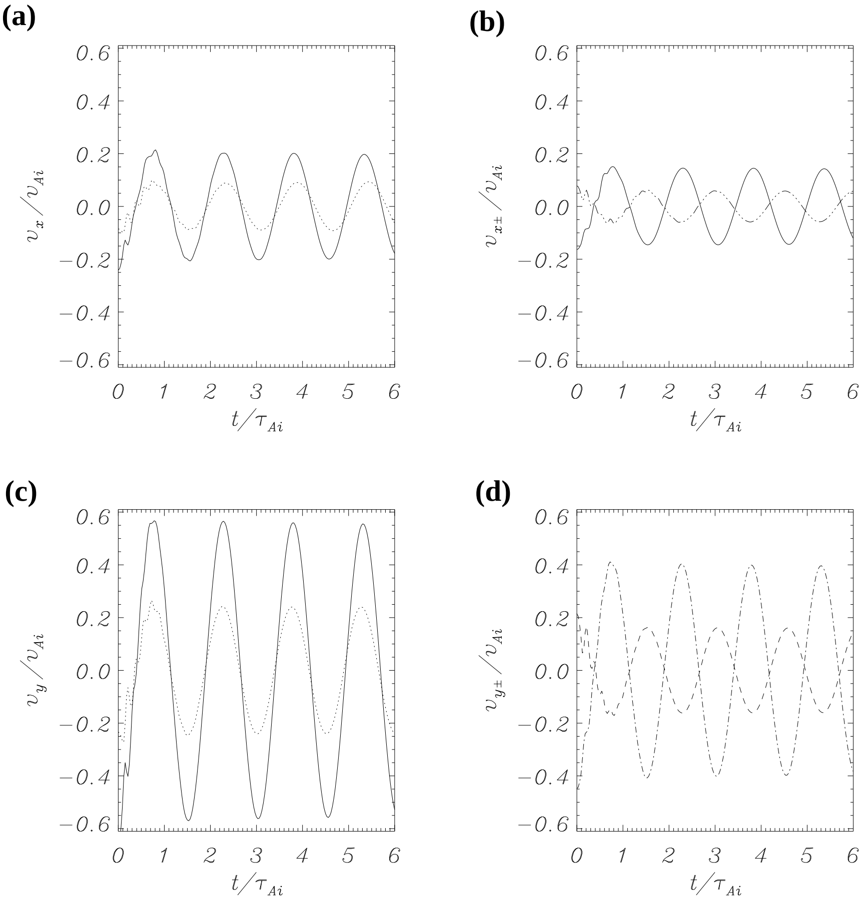

Figure 4.14: Same as Figure 4.12 for an initial incidence angle $\alpha = 70°$.

for $0° \leq \alpha \leq 50°$ and for $50° < \alpha \leq 90°$. In the first interval the amplitudes of the S_x and A_x modes are more or less equal (see Figure 4.12b and 4.12d as an example) and can be approximated by $0.3 \cos\alpha$. The same occurs for the amplitudes of the S_y and A_y modes, which vary roughly as $0.29 \sin\alpha$. In the second interval these amplitudes can be quite different (see Figures 4.14b and 4.14d as an example) and the S_x, A_x and A_y amplitudes go to zero at $\alpha = 90°$. On the other hand, the S_y amplitude increases and reaches its maximum value at $\alpha = 90°$. Furthermore, for $\alpha = 0°$ the amplitudes of the S_x and A_x modes have a maximum around 0.3 while the amplitudes of S_y and A_y modes are zero. This is because for $\alpha = 0°$ the initial disturbance drives the x-component of the velocity and so only the S_x and A_x modes are excited. Similarly, for the perturbation with $\alpha = 90°$ only the S_y and A_y modes can be excited, although the shape of our initial perturbation prevents the A_y mode from being driven and so the S_y mode reaches the largest amplitude of all modes. On the other hand, the excitation of the antisymmetric modes requires the initial disturbance to hit the right and left loops at different times. For this reason, the amplitudes of these modes decrease with α. In fact, when $\alpha = 90°$ this time difference

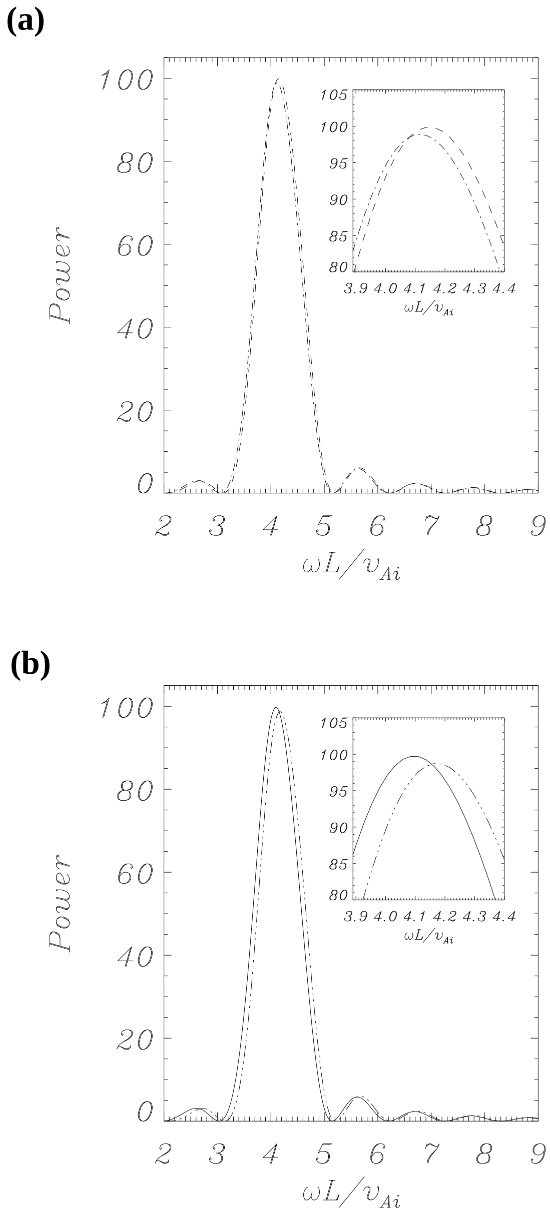

Figure 4.15: Same as Figure 4.13 for **(a)** and **(b)** the corresponding power spectra of Figures 4.14b and 4.14d, respectively, plotted with the same line styles.

is zero since both loops are excited at the same time and the amplitude of the A_x and A_y modes vanishes. Finally, it is interesting to note that for $\alpha = 45°$ the four modes are excited with almost the same amplitude.

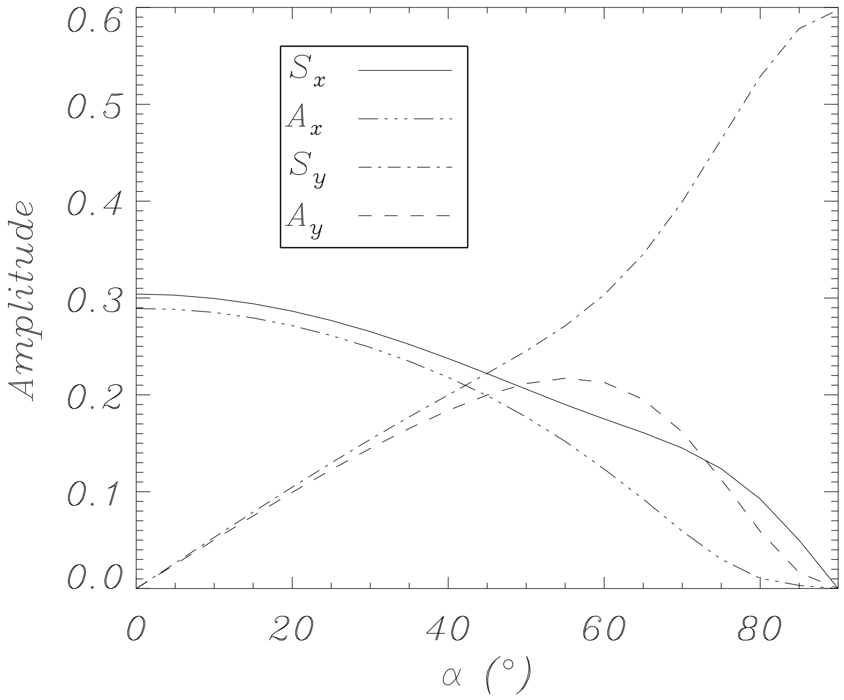

Figure 4.16: Amplitudes of the four normal modes as a function of the incidence angle α. The separation between loops is $d = 6a$.

4.5 Study of the loop motions: beating

As we have shown in the previous Section, loop motions can be very complex. This is even more clear in Movie 4, in which the time-evolution for a simulation with identical parameters to those used in Figure 4.11 but for much larger times is represented. In Section 4.4 we mentioned that the initial disturbance excites the right loop but does not perturb the left loop. After a short time the left tube starts to oscillate due to the interaction with the right one. At this stage, the right loop oscillates with the velocity polarisation of the initial pulse, whereas the left tube oscillates in a direction perpendicular to that of the initial disturbance. The reason for the complexity of the loop motions is that their oscillations are a superposition of four normal modes with different velocity polarisations, parities and frequencies.

We next analyse this case in detail. The x- and y-components of the velocity at the centre of the loops are represented in Figures 4.17a and 4.17b, respectively. There is a clear beating, characterised by the periodic interchange of the x- and y-components of the velocity between the loops. The two velocity components are modulated in such a way that v_x reaches its maximum value in the left tube and becomes zero in the right tube at the same time (around $t \simeq 40\tau_{Ai}$). This process is reversed at $t \simeq 80\tau_{Ai}$ and is repeated

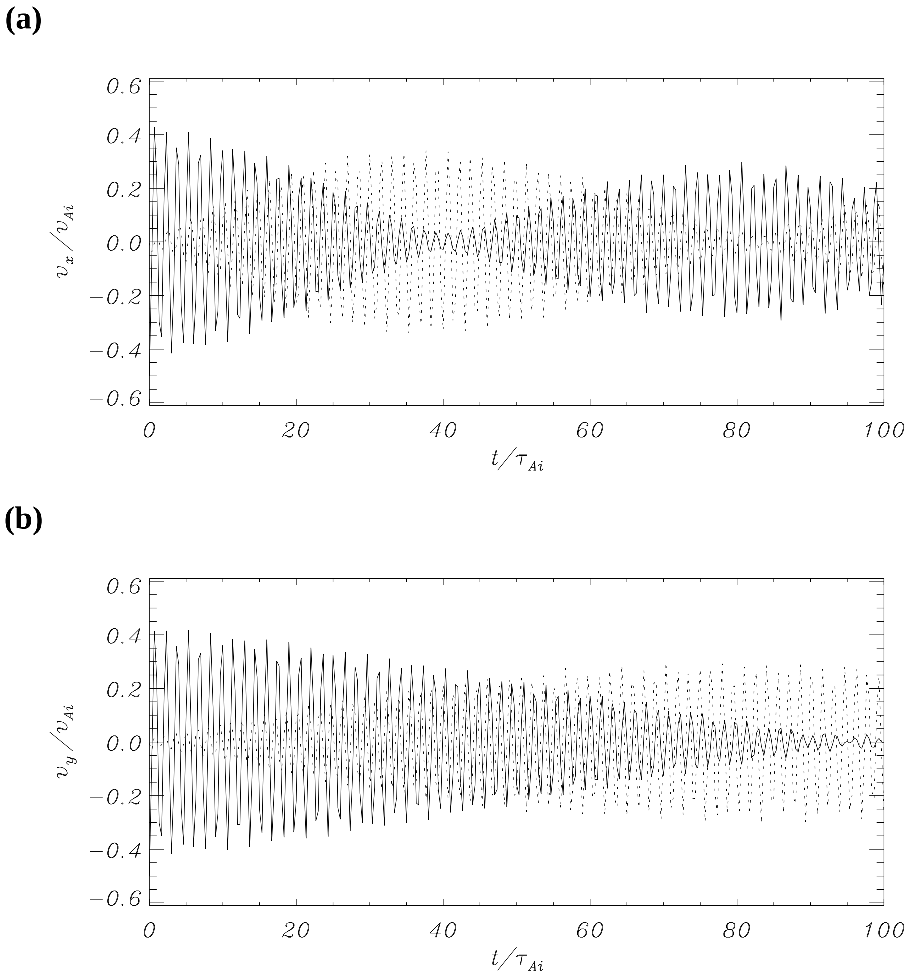

Figure 4.17: Temporal variation of the velocity components **(a)** v_x and **(b)** v_y at the centre of the right loop (solid line) and left loop (dashed line). These results correspond to the simulation shown in Figure 4.11 and illustrate the beating of the pair of loops. Damping caused by numerical dissipation causes a slight decrease of the amplitude during the numerical simulation. The time-evolution is also available as an mpeg animation in Movie 4 in the accompanying CD.

periodically.

The loop motions can be studied theoretically and the following analysis is a two dimensional generalisation of Section 3.5 (see Luna et al., 2006). In the stationary phase, during which the system oscillates in the normal modes S_x, A_x, S_y and A_y, the velocity field components inside the loops are

$$v_x(x,y,t) = C_x^S(x,y)\cos\left(\omega_x^S t + \phi_x^S\right) + C_x^A(x,y)\cos\left(\omega_x^A t + \phi_x^A\right), \qquad (4.35)$$

$$v_y(x,y,t) = C_y^S(x,y)\cos\left(\omega_y^S t + \phi_y^S\right) + C_y^A(x,y)\cos\left(\omega_y^A t + \phi_y^A\right). \qquad (4.36)$$

The S and A superscripts refer to the symmetric and antisymmetric modes, respectively. The functions C_x^S, C_x^A, C_y^S and C_y^A represent the spatial distribution of the four normal modes (see Figure 4.7) and their amplitude accounts for the energy deposited by the initial disturbance in each of them. The normal mode frequencies are represented by their frequencies, ω, while ϕ are their initial phases.

Let us turn our attention to the results in Figure 4.12. In the loos centres the symmetric and antisymmetric modes have a very similar amplitude (see also Figure 4.17 for $\alpha = 45°$), which means that $C_x^S(d/2,0) = C_x^A(d/2,0)$. Then, taking into account the parity of C_x^S and C_x^A about $x = 0$, we have $C_x^S(-d/2,0) = -C_x^A(-d/2,0)$. Inserting these expressions into Equations (4.35) and (4.36) evaluated at the loop centres we obtain

$$\begin{aligned}
\mathbf{v}_{right}(t) &= \left[C_x \cos\left(\frac{\omega_x^A - \omega_x^S}{2}\,t\right)\cos\left(\frac{\omega_x^A + \omega_x^S}{2}\,t\right),\right. && (4.37)\\
&\qquad \left. C_y \cos\left(\frac{\omega_y^A - \omega_y^S}{2}\,t\right)\cos\left(\frac{\omega_y^A + \omega_y^S}{2}\,t\right)\right],\\
\mathbf{v}_{left}(t) &= -\left[C_x \sin\left(\frac{\omega_x^A - \omega_x^S}{2}\,t\right)\sin\left(\frac{\omega_x^A + \omega_x^S}{2}\,t\right),\right. && (4.38)\\
&\qquad \left. C_y \sin\left(\frac{\omega_y^A - \omega_y^S}{2}\,t\right)\sin\left(\frac{\omega_y^A + \omega_y^S}{2}\,t\right)\right].
\end{aligned}$$

where $\mathbf{v}_{right}$ and $\mathbf{v}_{left}$ are the velocity at the centre of the right and left loop, respectively. We have defined $C_x = 2C_x^S(d/2,0)$ and $C_y = 2C_y^S(d/2,0)$ and have assumed $\phi_x^S = \phi_x^A = \phi_y^S = \phi_y^A = 0$ because the initial disturbance is over the right loop. The beating curves shown in Figure 4.17 are accurately described by these equations.

These formulae contain products of two harmonic functions. Then, the temporal evolution during the stationary phase is governed by four periods: the two oscillatory periods,

$$T_x = \frac{4\pi}{\omega_x^A + \omega_x^S}, \tag{4.39}$$

$$T_y = \frac{4\pi}{\omega_y^A + \omega_y^S}, \tag{4.40}$$

giving the mean periods of the time signal and two beating periods,

$$T_{bx} = \frac{4\pi}{\omega_x^A - \omega_x^S}, \tag{4.41}$$

$$T_{by} = \frac{4\pi}{\omega_y^A - \omega_y^S}, \tag{4.42}$$

giving the periods of the envelope of the time signal. To apply these expressions to the numerical simulation of Figure 4.12 we insert the values of ω_x^S, ω_x^A, ω_y^S and ω_y^A for $d = 6a$ into Equations (4.39)–(4.42). Then we obtain $T_x = 1.52\tau_{Ai}$, $T_y = 1.52\tau_{Ai}$, $T_{bx} = 159.96\tau_{Ai}$

and $T_{by} = 479.88\tau_{Ai}$. The two oscillating periods are equal because the frequency distribution is approximately symmetric around the central value (the kink frequency of an individual loop) for sufficiently large distances (see Figure 4.8). The two beating periods derived from the numerical simulations match very well these values because Figure 4.17 gives $T_{bx}/4 \simeq 40\tau_{Ai}$ and $T_{by}/4 \simeq 120\tau_{Ai}$.

The $\pi/2$ phase difference between $\mathbf{v}_{right}$ and $\mathbf{v}_{left}$ (see Figures 4.12a and 4.12c) is due to the fact that our system of two loops basically behaves as a pair of driven-forced oscillators. Considering v_x, the left loop has initially a $\pi/2$ delay with respect to the right loop because it behaves as a driven oscillator and the left one like a forced oscillator. After half a beating period, $T_{bx}/2$, the roles are exchanged and the left loop becomes the driver and right one the forced oscillator. The y-components of $\mathbf{v}_{right}$ and $\mathbf{v}_{left}$ exhibit the same behaviour (see Figure 4.12c). This was already shown by Luna et al. (2006) in the case of two slabs (see Section 3.4.2).

As we have seen, the polarisation of the oscillations changes with time (see Movie 4 for an example). In the beating range, we can see this from the equations by calculating the scalar product of the velocity at the loop centres,

$$\begin{aligned}\mathbf{v}_{right}\cdot\mathbf{v}_{left} = & -C_x^2 \sin\left[2\left(\omega_x^A-\omega_x^S\right)t\right]\sin\left[2\left(\omega_x^A+\omega_x^S\right)t\right] \\ & -C_y^2 \sin\left[2\left(\omega_y^A-\omega_y^S\right)t\right]\sin\left[2\left(\omega_y^A+\omega_y^S\right)t\right].\end{aligned} \tag{4.43}$$

This product gives the relative polarisation of the loop oscillations and we see that it is zero at $t = 0$ and approximately zero for sufficiently small times. Thus, the left loop does not oscillate initially and it starts to oscillate perpendicularly to the right loop during the first oscillations. This feature is shown in Figure 4.11 and Movies 3 and 4.

Similar beating features are recovered for incidence angles of the initial disturbance in the range $0^\circ \leq \alpha \lesssim 50^\circ$ (what we call the beating range). The cause of this behaviour is explained by Figure 4.16: for these values of α a similar amount of energy is deposited in the S_x and A_x modes, so the beating of the v_x component is possible. Obviously, an analogous argument applies to v_y. This is not the case for $50^\circ \lesssim \alpha \leq 90^\circ$ for which the symmetric and antisymmetric modes receive different amounts of energy from the initial excitation and then their relative amplitude is different (see Figure 4.14 for an example). Simulations for angles $\alpha > 50^\circ$ do not clearly exhibit beating and the trajectories of the loops are much more complex than those in the beating range.

4.6 Discussion and conclusions

In this Chapter, we have investigated the transverse oscillations of a system of two coronal loops. We have considered the zero-β, ideal MHD equations and have studied both the normal modes of this configuration and the time-dependent problem. The results of this work can be summarised as follows:

1. The system has four fundamental normal modes, somehow similar to the kink mode of a single cylinder (see Section 4.1). These modes are collective, i.e. the system oscillates with a unique frequency, different for each mode. When arranged in increasing frequency, the modes are S_x, A_y, S_y and A_x, where S (A) stands for symmetric (antisymmetric) velocity oscillations with respect to the plane in the middle of the two loops and x (y) stands for the polarisation of motions. These modes produce transverse motions of the tubes, so they are kink-like modes.

2. We have studied the eigenfrequencies as a function of the separation of loops. For large distances between cylinders, they behave as two independent loops, i.e. the frequency tends to the individual kink mode frequency. When the distance decreases the frequency splits in four branches, two of which correspond to the S_x and A_y modes and are below the frequency of the individual tube and the other two are related to the S_y and A_x modes and lie above the kink frequency of a single tube.

3. For small distances between the loops, the frequency of the S_x and A_y modes is quite similar and tends to the internal cut-off frequency. This is different to the behaviour in a configuration of two slabs in which, for small distances between the slabs, the system behaves as an individual loop of double width (see Section 3.3). On the other hand, for the two cylinders the frequency is much smaller than that of a loop with double radius.

4. We have also studied the temporal evolution of the system after an initial planar pulse. We have shown that, depending on the incidence angle, the system oscillates with a combination of several normal modes. The frequencies of oscillation calculated from the numerical simulations agree very well with the normal mode eigenfrequencies.

5. In the beating range ($0^\circ \leq \alpha \lesssim 50^\circ$), the system beats in the x- and y-components of the velocity and the left and right loops are $\pi/2$ out of phase for each velocity component. They behave as a pair of driven-forced oscillators, with one loop giving energy to the other and forcing its transverse oscillations. The role of the two loops is interchanged every half beating period. On the other hand, for perturbations with $\alpha > 50^\circ$ the loop motions are much more complex than those in the beating range. The phase lag cannot be clearly appreciated and it strongly depends on the incidence angle of the initial pulse.

From this work, we conclude that a loop system can show a collective behaviour, its fundamental normal modes being quite different from those of the kink mode of a single loop. These collective normal modes are not a combination of individual loop modes. This suggests that the observed oscillations reported in Aschwanden et al. (1999, 2002); Schrijver et al. (2002); Verwichte et al. (2004) are in fact caused by one or a superposition of some collective modes. Moreover, the antiphase movements reported by Nakariakov et al. (1999) can be easily explained using our model. The same applies to the bounce movement of loops D and E studied in Verwichte et al. (2004). These motions can be interpreted by assuming that there is beating between the loops produced by the simultaneous excitation of the fundamental S_x and A_x modes.

It should be noted that the observations indicate a very rapid damping of transverse oscillations, such that in a few periods the amplitude of oscillation of the loops is almost zero. This fast attenuation may hide the beating produced by the simultaneous excitation of several normal modes of the system. However, in some situations, for example, for small loop separations and high density contrast loops, the beating periods decrease. Then, under such conditions the beating could be detectable in the observation interval. In any case, the beating is just one particular collective behaviour and there is always interaction between the individual loops in short time scales (typically of the order of $2d/v_{Ae}$). The consequences of this interaction are the collective normal modes of the system. The presence of the normal modes could be also clear from a frequency analysis. Unfortunately, due to the temporal resolution, these observations do not allow us to perform such analysis, but the frequency extraction method derived in Section 4.4.1 is suitable to be applied to the observations.

In this Chapter, we have studied two loops with exactly the same density and radii, and the next step is to analyse the behaviour of a system of a larger number of loops with different properties. This study can also be extended to understand the possible effect of the internal structure (multistranded models and small filling factors) on the oscillating loops by considering a set of very thin tubes with different densities and radii. These are the topics of the following two Chapters.

Chapter 5

Two and three non-identical loop model. T-matrix theory[1]

Following the previous Chapters it is necessary to increase the complexity of the systems of loops that we investigate. In this Chapter we expand the study of the collective normal modes from two identical cylindrical flux tubes to an arbitrary system of loops or strands with different physical and geometrical properties by using the scattering theory. The scattering theory, or its matricial formulation called T-matrix theory (see, e.g., Waterman and Truell, 1961; Waterman, 1969; Ramm, 1989), was first applied to magnetic tubes by Bogdan and Zweibel (1985). These authors studied the effect of inhomogeneous magnetic fields in sunspots on solar p-modes. The model consists in an infinite non-magnetised medium filled with an infinite number of identical magnetic fibrils distributed randomly. They found that the frequency is shifted with respect to the homogeneous case. Later, a similar study was made by Bogdan and Zweibel (1987) for an infinite half-space and in Bogdan (1987) for a slab filled with magnetic fibrils and the reflection and transmission of an acoustic plane-wave was studied in the half-space interphase and the slab, respectively. In Bogdan and Cattaneo (1989) the frequency shifts and velocity eigenfunctions were calculated for a cylindrical cavity randomly filled with distributions of up to 100 fibrils. The authors computed the frequency shifts by using the perturbation theory. Bogdan and Fox (1991) investigated the interaction of an acoustic plane-wave with a pair of identical uniformly magnetised flux tubes. The authors found that the scattered field differs significantly from that of only one tube. In Keppens et al. (1994) the scattering and absorption of sound waves by bundles of magnetic flux tubes, in the so-called spaghetti sunspot model was studied. The individual fibrils within the bundle have thin transition nonuniform layers. They found that the composite sunspot absorbs much more wave energy than its monolithic counterpart. In all these papers a non-magnetised external medium was considered.

In this Chapter we apply the T-matrix theory to a magnetic tube system with an ex-

---

[1] The novel results in this Section have been published in Luna et al. (2009)

ternal magnetised medium in order to extend previous works to coronal loop conditions. Our model consists of an ensemble of parallel cylinders, without gravity and curvature. The individual flux tubes have uniform transverse structure, but the nonuniform transition layers of Keppens et al. (1994) are not considered. We assume a uniform magnetic field in the loop and in the external or coronal media. This assumption allows the existence of fast MHD waves in the internal and the external medium also. Then, the individual flux tubes produce excitations of the other loops by means of fast waves. The stationary situation is governed by one or more fast collective normal modes. The T-matrix method allows us to explicitly compute the eigenvalues and eigenfunctions of these collective normal modes of the model.

The Chapter is organised as follows. In Section 5.1 the loop ensemble model and the equations for its dynamics are presented. In Section 5.2 we briefly describe the T-matrix theory and apply it to our model. With this method the exact eigenfrequencies and eigenmodes of two non-identical loops are investigated. The dependence of the interaction with the relative density and radii of the loops is studied in Section 5.3. The study of three identical aligned, equispaced loops is presented in Section 5.4. In the same Section the interaction between three non-identical loops is considered. Finally, in Section 5.5 the results are summarised and the main conclusions are drawn.

5.1 Theoretical model

The equilibrium configuration used to model the loop set is a system of N cylindrical, parallel homogeneous flux tubes, with the z-axis pointing in the direction of the loop axes. All loops have the same length, L, and each individual loop, labelled j, is characterised by the position of its centre in the xy-plane, $\mathbf{r}_j = x_j\mathbf{e}_x + y_j\mathbf{e}_y$, its radius, a_j, and its density, ρ_j. The density of the coronal environment is ρ_e. As in Chapter 4, the tubes and the external medium are permeated by a uniform magnetic field along the z-direction ($\mathbf{B}_0 = B_0\mathbf{e}_z$). The Alfvén speed, $v_A = B_0/\sqrt{\mu\rho}$, takes the value v_{Aj} inside the j-th loop and v_{Ae} in the surrounding corona ($v_{Aj} < v_{Ae}$).

Linear perturbations about this equilibrium for a perfectly conducting fluid can be readily described using the ideal MHD equations of Chapter 2. In particular we use Equation (2.29) to describe the magnetic pressure perturbations, p_T, defined by Equation (2.25). The line-tying effect is incorporated by setting $k_z = \pi/L$, and we concentrate on the fundamental mode, as we have seen in Section 1.3. We only consider problems for which the time dependence is a simple harmonic oscillation with frequency ω. Then, the magnetic pressure perturbation can be written in cylindrical coordinates as

$$p_T = e^{i(k_z z - \omega t)}\psi(r,\varphi), \tag{5.1}$$

where $\psi(r,\varphi)$ is a function that includes the dependence on r and φ. Inserting this expression in Equation (2.29), we obtain the scalar Helmholtz equation

$$\nabla_\perp^2\psi + k_\perp^2\psi = 0, \tag{5.2}$$

where $k_\perp$ is

$$k_\perp^2 = \frac{\omega^2 - k_z^2 v_A^2}{v_A^2}. \tag{5.3}$$

Hereafter, the $\perp$ symbol is dropped for the sake of simplicity.

5.2 T-matrix theory: Normal modes

The scattering theory, or its matricial formulation called T-matrix theory, provides an scheme to find analytically the normal modes of a system of scatterers in which waves are described by a Helmholtz equation (see Ramm, 1989; Waterman, 1969). We fulfil the T-matrix theory requirements because our ensemble of N loops can be considered a collection of scatterers and the perturbed magnetic pressure is described by Equation (5.2).

The T-matrix scheme states that the j-th flux tube generates an outgoing scattered wave, ψ_{sc}^j, in a field position $\mathbf{r}$ (in the two-dimensional xy-plane) that adds to the waves scattered from the other loops to produce the following net external field (Bogdan and Cattaneo, 1989),

$$\psi(\mathbf{r}) = \sum_j^N \psi_{sc}^j(\mathbf{r} - \mathbf{r}_j). \tag{5.4}$$

The scattered wave by the j-th loop is produced as a response of an exciting wave produced by the external field minus the contribution of the mentioned loop,

$$\psi_{ex}^j(\mathbf{r} - \mathbf{r}_j) = \psi(\mathbf{r}) - \psi_{sc}^j(\mathbf{r} - \mathbf{r}_j). \tag{5.5}$$

With Equations (5.4) and (5.5) the exciting field, ψ_{ex}^j, may be written entirely in terms of the scattered field, resulting in the self-consistency field equation (Bogdan and Cattaneo, 1989). This system of equations may then be closed by noting that the exciting and scattered fields are further related by linear operators, $\mathbf{T}^j$, that describe the scattering properties of the individual flux tubes (Bogdan and Cattaneo, 1989; Waterman, 1969; Ramm, 1989)

$$\psi_{sc}^j(\mathbf{r} - \mathbf{r}_j) = \mathbf{T}^j \psi_{ex}^j(\mathbf{r} - \mathbf{r}_j). \tag{5.6}$$

The key point is that the linear operators $\mathbf{T}^j$ depend exclusively on the individual loop and external medium properties and can be directly computed through the boundary conditions at the loop-external medium interphase as we will see below.

The external field to the j-th loop can be decomposed with Equation (5.5) as an excitation field on this loop and a scattered field by this loop. The excitation field has no sources in the j-th loop, i.e. it is the scattered field of the other loops, so it can be written as

$$\psi_{ex}^j(R_j, \varphi_j) = \sum_{m=-\infty}^{\infty} \alpha_m^j J_m(k_e R_j) e^{im\varphi_j}, \tag{5.7}$$

where α_m^j are the expansion coefficients of order m, that depend on the k_z wave number and the frequency ω and R_j and φ_j are the local polar coordinates centred at $\mathbf{r}_j$, defined through $R_j = |\mathbf{r} - \mathbf{r}_j|$ and $\cos\varphi_j = \mathbf{e}_x \cdot (\mathbf{r} - \mathbf{r}_j)/|\mathbf{r} - \mathbf{r}_j|$. Here J_m is the Bessel function of the first kind and order m and k_e is the wave number in the external medium calculated using Equation (5.3). With Equations (5.6) and (5.7), we find the scattered field in terms of an outgoing wave with sources at $\mathbf{r}_j$,

$$\psi_{sc}^j(R_j, \varphi_j) = \sum_{m=-\infty}^{\infty} T_{mm}^j \alpha_m^j H_m^{(1)}(k_e R_j) e^{im\varphi_j}, \tag{5.8}$$

where T_{mm}^j are the matrix diagonal elements of the operator $\mathbf{T}^j$ projected on the local basis, called T-matrix. The non-diagonal elements of this matrix are zero for axisymmetric tubes (Bogdan and Zweibel, 1985). The functions $H_m^{(1)}$ are the Hankel functions of the first kind. With Equations (5.4), (5.5), (5.7) and (5.8), we find the following expression for the total field

$$\psi(\mathbf{r}) = \sum_{m=-\infty}^{\infty} \alpha_m^j \left[J_m(k_e R_j) + T_{mm}^j H_m^{(1)}(k_e R_j) \right] e^{im\varphi_j}, \tag{5.9}$$

in which the external field to j-th loop is decomposed as an excitation on this loop and a scattered field by this loop (Waterman, 1969). In this work, we consider trapped modes, for which k_e is imaginary and the excitation field and the scattered field can be expanded in terms of the modified Bessel functions of the first kind (I_m) and second kind (K_m), respectively. However, this formalism also allows us to find the leaky modes. In order to keep the generality of the analysis, the notation based on the Bessel and Hankel functions is preserved.

Following the development of Bogdan and Cattaneo (1989), a linear algebraic system of equations for the complex coefficients α_m^j may then be obtained. We first substitute Equation (5.4) in Equation (5.5) in order to obtain the self-consistency requirement

$$\psi_{ex}^j(\mathbf{r} - \mathbf{r}_j) = \sum_{i \neq j}^{N} \psi_{sc}^i(\mathbf{r} - \mathbf{r}_i). \tag{5.10}$$

Next the exciting and scattered fields are replaced by their basis expansions, Equations (5.7) and (5.8), and the translation formula (see appendix of Bogdan and Cattaneo, 1989),

$$H_m^{(1)}(\mathbf{r} - \mathbf{r}_i) e^{im\varphi_i} = \sum_{n=-\infty}^{\infty} H_{m-n}^{(1)}(\mathbf{r}_j - \mathbf{r}_i) e^{i(m-n)\varphi_{ji}} J_n(\mathbf{r} - \mathbf{r}_j) e^{in\varphi_j}, \tag{5.11}$$

is used to express the scattered wave centred in the i-th loop into an excitation at j-th flux tube. φ_{ji} is the angle formed by the centre of the i-th loop with respect to the centre of the j-th flux tube. Finally, we obtain the following set of equations

$$\alpha_m^j + \sum_{i \neq j}^{N} \sum_{n=-\infty}^{\infty} \alpha_n^i T_{nn}^i H_{n-m}^{(1)}(k_e |\mathbf{r}_j - \mathbf{r}_i|) e^{i(n-m)\varphi_{ji}} = 0, \quad -\infty < m < \infty. \tag{5.12}$$

As we will see below with this equation we can find the α_m^j coefficients and the frequencies, ω, from which the spatial structure of the normal modes can be determined. From Equation (5.12), we see that the expansion coefficient of order m of the j-th loop, α_m^j, is coupled to all expansion coefficients of the other loops. This fact reflects the collective nature of the normal modes. With the α_m^j and Equations (5.4) and (5.8) we find the net external field.

The internal or transmitted field is

$$\psi_{tr}^j(\mathbf{r}-\mathbf{r}_j) = \sum_{m=-\infty}^{\infty} \beta_m^j J_m(k_j R_j) e^{im\varphi_j}, \tag{5.13}$$

where k_j is the perpendicular wave number inside the j-th loop calculated using Equation (5.3). The Bessel functions of the second kind, Y_m, are not considered in the expansion of the internal field (Equation 5.13) because they are singular at the loop axes. The transmitted field (Equation 5.13) can be calculated through the boundary conditions, namely the continuity of the magnetic pressure perturbation and the radial component of the velocity at $R_j = a_j$ (Equation 2.45). In terms of the ψ fields they are expressed as follows

$$\psi_{tr}^j(k_j R_j)|_{R_j=a_j} = \psi(k_e R_j)|_{R_j=a_j}, \tag{5.14}$$

$$\frac{\psi_{tr}^{j\,\prime}(k_j R_j)|_{R_j=a_j}}{k_j} = \frac{\psi'(k_e R_j)|_{R_j=a_j}}{k_e}, \tag{5.15}$$

where the prime is the derivative with respect to the function argument, $\psi'(x) = \partial\psi(x)/\partial x$.

Equation (5.12) is completely general for a system of N cylindrical flux tubes (see Keppens, 1994, for the expressions of the non-axisymmetric case) and all the information of the individual loops is included in the T-matrix elements, T_{mm}^j. These elements are calculated through the boundary conditions at the interphase between the loop and the external medium. With Equations (5.9), (5.13), (5.14) and (5.15) we find the T_{mm}^j element expression

$$T_{mm}^j = \frac{k_j{}^2 k_e J_m(k_j a_j) J_m'(k_e a_j) - k_e{}^2 k_j J_m'(k_j a_j) J_m(k_e a_j)}{k_e{}^2 k_j H_m^{(1)}(k_e a_j) J_m'(k_j a_j) - k_j{}^2 k_e H_m^{(1)\prime}(k_e a_j) J_m(k_j a_j)}. \tag{5.16}$$

Equation (5.16) is the generalisation of Bogdan and Zweibel (1985); Bogdan and Cattaneo (1989) to the case of a magnetised external environment.

Finally, note that with the boundary conditions (Equations 5.14 and 5.15) it is possible to calculate the β_m^j coefficients

$$\beta_m^j = \frac{J_m(k_e a_j) + T_{mm}^j H_m^{(1)}(k_e a_j)}{J_m(k_j a_j)} \alpha_m^j, \tag{5.17}$$

which can be inserted into Equation (5.13) to obtain the internal field, ψ_{tr}^j.

From the previous theory, the results of a single oscillating loop can be retrieved (see Section 4.1). The second term of the left hand side of Equation (5.12) is zero and this implies that $\alpha_m^j = 0$. In order to have a non-zero external solution (Equation 5.8), the products $T_{mm}^j \alpha_m^j$ must be finite and arbitrary. This implies that the T_{mm}^j elements are singular at the eigenfrequencies of the isolated loop. This is the behaviour found in Equation (5.16), since the zeroes of the denominator correspond to the dispersion relation of the individual loop (see Equation 4.17).

Equation (5.12) is formally an infinite system of equations for an infinite number of unknowns (α_m^j). In order to solve it, we truncate the system into a finite number of equations and unknowns by setting $\alpha_{m_t+1}^j = 0$ for azimuthal numbers greater than a truncation number ($m > m_t$). To ensure the convergence of solutions, they must be independent of the truncation number m_t. With these considerations, the solution of Equation (5.12) reduces to solving a homogeneous linear system of $N(2m_t + 1)$ equations and $N(2m_t + 1)$ unknowns. For this system of equations to have a non-trivial solution, its determinant must be zero. This requirement gives the dispersion relation as a transcendental equation. We solve the dispersion relation numerically and find the frequencies of the normal modes and with these frequencies we calculate the α_m^j expansion coefficients. With Equations (5.4) and (5.13) we find the net field in the external medium and the transmitted field in each loop. In all our calculations, solutions are independent of the truncation number for values $m_t > 5$ but we fix this number to $m_t = 20$ to more confidently ensure their convergence. With the method presented here we have obtained the results of the following Sections. We apply the method outlined before to a system of two loops. Equation (5.12) can be written as

$$\mathbf{M}\alpha = 0, \tag{5.18}$$

where the matrix $\mathbf{M}$ is

$$\mathbf{M} = \left[\begin{array}{ccc|ccc}
1 & \cdots & 0 & T^2_{-m_t,-m_t}H_0^{(1)}(k_e r_{12}) & \cdots & T^2_{m_t,m_t}H_{-2m_t}^{(1)}(k_e r_{12}) \\
\vdots & \ddots & \vdots & \vdots & \ddots & \vdots \\
0 & \cdots & 1 & T^2_{-m_t,-m_t}H_{2m_t}^{(1)}(k_e r_{12}) & \cdots & T^2_{m_t,m_t}H_e^{(1)}(k_e r_{12}) \\
\hline
T^1_{-m_t,-m_t}H_0^{(1)}(k_e r_{21}) & \cdots & T^1_{m_t,m_t}H_{2m_t}^{(1)}(k_e r_{21}) & 1 & \cdots & 0 \\
\vdots & \ddots & \vdots & \vdots & \ddots & \vdots \\
T^1_{-m_t,-m_t}H_{-2m_t}^{(1)}(k_e r_{21}) & \cdots & T^1_{m_t,m_t}H_e^{(1)}(k_e r_{21}) & 0 & \cdots & 1
\end{array}\right],$$

and the vector α is

$$\alpha = \begin{bmatrix} \alpha^1_{-m_t} \\ \vdots \\ \alpha^1_0 \\ \vdots \\ \alpha^1_{m_t} \\ \alpha^2_{-m_t} \\ \vdots \\ \alpha^2_0 \\ \vdots \\ \alpha^2_{m_t} \end{bmatrix}.$$

Here, $r_{12} = r_{21} = |\mathbf{r}_1 - \mathbf{r}_2| = |\mathbf{r}_2 - \mathbf{r}_1|$ is the separation between the centres of the loops 1 and 2. Equation (5.18) is a homogeneous set of equations and as we have seen previously the determinant of the coefficient matrix ($\mathbf{M}$) must be zero,

$$\det \mathbf{M} = 0 \ . \tag{5.19}$$

This equation gives the dispersion relation of the collective normal modes, from which we find their frequencies numerically. With these frequencies, we find the coefficients α_m^j through Equation (5.18) and reconstruct the external field with Equations (5.8) and (5.4) and the internal field with Equations (5.17) and (5.13). The method outlined here is fully general for an arbitrary loop system but the $\mathbf{M}$ matrix is different and depends on the system considered. We have developed a general FORTRAN code in order to find the normal modes of an arbitrary loop system. In the following Sections we show several examples with different configurations.

5.3 Interaction between two loops

First, we compute the normal modes of two non-identical loops with the T-matrix theory outlined in Section 5.2. In this Section we study the dependence of the interaction as a function of the density and radii of the loops. We consider a system of two loops with radii $a_1 = a_2 = a = 0.03L$ and separated a distance $d = 3a$. The first loop density is $\rho_1 = 3\rho_e$ while ρ_2 is allowed to change from $\rho_2 = \rho_e$ to $5\rho_e$ to study its influence on the normal mode properties. We concentrate on the kink-like modes in which the individual loops move more or less as kink and suffer the largest transverse displacement (see Section 4.1). We find four kink-like normal modes, two with motions polarised in the x-direction and moving in phase and antiphase with different amplitudes, and other two with the same properties but polarised in the y-direction. In the case of two identical tubes (see Chapter 4 and Luna et al., 2008) the four kink-like solutions are either symmetric or antisymmetric with respect to the y-axis and for this reason they are called S_x, A_x, S_y and A_y. The present system consists of two non-identical loops and so the kink-like modes have different amplitude in each tube. In order not to introduce extra notation, we generalise the meaning of S and A to motions in phase or antiphase, respectively, so that the modes are still referred to as S_x, A_x, S_y and A_y. The frequencies of oscillation of these four modes as a function of ρ_2/ρ_e are displayed in Figure 5.1. The bottom solid line is associated to the S_x and A_y modes, which almost have the same frequency (see inbox in Figure 5.1). The same behaviour is found for the top solid line, which corresponds to the S_y and A_x modes. We see that the collective normal modes (solid lines) do not coincide with the kink frequencies of the individual loops (dashed lines), a discrepancy caused by the interaction between loops. This interaction is maximal when $\rho_2 = \rho_1$ (dotted line) and the normal modes S_x, A_y, S_y and A_x become the modes reported in Section 4 and Luna et al. (2008) with identical amplitude in each loop. The opposite situation takes place when ρ_2 is sufficiently different from ρ_1: the collective frequencies are closer to the

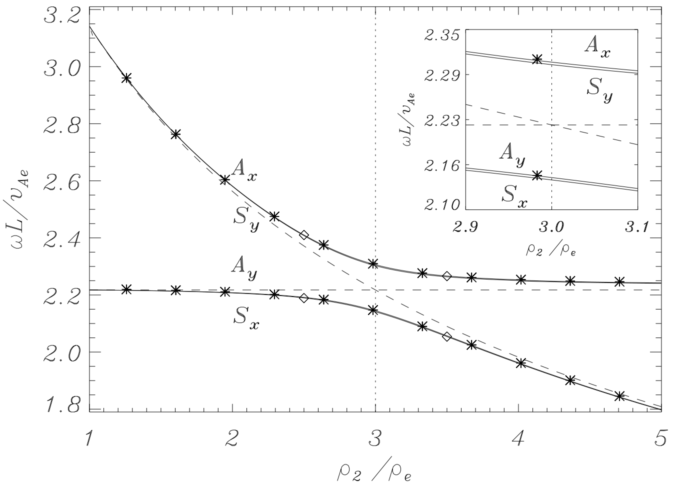

Figure 5.1: Dimensionless frequency, $\omega L/v_{Ae}$, as a function of the internal density of the second loop. The bottom solid line is associated to the two kink-like normal modes S_x and A_y, which have very similar frequencies. In the same way, the upper solid line is associated to the S_y and A_x modes. In the inner plot a detailed view for $\rho_2 \approx \rho_1$ is displayed showing that the solid lines are in fact double lines. The two dashed lines are the individual kink frequencies of each loop. We see that the kink frequency of loop 1 is constant and the frequency of loop 2 decreases with ρ_2, because ρ_1 is constant and ρ_2 changes. The vertical dotted line is plotted at $\rho_2 = \rho_1$. Diamonds mark the frequencies of the modes represented in Figure 5.2. The asterisks mark the frequencies computed with the analytical Equation (5.20) derived by Van Doorsselaere et al. (2008c).

individual kink frequencies and the system behaves as a pair of independently oscillating loops. In this regime, the S_x and A_y modes correspond to the individual oscillations of the denser loop in the x- and y-direction, respectively, and possess identical frequencies, whereas the S_y and A_x modes are the individual oscillations of the rarer loop in the x- and y-direction, respectively, and also share the same frequency. Figure 5.1 can be interpreted globally as an avoided crossing of the kink modes of the loops: far from the coupling, each branch is associated to the individual loop kink mode, but near the avoided crossing motions are associated to the two loops to produce four collective kink-like modes. As long as kink-like solutions are concerned, loops interact for densities approximately in the range $\rho_2 = 2\rho_e$ to $4\rho_e$.

The magnetic pressure perturbation of the S_x and A_x modes is plotted in Figure 5.2 for two cases in which the loop interaction is important ($\rho_2 = 2.5\rho_e$ and $3.5\rho_e$). The behaviour of the other two modes, A_y and S_y, is analogous to that of the S_x and A_x modes and thus their spatial structure is not shown. In contrast to the case $\rho_1 = \rho_2$, in which the interaction is maximal and thus the two loops oscillate with equal amplitudes (see Figure 4.7) the solutions in Figure 5.2 display an imbalance in the oscillatory amplitude of the

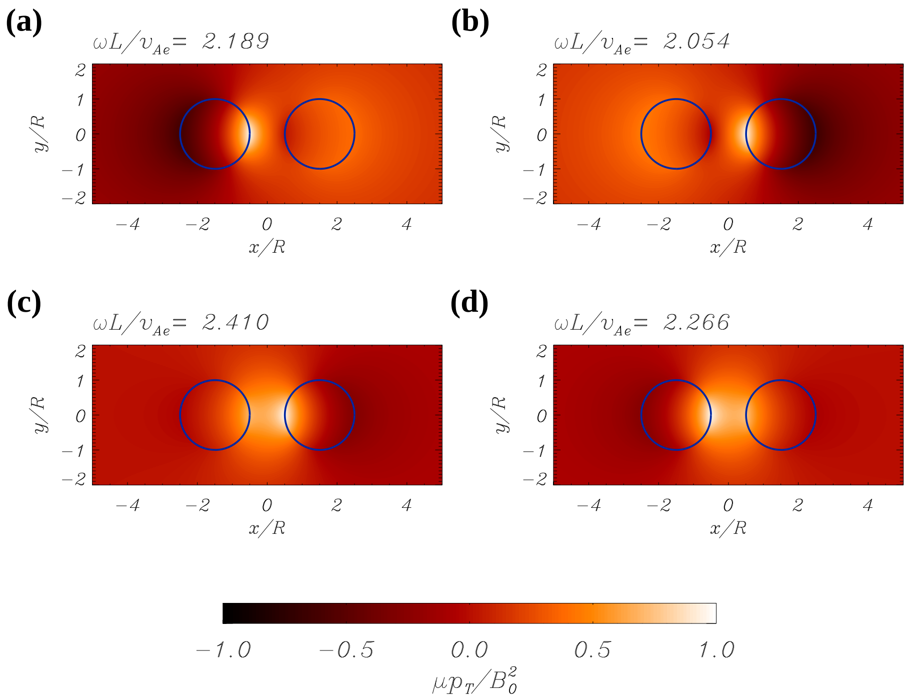

Figure 5.2: Total pressure perturbation of the fast collective normal modes S_x and A_x (plotted in the xy-plane) for a fixed density of the left loop ($\rho_1 = 3\rho_e$) and different densities of the right loop (ρ_2). The panels show the S_x mode for **(a)** $\rho_2 = 2.5\rho_e$ and **(b)** $\rho_2 = 3.5\rho_e$; the A_x mode for **(c)** $\rho_2 = 2.5\rho_e$ and **(d)** $\rho_2 = 3.5\rho_e$. The frequencies of the modes are given on top of the corresponding panels. The dotted lines show the boundaries of the unperturbed tubes. Regions of the positive (negative) perturbed magnetic pressure represent density enhancements (decrements), so that in **(a)** and **(b)** the loops move in phase in the x-direction, while in **(c)** and **(d)** they move in antiphase in the x-direction.

two loops. The largest amplitude of the pressure perturbation corresponds to the denser loop for the S_x mode (see Figures 5.2a and 5.2b), while it occurs in the rarer loop for the A_x mode (see Figures 5.2c and 5.2d).

Secondly, we consider the same system of two loops but now the densities are fixed to $\rho_1 = \rho_2 = 3\rho_e$, the radius of the left loop is $a_1 = 0.03L$ and the right loop radius, a_2, is allowed to vary. The distance between the tube centres is $3a_M$, where a_M is the averaged radius defined as $a_M = (a_1 + a_2)/2$. With this condition the separation measured in averaged radius units is constant. The frequencies of the four modes S_x, A_y, S_y and A_x are plotted in Figure 5.3. As in Figure 5.1, the collective frequencies (solid lines) are different from the individual kink frequencies (dashed lines), showing the collective nature of the oscillations. The chosen range of radii are those measured in TRACE observations of transverse oscillations (see, e.g., Aschwanden et al., 2003). In Figure 5.3 we see that the collective frequencies are more or less constant; moreover the amplitude of the oscillation is more or less equal in each tube. Then, in the considered range of radii the interaction between kink modes is strong and does not significantly depend on the loop radii.

In Van Doorsselaere et al. (2008c) an analytical approximation of the eigenfrequencies and eigenmodes of the present problem has been derived in the long-wavelength limit. They have found the four collective normal modes, but the S_x and A_y have a degenerate frequency ω_- and the S_y and A_x a degenerate frequency ω_+. The authors found an explicit expression for the two degenerate frequencies,

$$\omega_\pm^2 = \rho_e\, k_z^2 v_{Ae}^2\, \frac{\rho_1 + \rho_2 + 2\rho_e \pm \sqrt{(\rho_1 - \rho_2)^2 + 4(\rho_1 - \rho_e)(\rho_2 - \rho_e)E^2}}{(\rho_1 + \rho_e)(\rho_2 + \rho_e) - (\rho_1 - \rho_e)(\rho_2 - \rho_e)E^2} \tag{5.20}$$

where $E = e^{-(\tau_1+\tau_2)}$, $\tau_1 = \operatorname{arccosh}\left(\frac{d^2+a_1^2-a_2^2}{2a_1 d}\right)$ and $\tau_2 = \operatorname{arccosh}\left(\frac{d^2+a_2^2-a_1^2}{2a_2 d}\right)$. The frequencies obtained with this expressions are plotted with asterisks in Figures 5.1 and 5.3. We find a very good agreement between the approximate values and the T-matrix results. The results of Van Doorsselaere et al. (2008c) are a good approximation because we fulfil the long-wavelength condition in the range of a/L and d/L considered here. However, the Van Doorsselaere et al. (2008c) method is limited to two loop systems because they use bicylindrical coordinates to find the eigenfrequencies and eigenfunctions. Then, this method is not applicable, for example, in the following Section 5.4, in which a system of three loops is considered or in Chapter 6, in which the normal modes of more than ten strands are computed. In addition, the Van Doorsselaere et al. (2008c) results disagree with those of Section 4.2 in which all the four modes have different frequencies because the long-wavelength limit is not fulfilled.

5.4 Interaction between three loops

5.4.1 Equal loop densities

We first study the situation in which the density and radii of the loops is the same and find that there are eight kink-like normal modes, whose eigenfunctions are plotted in Figure 5.4, with the modes ordered by increasing frequency. The lowest frequency corresponds to a mode in which the three loops move in phase in the x-direction (Figure 5.4a), whereas in the highest frequency mode (Figure 5.4h) the three loops move in phase in the y-direction. This behaviour is different from that of the system of two loops (see Section 5.3), in which the higher frequency mode corresponds to the A_x instead of the S_y mode. The modes of Figures 5.4a, 5.4b, 5.4g and 5.4h are kink-like while the other four modes of Figures 5.4c, 5.4d, 5.4e and 5.4f combine kink and fluting oscillations: the two left and right loops oscillate with a kink-like motion whereas the central loop oscillates with a fluting motion. We also refer to these modes as kink-like because at least one loop oscillates with a kink-like behaviour. In these modes the central loop contributes appreciably to the total field (Equation 5.8) with the multipole $m = 2$ (see Figure 4.4). Between the

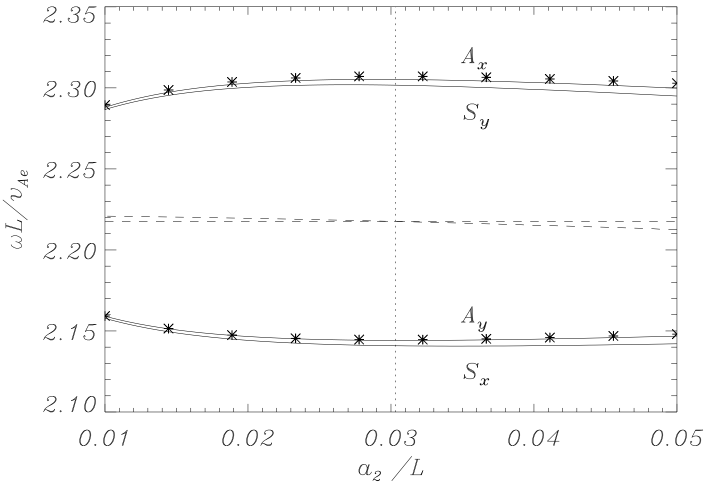

Figure 5.3: Dimensionless frequency, $\omega L/v_{Ae}$, of the four collective kink-like modes S_x, A_y, S_y and A_x (solid lines), as a function of the normalised right loop radius, a_2/L. As in Figure 5.1, the two individual kink frequencies are plotted (dashed lines), where the horizontal dashed line corresponds to the left loop and the one with a slight dependence on a_2 corresponds to the right loop. The asterisks mark the frequencies computed with Equation (5.20) derived by Van Doorsselaere et al. (2008c).

frequencies of the modes plotted in Figures 5.4d and 5.4e there are modes with the three loops oscillating with fluting motions and even with more complex structure associated to $m > 2$ solutions. Then we call these modes fluting-like. They are not further analysed because they do not produce transverse displacements of the loops.

5.4.2 Different loop densities

Now we consider the dependence of the interaction on the loop density. The loop radii are fixed to $a_1 = a_2 = a_3 = a = 0.03L$, the separation between adjacent loop centres is $d = 3a$, the densities of loops 1 and 2 are fixed to $\rho_1 = 3\rho_e$ and $\rho_2 = 2\rho_e$ and ρ_3 is allowed to change from ρ_e to $4\rho_e$. Six kink-like normal modes, rather than eight, are found and their frequencies are plotted as a function of ρ_3 in Figure 5.5. There are six branches associated to the six kink-like modes, that have been labelled m_1 to m_6 starting with the lowest frequency mode. We have chosen ρ_1 and ρ_2 in such a way that loops 1 and 2 are basically decoupled (see Section 5.3). Figure 5.5 is similar to Figure 5.1 and can be interpreted as two avoided crossings of the individual kink modes of the three loops. Far from the couplings, the loops behave independently. This fact is illustrated in Figure 5.6. In this figure we have plotted the modes associated to the branches m_2, m_3 and m_6 in the top, central and bottom rows, respectively. The modes m_1, m_4 and m_5 have an equivalent behaviour and have not been plotted. Far from the coupling region the m_1 and

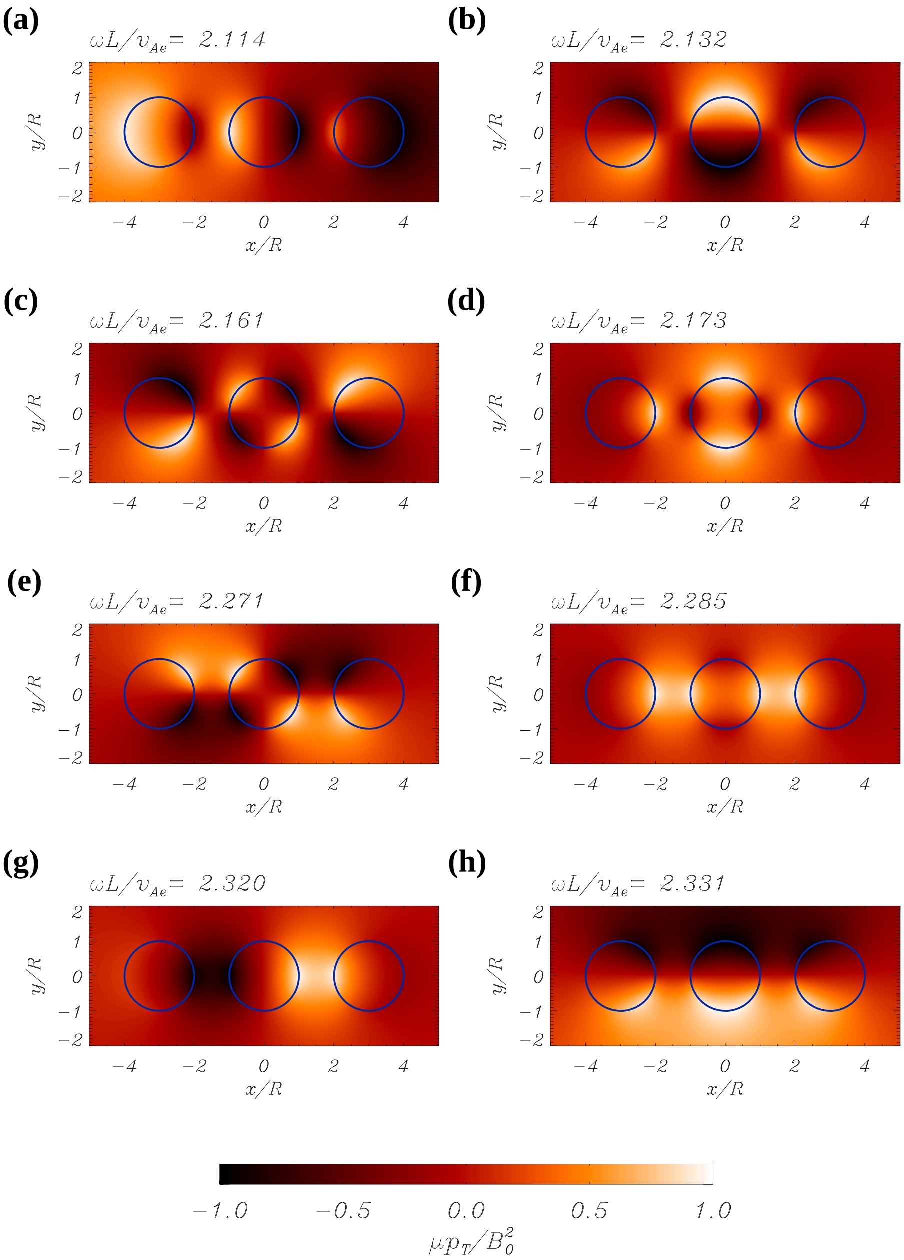

Figure 5.4: Total pressure perturbation of the eight kink-like collective normal modes of three identical loops. The densities are fixed to $\rho_1 = \rho_2 = \rho_3 = 3\rho_e$, the radii to $a_1 = a_2 = a_3 = a = 0.03L$ and the separation between adjacent loops is $d = 3a$.

m_2 solutions are associated to the individual kink oscillations of the denser loop in the x- and y-direction, respectively. In the same way, the branches m_3 and m_4 are associated to the individual kink mode of the intermediate density loop and the branches m_5 and m_6 to the individual kink oscillations of the rarest loop. On the other hand, at the couplings

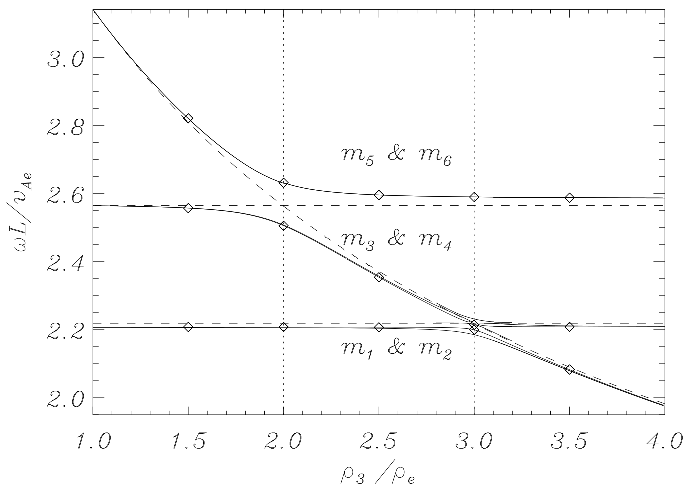

Figure 5.5: Same as Figure 5.1 for the collective frequencies of three aligned, equispaced loops plotted as a function of the density of loop 3. Solid lines correspond to the frequencies of the six collective kink-like modes. Dashed lines correspond to the individual kink frequencies of the loops. The horizontal bottom and upper dashed lines correspond to the kink frequencies of loops 1 and 2, respectively. The other dashed curve corresponds to the kink frequency of the third loop, with variable density ρ_3. Diamonds mark the frequencies of the modes represented in Figures 5.6 and 5.7.

the loops interact by pairs as we see in Figure 5.7. The interacting pair oscillates with a collective normal mode whereas the other loop oscillates individually. In the first avoided crossing, for $\rho_3 = \rho_2 = 2\rho_e$, the branches m_3 and m_4 are coupled with m_5 and m_6 (see Figure 5.5), associated to loops 2 and 3, that oscillate collectively as we see in Figures 5.7c and 5.7e. The branches m_1 and m_2 are uncoupled and loop 1 oscillates independently from the other two, as we see in Figure 5.7a. In the second avoided crossing at $\rho_3 = \rho_1 = 3\rho_e$ the branches m_1 and m_2 are coupled with m_3 and m_4, while m_5 and m_6 are independent. Therefore, in this avoided crossing the interaction is between loops 1 and 3 (Figures 5.7b and 5.7d) and loop 2 oscillates independently (Figure 5.7f). It is important to note that the collective modes of the two coupled tubes have a different frequency ordering with respect to the case of two loops, studied in Section 5.3, because of the presence of loop 1.

Comparing Figures 5.1 and 5.5 the coupling regions occur in a narrower range of density values in the three loop system than for two tubes. The physical meaning is that only loops with similar densities are coupled in the three loop ensemble. In this system, it is important to note that in the second avoided crossing at $\rho_3 \approx \rho_1$ loop 2 does not participate of the collective dynamics despite being the closest tube to the interacting loops.

The results discussed so far in this Subsection correspond to different densities of loops 1 and 2. Nevertheless, if the densities of loops 1 and 2 are similar, their interaction

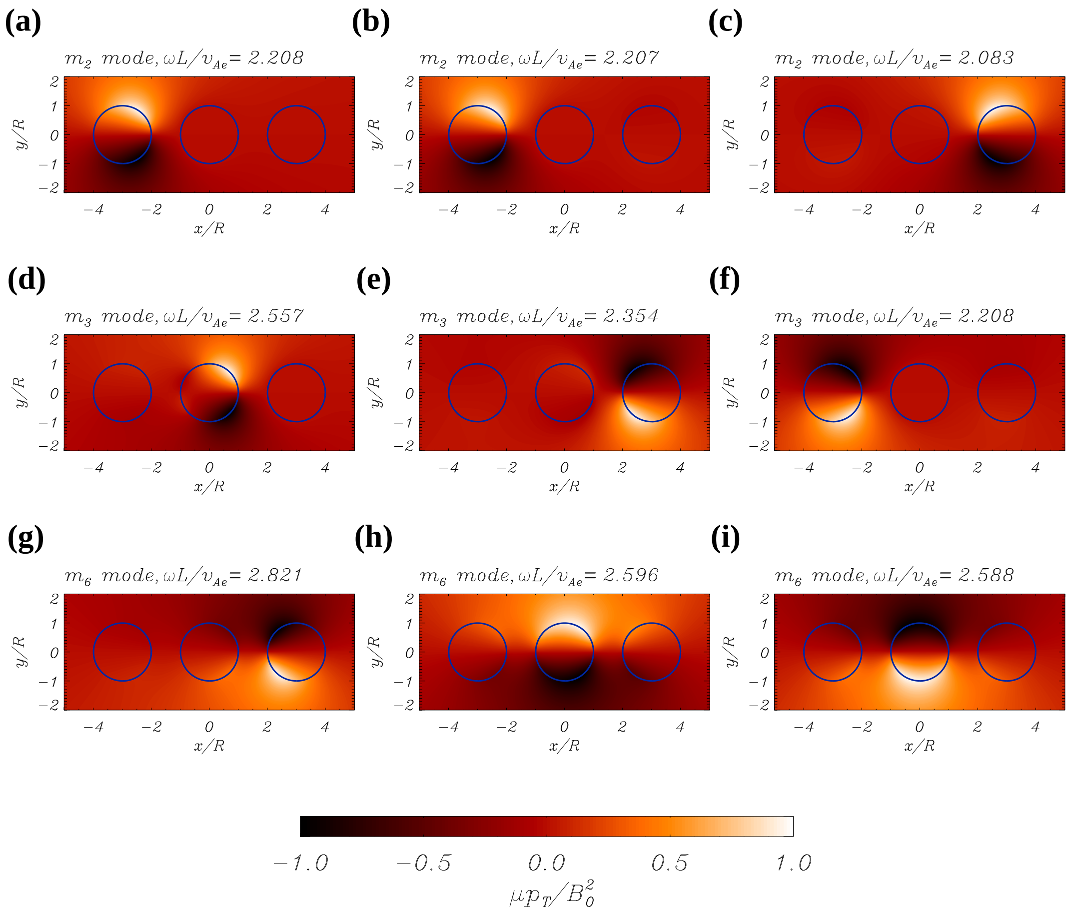

Figure 5.6: Same as Figure 5.4 for three values of ρ_3 far from the two coupling regions of Figure 5.5. The densities of loops 1 and 2 are fixed to $\rho_1 = 3\rho_e$ and $\rho_2 = 2\rho_e$ and ρ_3 is allowed to change. The loop radii are fixed to $a_1 = a_2 = a_3 = 0.03L$. In the top, central and bottom rows of panels the m_2, m_3 and m_6 modes are plotted for **(a)**, **(d)** and **(g)** $\rho_3 = 1.5\rho_e$; **(b)**, **(e)** and **(h)** $\rho_3 = 2.5\rho_e$; **(c)**, **(f)** and **(i)** $\rho_3 = 3.5\rho_e$.

is more important and the description of the dispersion diagram and the normal modes of the system is much more complex. In this case, there are eight kink-like normal modes. In this situation there are not only interactions between pairs of loops but also interactions between three loops. There are modes associated to the ensemble formed by tubes 1 and 2, individual oscillations of the cylinder 3 and the ensemble of the three loops depending on ρ_3. A particular case of this situation is the three identical loops previously discussed (Section 5.4.1) in which all modes are associated to the collectivity.

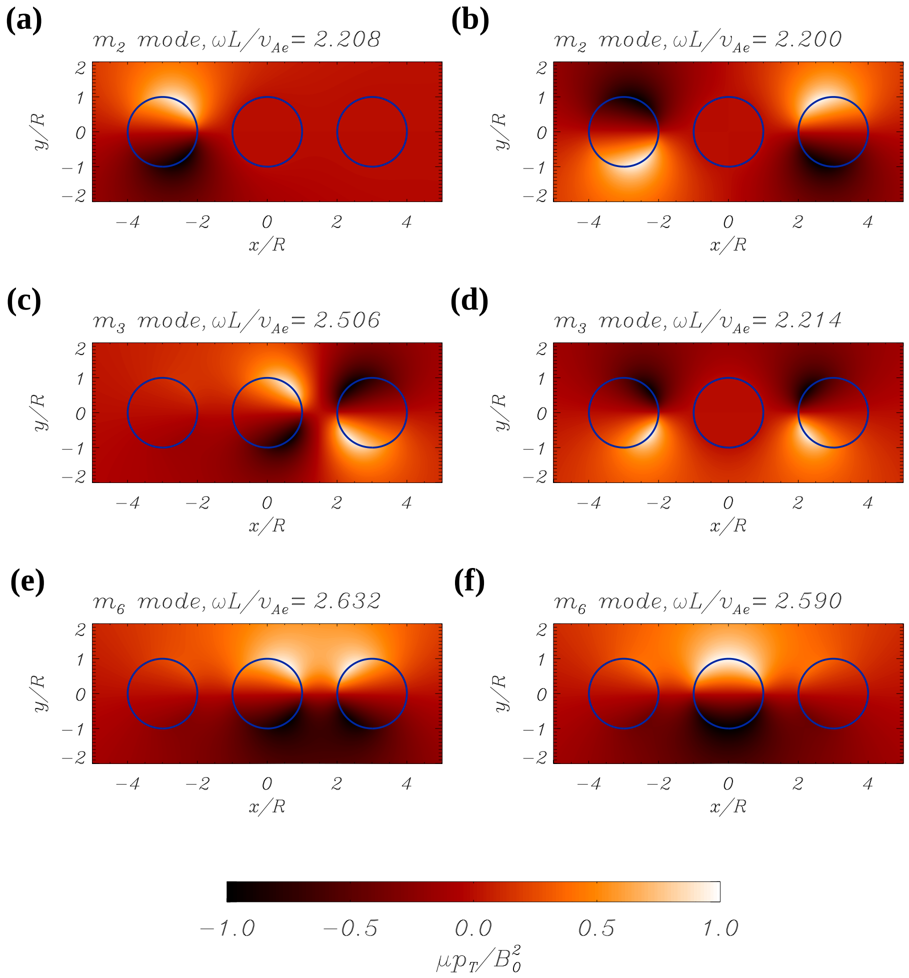

Figure 5.7: Same as Figure 5.4 for two values of ρ_3 at the maximal coupling (Figure 5.5). In the top, central and bottom rows of panels the m_2, m_3 and m_6 modes are plotted for **(a)**, **(c)** and **(e)** $\rho_3 = 2\rho_e$; **(b)**, **(d)** and **(f)** $\rho_3 = 3\rho_e$.

5.5 Discussion and conclusions

In this Chapter we have investigated the kink-like normal modes of a system of several loops with the help of the T-matrix theory. The results of this work can be summarised as follows:

1. In the system of two non-identical loops, we have found four kink-like normal modes S_x, A_y, S_y and A_x. The frequencies of the S_x and A_y solutions are very similar as well as the frequencies of the S_y and A_x modes. This result agrees with Van Doorsselaere et al. (2008c), who considered thin tubes (i.e. long wavelength approximation). For fat loops the S_x and A_y modes, as well the S_y and A_x, have

different frequencies, as was shown in Chapter 4 and Luna et al. (2008). These collective normal modes are related with the standing-channel scattering resonances discussed in Bogdan and Fox (1991) and Keppens (1994).

2. For a system of two loops we have investigated the dependence of the interaction between kink oscillations as a function on the relative density of the loop pair. For $\rho_1 = 3\rho_e$ we have found that the oscillations of the loops are coupled in the range of ρ_2 between $2\rho_e$ to $4\rho_e$ and that the coupling is maximum for $\rho_2 = \rho_1 = 3\rho_e$. Outside this density range the loops are essentially decoupled and oscillate independently.

3. We have also studied the dependence of the interaction with the relative radii of the loops. We have seen that in the range of radii for which transverse loop oscillations have been observed the interaction depends very little on this parameter and the loops strongly interact for all the radii considered. The explanation of this behaviour is that in our loops the thin loop approximation can be applied and in this situation the kink frequency depends on the tube density and not on the radii.

4. In the case of a system of three equal, aligned, equispaced loops there are eight kink-like normal modes. The lower frequency mode corresponds to the three loops oscillating in phase in the x-direction, i.e. along the direction in which their axes are aligned, in agreement with the results of two identical loops. On the other hand, the upper frequency mode corresponds to the three loops oscillating in phase in the y-direction. This does not agree with the two identical loop situation, in which the upper mode corresponds to the two loops oscillating in antiphase in the x-direction. In fact, this property of the three-loop system is also true for ensembles of four or more aligned loops.

5. We have made a parametric study of the kink-like modes in a system of three loops with equal radii and different densities by changing the density of loop 3, ρ_3. We have chosen $\rho_1 = 3\rho_e$ and $\rho_2 = 2\rho_e$ so that the interaction between loops 1 and 2 is negligible. We have found that the oscillations of loop 3 are coupled with loop 2 when $\rho_3 \approx \rho_2$, whereas loop 1 oscillates independently. Furthermore, loop 3 couples with loop 1 when $\rho_3 \approx \rho_1$ with loop 2 oscillating independently. If ρ_3 takes different values, the system is decoupled and the three loops oscillate independently.

In this Chapter, we have found that the interaction between loops regarding kink-like motions depends strongly on the their individual kink frequencies. If these frequencies are similar, loop motions are coupled and the normal modes are collective. On the other hand, if the loop kink frequencies are quite different their motions are not coupled. Since the individual frequencies depend on the loop density and radius, we have studied separately the influence of the two parameters. We have found that if the densities are quite similar, loops are coupled and the oscillations are collective. On the other hand, if the densities are quite different, the tubes oscillate independently. The range of densities for which the loops are coupled depends on the system properties and in the configuration of three loops this range is narrower than in the two tubes configuration.

From the results shown in this Chapter we suggest that the antiphase motions reported in Schrijver and Brown (2000); Schrijver et al. (2002) are collective motions and, therefore, that the individual kink frequencies are similar but different from the collective observed frequency. If the loop model presented here is valid, both loop densities are also similar. In addition, in Verwichte et al. (2004) a loop arcade is studied and three groups of tubes oscillating with similar frequencies can be appreciated. The dynamics of each group of tubes can be interpreted as collective, although a detailed study of such configuration is needed to relate the loop characteristics and the frequency of oscillation of the group. On the other hand, loops not belonging to these three groups do not share their frequencies with other loops and so oscillate independently. This has to be interpreted as a sign that these loops have different densities from those of the rest of the loops. It must be mentioned that in Verwichte et al. (2004) all the oscillations are assumed as individual, but this is only true in the case of loops that do not share their frequency. For example, if the loops actually oscillate with the lowest frequency collective mode, the assumption of individual motion might produce an underestimation of the magnetic field or an overestimation of the loop density.

The T-matrix method shown in this Chapter can be easily applied to more complex configurations with gas pressure and tubes with flows or, following Keppens et al. (1994), with thin non-uniform layers. However, here we neglect these effects and consider a more complex system using the multistranded loop model in the following Chapter.

Chapter 6

Transverse oscillations of a multistranded loop model

In Section 1.2 we have pointed out that the nature and detailed structure of loops is not yet well understood. Recent observations suggest that coronal loops could be made up by filaments called strands. Here we consider a multistranded loop with a fine structure that is formed by several tens or hundreds of strands considered as miniloops and for which the plasma heating properties are approximately uniform in the transverse direction (see Section 1.2). In this Chapter we apply the techniques and results of Chapter 5 and find the collective normal modes of different ensembles of strands. The aim of this Chapter is to discuss the implications of the fine structure on the global transverse motion of loops.

This Chapter is organised as follows. In Section 6.1, the multistranded loop model is presented. In Section 6.2, the normal modes of a system of ten identical strands are found, while the same is done for ten non-identical tubes in Section 6.3. In Section 6.4, a much more complex configuration, namely a loop made of 40 strands, is investigated. Finally, in Section 6.5 the results are discussed and the main conclusions are drawn.

6.1 Theoretical model

In this Chapter a coronal loop is assumed to be a composite structure of several strands. Each coronal strand is modelled as a straight cylinder without gravity and uniform density along the tube with the loop feet tied in the photosphere. The multistranded loop configuration consists of a bundle of N cylindrical, parallel, homogeneous strands. The z-axis points in the direction of the strands axes. All strands have the same length, L, and each individual strand, labelled as j, is characterised by the position of its centre in the xy-plane, $\mathbf{r}_j = x_j\mathbf{e}_x + y_j\mathbf{e}_y$, its radius, a_j, and its density, ρ_j. The position of each strand is randomly generated within a hypothetical unresolved loop of radius R (see Figure 6.1). The density of the coronal environment is ρ_e. Similarly to Chapter 5, the uniform magnetic equilibrium field is $\mathbf{B}_0 = B_0\mathbf{e}_z$ inside the strands and in the coronal medium. A harmonic time dependence of the perturbations $e^{-i\omega t}$ is assumed and the z-dependence of the form $e^{ik_z z}$, with $k_z = \pi/L$ (line-tying effect). With all the assumptions discussed here the governing equations of our system reduce to a scalar Helmholtz equation for the magnetic pressure (see Equation 5.2).

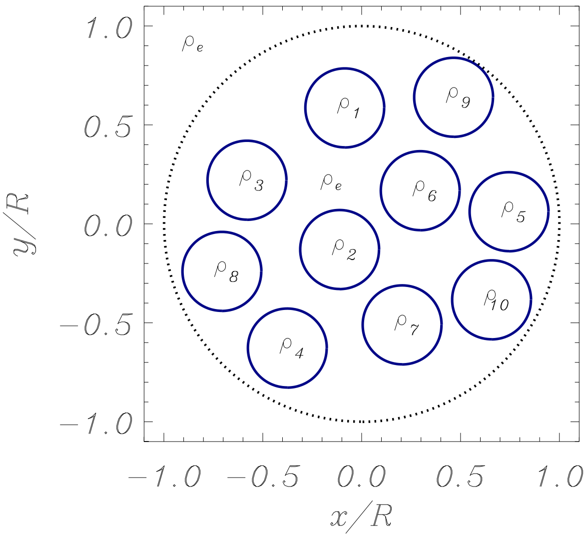

Figure 6.1: Sketch of the cross section of a multistranded loop model, which consists of a loop of radius R (large dotted circle) filled with N homogeneous strands of densities ρ_j and radius a_j (solid smaller circles). The external medium to the loop and the medium between strands consist of coronal material with density ρ_e. It is important to note that the large dotted circle is not real and represents the external boundary of a hypothetical unresolved loop.

In order to compare the dynamics of a multistranded loop model with that of a monolithic tube, an equivalent flux tube is defined. The flux tube radius, R, corresponds to size of the cylinder that wraps the strand bundle (see Figure 6.1). An equivalent density is defined as

$$\rho_{eq} = \sum_{j=1}^{N} \rho_j \left(\frac{a_j}{R}\right)^2 + \rho_e \left[1 - N\left(\frac{a_j}{R}\right)^2\right] , \tag{6.1}$$

so that the equivalent monolithic loop has the same mass as the multistranded loop. We have fixed the radius of the cylinder envelop to $R = 0.03L$, that is a typical value for coronal loops (see Aschwanden et al., 2003). We have assumed the volume filled by the strands is 40% that of the monolithic loop. In addition, all the strands have the same radius, $a_j = 0.2R = 0.006L$.

6.2 Normal modes of ten identical strands

We first study a system of $N = 10$ identical strands, i.e. with identical densities and radii. From the results of Chapter 5, this is the situation for which the coupling between strands is stronger because all the tubes have identical individual kink frequencies, ω_{strand}. The density of each strand is fixed to $\rho_j = 7.5\rho_e$ in order to have an equivalent density $\rho_{eq} = 3.6\rho_e$ (see Equation 6.1). The equivalent monolithic loop has an individual kink frequency $\omega_{mono} = 2.067 v_{Ae}/L$ computed with the fast wave dispersion relation in a cylinder (see Equation 4.17). Hereafter, all the frequencies will be expressed in terms of this frequency. The individual kink frequency of each strand is then $\omega_{strand} = 0.737\omega_{mono}$.

6.2.1 Frequency analysis of the collective normal modes

We have investigated the eigenfrequencies of the system and have found that they are distributed at both sides of the individual strand frequency and always below the frequency of the equivalent monolithic loop (see Figure 6.2a). The lowest and highest frequencies are $\omega = 0.612\omega_{mono}$ and $\omega = 0.993\omega_{mono}$, respectively. We see that the eigenfrequencies are in a broad band of width approximately $0.38\omega_{mono}$. According to their spatial structure, we classify the normal modes in three groups. Modes with frequencies below the central frequency ($\omega < \omega_{strand}$) are called low modes (left-hand side of the shaded area in Figure 6.2a). Mid modes are those with frequencies similar to the central frequency ($\omega \approx \omega_{strand}$; shaded area in Figure 6.2a) and finally the solutions with $\omega > \omega_{strand}$ are referred to as high modes (right hand side of the shaded area in Figure 6.2a). It is important to note that in a system of non-interacting strands the frequency of oscillation of each strand is ω_{strand}.

6.2.2 Velocity and total pressure perturbation analysis

The spatial structure of the three groups of modes is clearly different. Low modes are kink-like modes in the sense that at least one strand moves transversely like a kink. For these modes, the fluid between tubes follows the strand motion (see Figure 6.3), producing chains of loops in which one follows the next. In Figure 6.3, two examples of low modes are plotted. Figure 6.3a corresponds to the lowest frequency mode, in which only five strands oscillate, producing some kind of global torsional motion of the strands. In Figure 6.3b, another example of low eigenfunction is plotted and shows that almost all the strands are excited. As in the previous example, the fluid between strands moves with them. In both modes the maximum velocity takes place inside the strands. These characteristics are shared by all the low modes. The S_x and A_y modes of the system of two loops (Chapter 4) and the m_1 to m_4 modes of a system of three aligned loops (Chapter 5) can be classified in the low mode group because the spatial structure of the magnetic pressure perturbation and velocity field have the features previously described and their frequencies are below

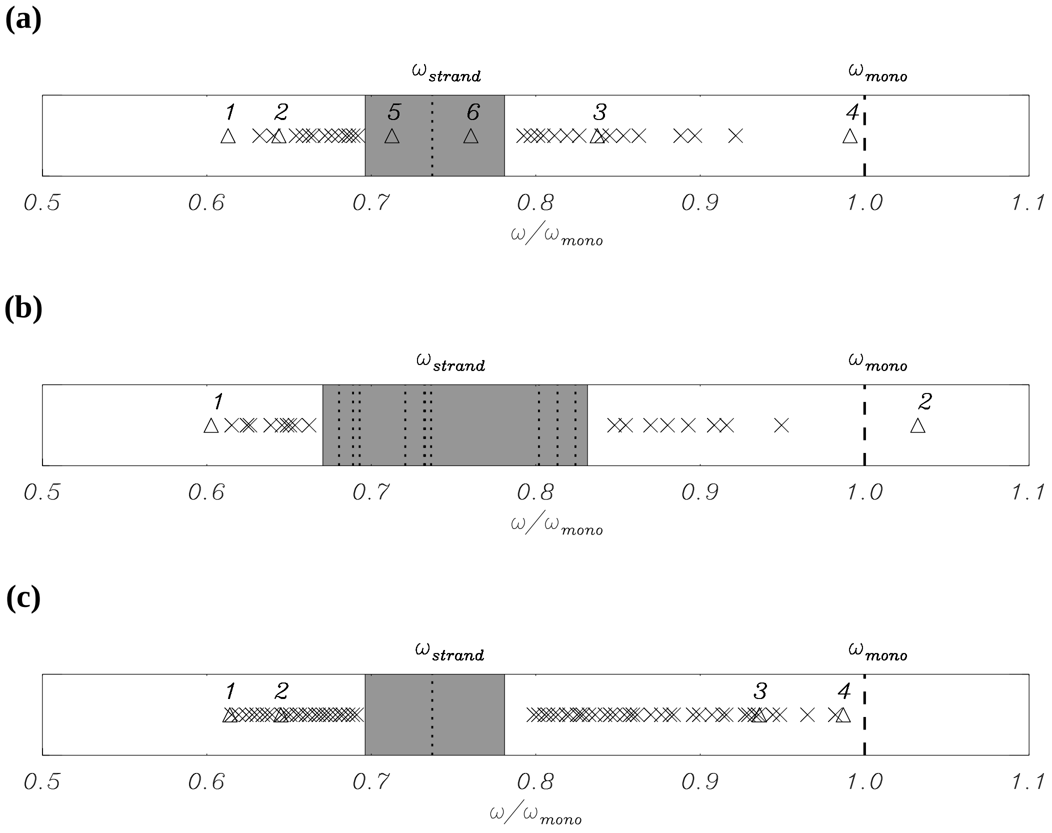

Figure 6.2: Distribution of the frequencies of the collective normal modes associated to the three systems considered in this Chapter: **(a)** 10 identical strands, **(b)** 10 nonidentical strands with different densities and, **(c)** 40 identical strands. In all cases we clearly see that the frequencies are distributed at both sides of the individual strand frequencies, ω_{strand}, (dotted line) in a broad band of frequencies and that all the modes have frequencies below ω_{mono} (dashed line). The mid modes are within the shaded area. The triangles mark the frequencies of the modes displayed in the following plots and are labelled with integers.

the corresponding individual kink frequency.

On the other hand, for the high modes the intermediate fluid between tubes is compressed or rarefied (which leads to a higher or lower total pressure perturbation) or moves in the opposite direction to the strands, producing a more forced motion than that of the low modes (see Figure 6.4). These modes are kink-like too, but, in contrast to the low modes, the maximum velocities take place in the intermediate fluid between strands, i.e. outside them. This behaviour is very clear in Figure 6.4a, in which the strand motions force the coronal fluid to pass through the narrow channels between them or to compress the coronal medium. Similarly, in the highest frequency mode (Figure 6.4b), high velocity flows between the five excited strands takes place. The coronal medium within the excited strands is compressed and rarefied, giving rise to some kind of sausage global motion of the strands. All the modes that we have classified as high share these characteristics. The S_y and A_x modes of two identical tubes (Chapter 4) and the m_5 to m_8 modes of a system of three aligned loops (Chapter 5) belong to the high group of modes.

Finally, the mid modes have the most complex spatial structure. They are fluting-like modes and have strand motions similar to those of the fluting modes of the individual tube (see Figures 6.5a and 6.5b). The magnetic pressure perturbation and velocity are concentrated mainly in the strand surface. There is an infinite number of mid modes with frequencies concentrated around $\omega \approx \omega_{strand}$, and for this reason they are plotted as a shaded area in Figure 6.2.

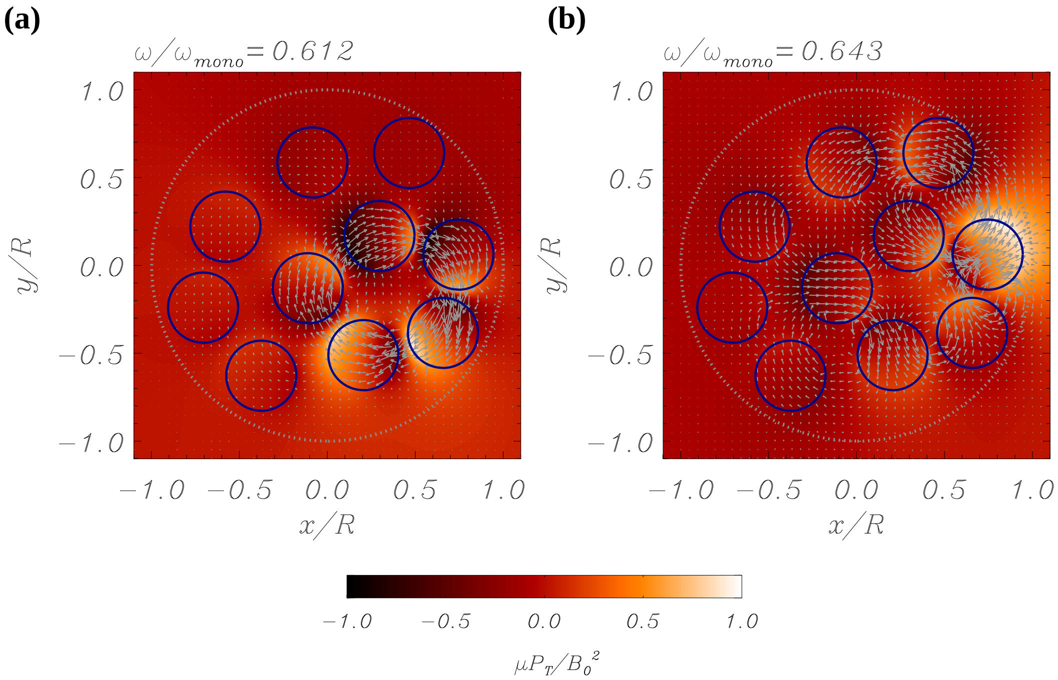

Figure 6.3: Total pressure perturbation (color field) and velocity field (arrows) of the fast collective normal modes of two low modes labelled as 1 and 2 in Figure 6.2a. **(a)** Lowest frequency mode labelled as 1. **(b)** Low mode, labelled as 2.

6.3 Normal modes of ten non-identical strands

In this Section we have considered the previous spatial distribution of strands but with different densities. The strand densities have been distributed randomly around and average density $7.5\rho_e$ with a deviation of $3\rho_e$ and the equivalent monolithic density has been kept equal to $\rho_{eq} = 3.6\rho_e$ and the volume filled by the strands to 40% that of the monolithic loop volume, as in Section 6.2. The densities we use are $\rho_j/\rho_e = \{7.89, 7.61, 7.60, 8.97,$

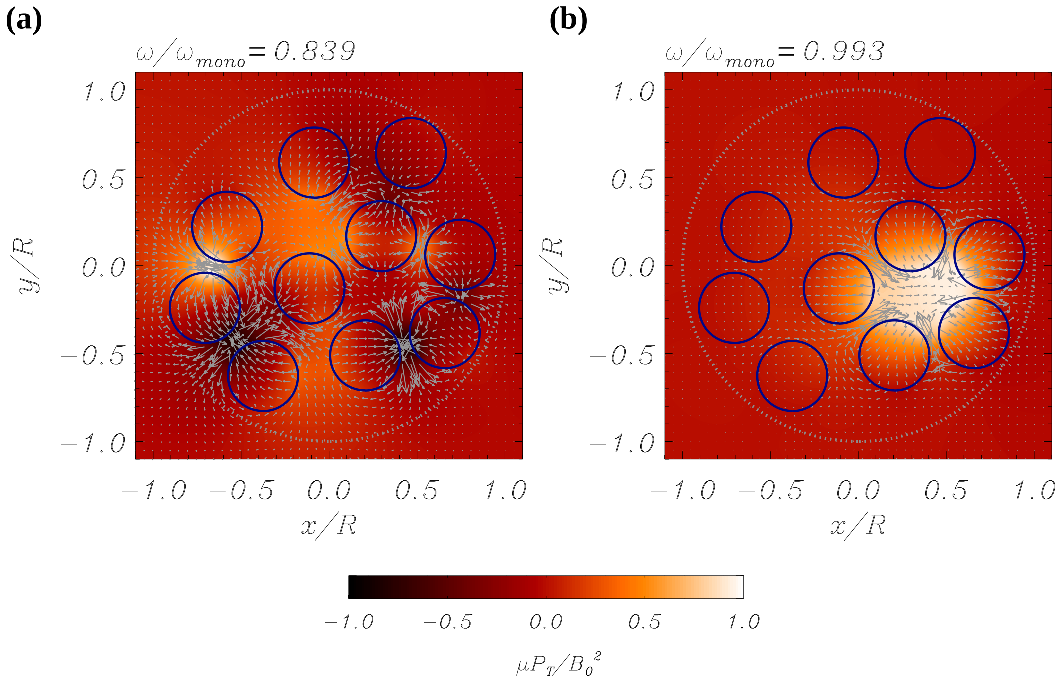

Figure 6.4: Same as Figure 6.3 for two modes classified as top. **(a)** Mode labelled as 3 in Figure 6.2a. **(b)** Highest frequency mode, labelled as 4.

5.98, 8.73, 7.52, 8.62, 6.18, 5.80} following the ordination of Figure 6.1. The density deviation implies a diference between the individual kink frequencies of the strands. This difference between the maximum and minimum values of the individual kink frequencies is $0.13\omega_{mono}$. This makes the coupling between the strands weaker (see Chapter 5 and Luna et al., 2009) than in the identical strand case discussed in Section 6.2. However, the strands still interact and so it is not possible to consider the multistranded system as a collection of individual tubes. The band of collective frequencies now goes from $\omega = 0.602\omega_{mono}$ to $\omega = 1.036\omega_{mono}$, i.e. it has a width of $0.43\omega_{mono}$, as we see in Figure 6.2b. This band is broader than in the identical strand case (for which it is $0.38\omega_{mono}$) but this does not mean that the interaction between non-identical strands is stronger. The reason is the additional broadening associated to the spreading of the individual kink frequencies, which results in the enlargement of the mid frequency band (see Figure 6.2b). Roughly speaking, the broadening associated to the coupling is then the total broadening minus the spreading of the individual kink frequencies. In case of an uncoupled system of nonidentical strands the band width associated to the coupling is zero. The individual kink frequencies of our system are in a band of $0.13\omega_{mono}$. This implies that the contribution of the strand interaction is roughly $0.30\omega_{mono}$, indicating less interaction between the strands than for the identical strand system (Section 6.2). Similarly to Section 6.2, we can divide the collective normal modes in three groups. However, the spatial structure differs from those of the previous Section. The differences are clear, for example, in the lowest frequency mode. Comparing Figure 6.6a with Figure 6.3a we see that the global torsional

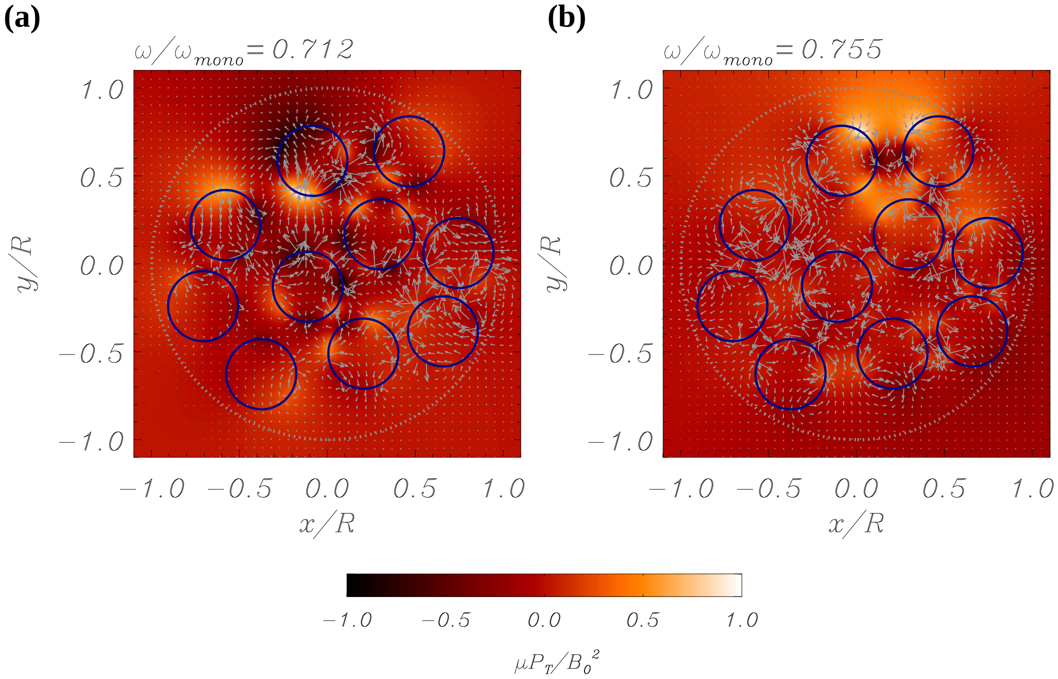

Figure 6.5: Same as Figure 6.3 for two modes classified as middle. **(a)** Mode labelled as 5 in Figure 6.2a. **(b)** Mode labelled as 6. In both cases we see the complex structure of the mid normal modes.

oscillation of the five strands labelled 2, 5, 6, 7 and 10 is avoided because their densities are very different, but the oscillation of the strands labelled as 1, 2, 3, 4, 6, 7 and 8 with similar densities, is favoured. The highest frequency mode plotted in Figure 6.6b is very similar to the corresponding mode in the identical tube case (Figure 6.4b), although the amplitude of the oscillations is concentrated in the rarest tubes, labelled 5 and 10. These results are general and the low modes have the largest oscillatory amplitudes in the denser tubes. On the contrary, for the high modes, the highest oscillatory amplitudes are associated to the rarest strands. The mid modes have complex spatial structure but similar to that of the identical strand case and are not plotted for the sake of simplicity.

In Terradas et al. (2008) a system of 10 non-homogeneous strands was considered. The authors studied the time-dependent evolution of the system after an initial excitation. They found a collective frequency $0.22/\tau_A$, where τ_A is a time unit defined in that paper as $\tau_A = v_{Ae}/R$. We have considered an equivalent system of homogeneous strands preserving the total mass and have found that modes lie in a frequency band going from $0.182/\tau_A$ to $0.23/\tau_A$ that agrees very well with the mentioned results.

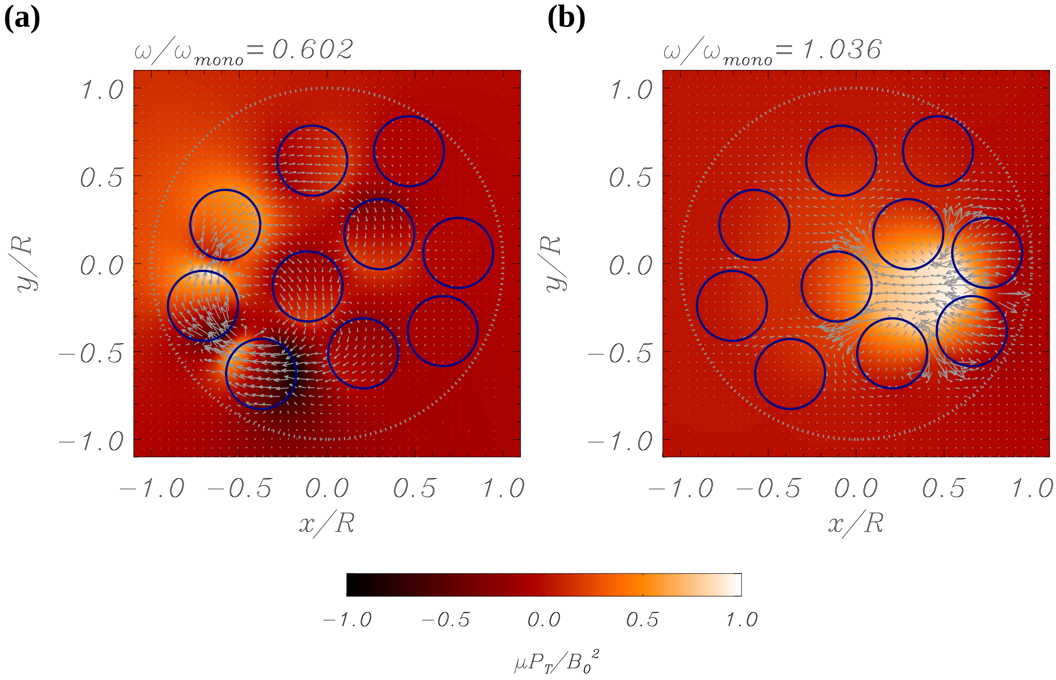

Figure 6.6: Same as Figure 6.3 for the collective normal modes of a system of 10 non-identical strands. **(a)** Lowest frequency mode, labelled as 1 in Figure 6.2b. **(b)** Highest frequency mode, labelled as 2.

6.4 Normal modes of forty identical strands

We have also found the normal modes of a much more complex system of 40 identical strands. The strands fill 40% of the equivalent loop volume, with a strand density $\rho_j = 7.5\rho_e$ and an equivalent density $\rho_{eq} = 3.6\rho_e$. The frequencies of the normal modes lie in a band that goes from $\omega = 0.614\omega_{mono}$ to $\omega = 0.987\omega_{mono}$, so that its width is $0.37\omega_{mono}$. This frequency band coincides well with that of the 10 identical strand case (see Figures 6.2a and 6.2c). However, the system of 40 strands has more collective normal modes than the system of 10 strands. The classification in low, mid and high modes is still valid in this complex system of strands. In this Section we have only considered the kink-like modes (low and high modes) and the mid modes are not plotted for the sake of simplicity. In Figures 6.7a and 6.7b, two examples of low collective normal modes are plotted. In the lowest frequency normal mode (Figure 6.7a), a cluster of close strands is excited and the others are at rest. In the second example (Figure 6.7b), a cluster of distant strands participates in the motion. In Figures 6.8a and 6.8b, two examples of high modes are also plotted. Similarly to the low modes, in the high modes a cluster of several strands participates in the motion whereas the others are at rest.

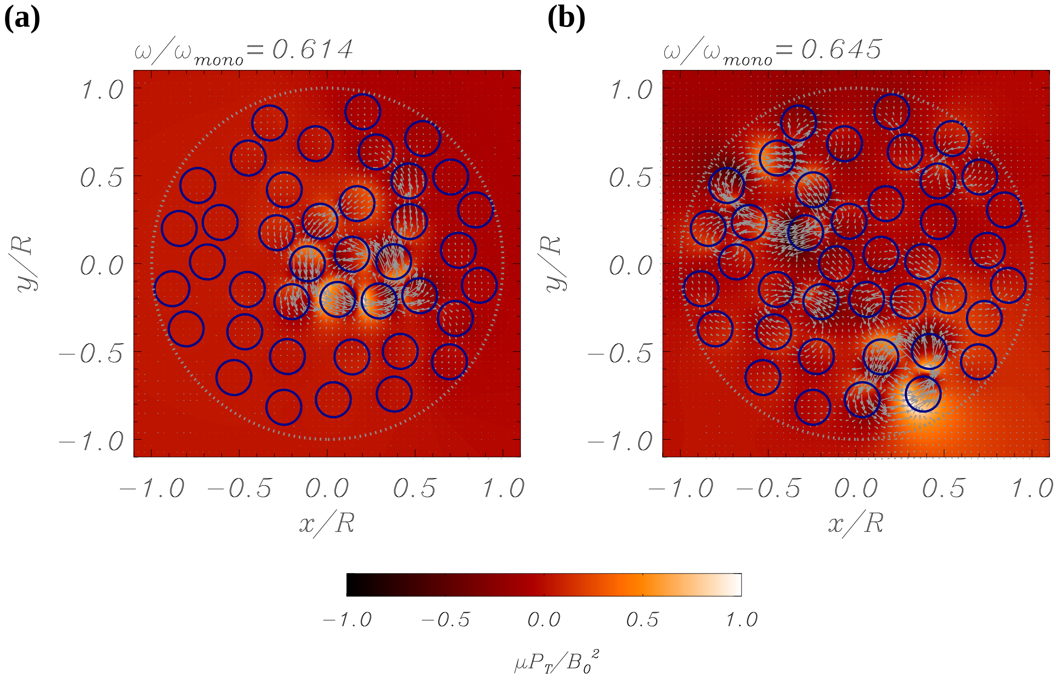

Figure 6.7: Same as Figure 6.3 for two low modes in a system of 40 identical strands. **(a)** Lowest frequency mode, labelled as 1 in Figure 6.2c. **(b)** Normal mode labelled as 2.

6.5 Discussion and conclusions

In this Chapter we have found analytically the normal modes of a multistranded coronal loop with the help of the T-matrix theory outlined in Chapter 5. The results of this work can be summarised as follows

1. We have considered a multistranded loop filled with 10 identical strands located at random positions. We have found a large quantity of normal modes whose their frequencies are in a broad band of width approximately $0.38\omega_{mono}$. All these frequencies are smaller than the monolithic kink frequency. We have seen that the collective normal modes can be classified in three groups according to their frequencies and spatial structures. Low modes have a frequency $\omega < \omega_{strand}$ and the spatial structure is kink-like and characterised by strands moving in complex chains. In these modes, the intermediate fluid between strands follows their transverse displacement and produces a non-forced motion of the system. In the low modes the strands move faster than the surrounding medium, i.e. the maximum velocities are within the strands. Mid modes have a frequency $\omega \approx \omega_{strand}$ and the spatial structure is fluting-like, by which the strands are essentially distorted and their displacements are small. Finally, high modes ($\omega > \omega_{strand}$) are kink-like modes characterised by a forced motion of the strands, that move in the opposite direction to the surrounding plasma or compress and rarefy their intermediate fluid, producing high velocities in

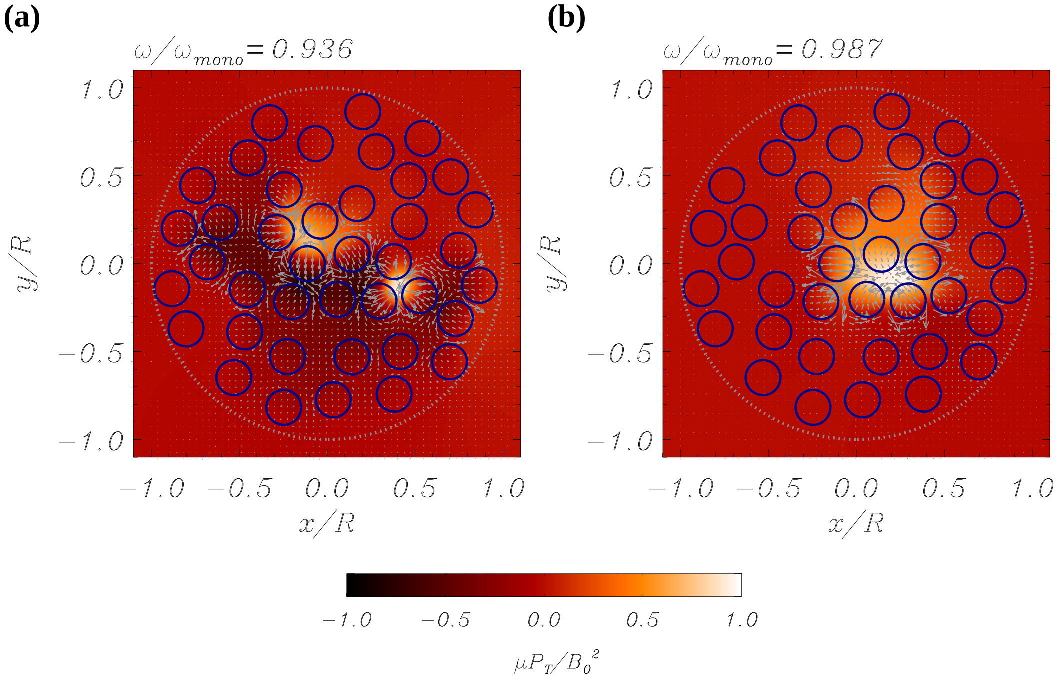

Figure 6.8: Same as Figure 6.3 for two high modes in a system of 40 identical strands. **(a)** Collective normal mode, labelled as 3 in Figure 6.2c. **(b)** Highest frequency mode, labelled as 4.

the coronal medium. Then, the surrounding medium moves faster than the strands.

2. We have also investigated a system of 10 non-identical strands. The spatial distribution of the strands is the same as in Section 6.2, but with different strand densities. Similarly to the identical strand case, we have found a large quantity of collective normal modes, but now their frequencies lie in a band of width $0.30\omega_{mono}$. This band width is narrower than that of the identical strand case of Section 6.2, indicating a weaker interaction between the strands. The collective normal modes can be also classified in low, mid and high modes. The largest oscillation amplitudes correspond to the denser strands in the low modes and to the rarest strands in the high modes.

3. The normal modes of a complex system of 40 identical strands have also been computed. Their frequencies lie in a band of width $0.37\omega_{mono}$, that coincides well with that of system of 10 identical strands. The classification of the normal modes in low, mid and high is still valid in this complex system. However, the number of normal modes is larger than in the two systems with 10 strands. This indicates that the number of collective normal modes increases with the number of strands.

The spatial structure of the normal modes is very complex and we have found no collective normal mode that can be considered as a global kink mode. In such modes, we expect that all the strands move in phase with the same direction producing a whole displacement of the loop. The collective normal modes that we have found displace the loop centre but the detailed motion of the strands is very complex. Low and high normal modes produce the largest transverse displacements of the loop, whereas the mid modes do not produce important oscillations of the whole tube. The reason is that the low and high modes are kink-like, and the combined motion of the strands produces the whole motion of the loop. However, the mid modes are fluting-like, and the individual motion of the strands does not contribute to the transverse loop motion. On the other hand, the frequencies of the normal modes lie in a broad band. These results indicates that the whole loop motion cannot be described by an equivalent monolithic and uniform loop system, with some equivalent density and its kink frequency. Otherwise, the fine structure influences the collective dynamics of the multistranded loop.

In this study we have only considered the normal modes of the system. The investigation of the time evolution after an initial disturbance is needed to understand how the different normal modes are excited, and how is the whole loop dynamics. In Chapter 4, we have shown that the motion of a two strand system is complex and that the complexity of its dynamics depends on the width of the frequency band of the collective modes. For this reason, we expect a complex dynamics of the multistranded loops studied here. Terradas et al. (2008) have found that an initial disturbance produces a displacement of the strands in the direction of the initial pulse perturbation. As we have seen, there are no normal modes with such a structure of strand oscillations, but it is possible to obtain this initial configuration by a combination of collective normal modes. We expect that after some time, each collective normal mode oscillates with different phase due to the frequency differences between them. As a consequence each strand oscillates with a complicated motion. This complex motion reflects in the variation of the direction of oscillation with time and a modulation of the amplitude (see Chapter 4). Terradas et al. (2008) considered a system of weakly coupled strands with frequencies in a band of approximately $0.12\omega_{mono}$. The rapid damping of the oscillations due to resonant absorption in the nonuniform layers of the strands makes very difficult the study of the collective dynamics. However, we expect that the collective dynamics can contribute to the observed damping of transverse loop oscillations.

Chapter 7

Conclusions and future work

7.1 Conclusions

The main goal of this Thesis has been to study the collective transverse oscillations of composite coronal magnetic structures. This investigation has focused on bundles and arcades of coronal loops belonging to active regions and on a multistranded loop model with internal fine structure. The work has been carried out by solving the governing equations analytically and numerically, providing a sound theoretical basis for more realistic magnetohydrodynamic coronal seismology.

Firstly, we modelled a loop as a magnetic slab, studying a simple system of two identical slabs. In Chapter 3 we studied the collective oscillations of this configuration and found analytically the normal modes. There are two fundamental normal modes, the symmetric and antisymmetric collective modes, in which the slabs move in phase or antiphase, respectively. Both these modes have different frequencies: the symmetric mode has a smaller frequency than that of the individual slab, while the opposite happens with the antisymmetric mode. The symmetric mode is always trapped, but the antisymmetric mode can be leaky or trapped according to the separation between the slabs. In addition, we numerically solved the initial value problem, perturbing the system with a pulse with a Gaussian shape. We then investigated the collective excitation and the time evolution as a function of the slab separation. In all cases, after a transient phase, the system oscillates with a combination of collective normal modes. In a range of slab separations the amplitude of oscillation shows a sinusoidal modulation, which is the well known collective beating phenomenon. In this range of separations the slabs interchange energy periodically, indicating a complex behaviour of the system.

The interaction between the loops depends on the considered geometry and on how the flux tubes perturb their surrounding plasma and magnetic field. Consequently, in the second step, we considered a cylindrical loop model. In Chapter 4, we studied two identical and parallel cylindrical loops. We found four collective normal modes called S_x,

A_y, S_y and A_x, where S and A stand for the phase and antiphase motions, respectively (the subscripts are the direction of oscillation). It is important to note that the system dynamics are not the sum of two individual loops moving independently. We investigated the system oscillations after an initial disturbance solving the initial value problem numerically in two dimensions. After different numerical experiments with different incidence angles, we found that the system oscillates with a combination of four collective normal modes after a very brief transient phase. The amplitude of oscillation of each normal mode depends on the incidence angle of the initial pulse, with the dynamics of the two loop system being very complex, indicating strong interaction between the flux tubes.

In Chapter 5 we generalised our investigation to complex systems of parallel cylindrical flux tubes using T-matrix theory. The first system that we considered is made of two non-identical tubes, in order to investigate the dependence of loop coupling with respect to their relatives densities and radii. We found that the system is coupled if their densities or radii are similar and the normal modes of the system are collective. On the other hand, the system behaves as two independent loops if their densities are sufficiently different. In the range of observed loop radii the interaction does not depend strongly on this parameter and the loops are coupled. A further study was made of a system with three identical loops and this produced eight kink-like normal modes. In addition, we investigated the dependence of the interaction between the three loops with their relative density. Our study showed that loops with similar kink frequencies are coupled and their dynamics are collective, but if their kink frequencies are sufficiently different they are uncoupled and behave as independent tubes. Importantly, these advanced theoretical results can be actually be applied to real observations of coronal loop system oscillations. Observed loops that share their frequencies are likely to be coupled and probably have similar densities, but on the other hand, loops whose frequencies do not coincide are probably uncoupled oscillators. Crucially, the assumption of individual instead of collective motion might produce a seismological underestimation of the magnetic field or overestimation of the loop density.

Finally, in Chapter 6 we applied the T-matrix theory outlined in Chapter 5 to find the collective normal modes of the multistranded loop model, in which our system consists of several thin and close strands. We first considered a collection of ten identical strands and found a huge quantity of normal modes with their frequencies lying in a broad band at both sides of the individual strand frequency. The collective normal modes can be classified as low, mid and high frequency modes according to their frequencies and spatial structure. Low modes have frequencies smaller than an individual strand kink frequency and their spatial structure is basically kink-like, with the motion of the strands following one another in the form of a complex chains of strands. In these modes, the intermediate fluid between strands follows the tubes and produces a non-forced motion of the system. With the low frequency modes, the strands move faster than the surrounding medium, i.e. the maximum velocities are within the strands. Mid frequency modes have a frequency similar to the individual strand kink frequency and their spatial structure is fluting-like, i.e. the strands are essentially distorted and their displacements are small. Interestingly, in this complex equilibrium configuration, there can exist an infinite number of mid frequency fluting-like modes. Finally, high frequency modes, with frequencies greater than the strand kink frequency, are kink-like modes characterised by a forced motion of the strands, that move oppositely to the surrounding plasma or compress and rarefy the intermediate fluid, producing high velocities in the coronal medium causing the surrounding medium to move faster than the strands. We also considered a system of ten strands with different densities, in which we found similar results but with the frequency band of the collective normal modes being narrower. The reason for this is that the coupling between the non-identical strands is weaker than in the identical strand configuration, but our classification of the normal modes in the low, mid and high frequencies is still valid. In order to confirm our results we considered a much more complex system made of forty strands and found that the results agree with the ten strand case. However, there are many more collective modes than in the simpler case. One of the most important results of our analysis is that there is no global kink normal mode with all the strands moving in phase in the same direction. This shows that the internal structuring of a loop can affect the global motion and produces amplitude modulations and changes in the transverse direction of oscillation.

In summary, in this Thesis the transverse oscillations of several loops and their collective behaviour were investigated. We performed our study firstly by considering a very simplified two loop model and then increased the complexity by increasing the number of loops, thereby creating a more realistic configuration. In addition, we investigated the transverse oscillations of a loop with fine structure and found that its internal structure affects the global motion of the loop. With the purpose of gaining even more progress in coronal physics, some further key topics not addressed in this Thesis, related to coronal loop modelling, should be the subject of future research and these will be discussed in the next and final Section.

7.2 Future work

In Chapters 3, 4 and 5 the coupling between loops was investigated and we identified collective oscillation signatures and determined under which conditions coupling takes place. With these new results it is now possible to attempt more advanced coronal seismology by reinterpreting existing observational results. For example, in the harmonica event reported by Verwichte et al. (2004), the physical reason why three groups of coronal loops are oscillating with similar frequencies may be explained for the first time. Since there is similarity in the observed frequencies, it is possible that the oscillations of these loops are coupled. However, a more detailed study of their relative phase and position is needed before a more definite answer can be made and this should be the aim of future work in this field. If their oscillations are indeed coupled, the theory developed in this Thesis may provide fine corrections to the densities and magnetic fields estimated by the method of coronal seismology. In addition, new telescopes and new observations with improved temporal and spatial resolution will increase the possibility of identifying such coupled loops oscillations.

Concerning the multistranded loop model, the next step is to consider the normal modes of the system for different filling factors. Additionally, by using the long wavelength approximation it is possible to find an expression for the band of frequencies of the collective normal modes. This analytical expression can be related with the mean strand characteristics and would also be a useful tool for coronal seismology. On the other hand, there is a huge quantity of normal modes in a multistranded loop. It is necessary to study which combination of normal modes are excited after an initial disturbance as this determines the temporal evolution of the whole loop system. This last point is very interesting as the resulting collective loop motion can be very complex (see even the simple case of two tubes studied in Section 4.4). Therefore, if such complicated loop motions are actually observed this would be a strong indication of sub-resolution internal fine structuring.

The theoretical models presented in this Thesis are only an approximation to the real situations, however, such models allows us to understand how the different physical processes take place. After our initial simple model it is was necessary to increase the complexity to have a more realistic system. Following this idea, a natural extension to make our modelling more realistic would be to introduce plasma structuring along coronal loops (or the component strands) and the surrounding medium. Some work has already been made in this regard, for example, by Hanasoge and Cally (2009) and Jain et al. (2009). These authors have studied the scattering of the *p*-modes stratified fibrils and found that multiple-scattering is important in the solar plage. Similar studies can be also made relating to the solar corona to investigate the effect of longitudinal loop or strand stratification on the collective dynamics.

List of Figures

Bibliography

Arregui, I., Terradas, J., Oliver, R., and Ballester, J. L. (2007). The influence of the internal structuring of coronal loops on the properties of their damped transverse oscillations. *A&A*, 466:1145–1151. 21

Aschwanden, M. J., de Pontieu, B., Schrijver, C. J., and Title, A. M. (2002). Transverse Oscillations in Coronal Loops Observed with TRACE II. Measurements of Geometric and Physical Parameters. *Sol. Phys.*, 206:99–132. 16, 18, 85, 121

Aschwanden, M. J., Fletcher, L., Schrijver, C. J., and Alexander, D. (1999). Coronal Loop Oscillations Observed with the Transition Region and Coronal Explorer. *ApJ*, 520:880–894. 16, 85

Aschwanden, M. J., Nakariakov, V. M., and Melnikov, V. F. (2004). Magnetohydrodynamic Sausage-Mode Oscillations in Coronal Loops. *ApJ*, 600:458–463. 24

Aschwanden, M. J. and Nightingale, R. W. (2005). Elementary Loop Structures in the Solar Corona Analyzed from TRACE Triple-Filter Images. *ApJ*, 633:499–517. 15

Aschwanden, M. J., Nightingale, R. W., and Alexander, D. (2000). Evidence for Nonuniform Heating of Coronal Loops Inferred from Multithread Modeling of TRACE Data. *ApJ*, 541:1059–1077. 15, 17, 121

Aschwanden, M. J., Nightingale, R. W., Andries, J., Goossens, M., and Van Doorsselaere, T. (2003). Observational Tests of Damping by Resonant Absorption in Coronal Loop Oscillations. *ApJ*, 598:1375–1386. 95, 106

Berghmans, D. and Clette, F. (1999). Active region EUV transient brightenings - First Results by EIT of SOHO JOP80. *Sol. Phys.*, 186:207–229. 18

Berton, R. and Heyvaerts, J. (1987). Magnetohydrodynamic modes of a periodic magnetic medium. *Sol. Phys.*, 109:201–231. 21

Bogdan, T. B. and Knoelker, M. (1991). Scattering of acoustic waves from a magnetic flux tube embedded in a radiating fluid. *ApJ*, 369:219–236. 68

Bogdan, T. J. (1987). Propagation of compressive waves through fibril magnetic fields. II - Scattering from a slab of magnetic flux tubes. *ApJ*, 318:888–895. 87

Bogdan, T. J. and Cattaneo, F. (1989). The normal modes of a resonant cavity containing discrete inhomogeneities - The influence of fibril magnetic fields on the solar acoustic oscillations. *ApJ*, 342:545–557. 87, 89, 90, 91

Bogdan, T. J. and Fox, D. C. (1991). Multiple scattering of acoustic waves by a pair of uniformly magnetized flux tubes. *ApJ*, 379:758–775. 68, 87, 102

Bogdan, T. J. and Zweibel, E. G. (1985). Effect of a fibril magnetic field on solar p-modes. *ApJ*, 298:867–875. 68, 87, 90, 91

Bogdan, T. J. and Zweibel, E. G. (1987). Propagation of compressive waves through fibril magnetic fields. *ApJ*, 312:444–456. 87

Cally, P. S. (1986). Leaky and non-leaky oscillations in magnetic flux tubes. *Sol. Phys.*, 103:277–298. 60, 63

Cally, P. S. (2003). Coronal Leaky Tube Waves and Oscillations Observed with Trace. *Sol. Phys.*, 217:95–108. 63

Chen, F. F. (1984). *Introduction to Plasma Physics and Controlled Fusion. Volume 1*. Plenum Press. 23

De Moortel, I., Ireland, J., Hood, A. W., and Walsh, R. W. (2002). The detection of 3 & 5 min period oscillations in coronal loops. *A&A*, 387:L13–L16. 18

De Moortel, I., Ireland, J., and Walsh, R. W. (2000). Observation of oscillations in coronal loops. *A&A*, 355:L23–L26. 18

DeForest, C. E. (2007). On the Size of Structures in the Solar Corona. *ApJ*, 661:532–542. 15

Díaz, A. J., Oliver, R., and Ballester, J. L. (2005). Fast magnetohydrodynamic oscillations in a multifibril Cartesian prominence model. *A&A*, 440:1167–1175. 21, 57, 69

Edwin, P. M. and Roberts, B. (1982). Wave propagation in a magnetically structured atmosphere. III - The slab in a magnetic environment. *Sol. Phys.*, 76:239–259. 31

Edwin, P. M. and Roberts, B. (1983). Wave propagation in a magnetic cylinder. *Sol. Phys.*, 88:179–191. 60, 62, 63, 67

Goedbloed, J. P. H. and Poedts, S. (2004). *Principles of Magnetohydrodynamics*. Cambridge University Press. 23, 30

Goossens, M. (2003). *An introduction to plasma astrophysics and magnetohydrodynamics*, volume 294 of *Astrophysics and Space Science Library*. 23

Goossens, M., Andries, J., and Aschwanden, M. J. (2002). Coronal loop oscillations. An interpretation in terms of resonant absorption of quasi-mode kink oscillations. *A&A*, 394:L39–L42. 17

Goossens, M., Terradas, J., Andries, J., Arregui, I., and Ballester, J. L. (2009). On the nature of kink MHD waves in magnetic flux tubes. *ArXiv e-prints*. 20, 60

Hanasoge, S. M. and Cally, P. S. (2009). Multiple Scattering of Waves by a Pair of Gravitationally Stratified Flux Tubes. *ApJ*, 697:651–659. 120

Hindman, B. W. and Jain, R. (2008). The Generation of Coronal Loop Waves below the Photosphere by p-Mode Forcing. *ApJ*, 677:769–780. 19

Jain, R., Hindman, B. W., Braun, D. C., and Birch, A. C. (2009). Absorption of p Modes by Thin Magnetic Flux Tubes. *ApJ*, 695:325–335. 120

Keppens, R. (1994). *On the interaction of acoustic oscillations with magnetic flux tubes in the Solar photosphere*. PhD thesis, cooperative Ph.D. thesis, Katholieke Univ. Leuven and Nat. Center Atmos. Res., (1994). 91, 102

Keppens, R., Bogdan, T. J., and Goossens, M. (1994). Multiple scattering and resonant absorption of p-modes by fibril sunspots. *ApJ*, 436:372–389. 68, 87, 88, 103

Klimchuk, J. A. (2006). On Solving the Coronal Heating Problem. *Sol. Phys.*, 234:41–77. 15

Leveque, R. J. (2002). *Finite Volume Methods for Hyperbolic Problems*. Cambridge University Press. 71

Luna, M., Terradas, J., Oliver, R., and Ballester, J. L. (2006). Fast magnetohydrodynamic waves in a two-slab coronal structure: collective behaviour. *A&A*, 457:1071–1079. 22, 31, 69, 82, 84

Luna, M., Terradas, J., Oliver, R., and Ballester, J. L. (2008). Transverse Oscillations of Two Coronal Loops. *ApJ*, 676:717–727. 22, 59, 93, 102

Luna, M., Terradas, J., Oliver, R., and Ballester, J. L. (2009). Transverse Oscillations of Systems of Coronal loops. *ApJ*, 692:1582–1589. 22, 87, 110

Murawski, K. (1993). Cross-talk in solar coronal loops. *Acta Astronomica*, 43:161–176. 21

Murawski, K. and Roberts, B. (1994). Time signatures of impulsively generated waves in a coronal plasma. *Sol. Phys.*, 151:305–317. 21

Nakariakov, V. M. and Ofman, L. (2001). Determination of the coronal magnetic field by coronal loop oscillations. *A&A*, 372:L53–L56. 17

Nakariakov, V. M., Ofman, L., Deluca, E. E., Roberts, B., and Davila, J. M. (1999). TRACE observation of damped coronal loop oscillations: Implications for coronal heating. *Science*, 285:862–864. 16, 17, 19, 85, 121

Nakariakov, V. M. and Verwichte, E. (2005). Coronal Waves and Oscillations. *Living Reviews in Solar Physics*, 2:3. 20, 122

Nightingale, R. W., Aschwanden, M. J., and Hurlburt, N. E. (1999). Time Variability of EUV Brightenings in Coronal Loops Observed with TRACE. *Sol. Phys.*, 190:249–265. 18

Ofman, L. and Wang, T. (2002). Hot Coronal Loop Oscillations Observed by SUMER: Slow Magnetosonic Wave Damping by Thermal Conduction. *ApJL*, 580:L85–L88. 19

O'Shea, E., Banerjee, D., Doyle, J. G., Fleck, B., and Murtagh, F. (2001). Active region oscillations. *A&A*, 368:1095–1107. 18

Priest, E. R. (1987). *Solar magneto-hydrodynamics*. Dordrecht: D. Reidel. 24, 26

Ramm, A. G. (1989). *Scattering by obstacles*. D.Reidel Publishing Company. 87, 89

Roberts, B., Edwin, P. M., and Benz, A. O. (1984). On coronal oscillations. *ApJ*, 279:857–865. 19

Schmelz, J. T., Nasraoui, K., Richardson, V. L., Hubbard, P. J., Nevels, C. R., and Beene, J. E. (2005). All Coronal Loops Are the Same: Evidence to the Contrary. *ApJL*, 627:L81–L84. 15

Schrijver, C. J., Aschwanden, M. J., and Title, A. M. (2002). Transverse oscillations in coronal loops observed with TRACE I. An Overview of Events, Movies, and a Discussion of Common Properties and Required Conditions. *Sol. Phys.*, 206:69–98. 16, 85, 103

Schrijver, C. J. and Brown, D. S. (2000). Oscillations in the Magnetic Field of the Solar Corona in Response to Flares near the Photosphere. *ApJL*, 537:L69–L72. 16, 20, 103

Schrijver, C. J., Title, A. M., Berger, T. E., Fletcher, L., Hurlburt, N. E., Nightingale, R. W., Shine, R. A., Tarbell, T. D., Wolfson, J., Golub, L., Bookbinder, J. A., Deluca, E. E., McMullen, R. A., Warren, H. P., Kankelborg, C. C., Handy, B. N., and de Pontieu, B. (1999). A new view of the solar outer atmosphere by the Transition Region and Coronal Explorer. *Sol. Phys.*, 187:261–302. 16, 18

Sewell, G. (2005). *The Numerical Solution of Ordinary and Partial Differential Equations*. Wiley-Interscience. 41, 68

Spruit, H. C. (1982). Propagation speeds and acoustic damping of waves in magnetic flux tubes. *Sol. Phys.*, 75:3–17. 60, 63

Terradas, J. (2009). Excitation of standing kink oscillations in coronal loops. *ArXiv e-prints*. 63

Terradas, J., Andries, J., and Goossens, M. (2007). On the Excitation of Leaky Modes in Cylindrical Loops. *Sol. Phys.*, 246:231–242. 63

Terradas, J., Arregui, I., Oliver, R., Ballester, J. L., Andries, J., and Goossens, M. (2008). Resonant Absorption in Complicated Plasma Configurations: Applications to Multistranded Coronal Loop Oscillations. *ApJ*, 679:1611–1620. 111, 115

Terradas, J., Oliver, R., and Ballester, J. L. (2005a). On the excitation of trapped and leaky modes in coronal slabs. *A&A*, 441:371–378. 33, 35, 36, 41, 42, 122

Terradas, J., Oliver, R., and Ballester, J. L. (2005b). The Excitation and Damping of Transversal Coronal Loop Oscillations. *ApJL*, 618:L149–L152. 34

Terradas, J., Oliver, R., and Ballester, J. L. (2006). Damping of Kink Oscillations in Curved Coronal Loops. *ApJL*, 650:L91–L94. 59

Tomczyk, S. and McIntosh, S. W. (2009). Time-Distance Seismology of the Solar Corona with CoMP. *ApJ*, 697:1384–1391. 19

Tomczyk, S., McIntosh, S. W., Keil, S. L., Judge, P. G., Schad, T., Seeley, D. H., and Edmondson, J. (2007). Alfvén Waves in the Solar Corona. *Science*, 317:1192. 19

Uchida, Y. (1970). Diagnosis of Coronal Magnetic Structure by Flare-Associated Hydromagnetic Disturbances. *PASJ*, 22:341. 19

Van Doorsselaere, T., Debosscher, A., Andries, J., and Poedts, S. (2004). The effect of curvature on quasi-modes in coronal loops. *A&A*, 424:1065–1074. 59

Van Doorsselaere, T., Nakariakov, V. M., and Verwichte, E. (2008a). Detection of Waves in the Solar Corona: Kink or Alfvén? *ApJL*, 676:L73–L75. 19

Van Doorsselaere, T., Nakariakov, V. M., Young, P. R., and Verwichte, E. (2008b). Coronal magnetic field measurement using loop oscillations observed by Hinode/EIS. *A&A*, 487:L17–L20. 16

Van Doorsselaere, T., Ruderman, M. S., and Robertson, D. (2008c). Transverse oscillations of two parallel coronal loops. *A&A*, 485:849–857. 94, 96, 97, 101, 127, 128

Verwichte, E., Aschwanden, M. J., Van Doorsselaere, T., Foullon, C., and Nakariakov, V. M. (2009). Seismology of a Large Solar Coronal Loop from EUVI/STEREO Observations of its Transverse Oscillation. *ApJ*, 698:397–404. 16

Verwichte, E., Nakariakov, V. M., Ofman, L., and Deluca, E. E. (2004). Characteristics of transverse oscillations in a coronal loop arcade. *Sol. Phys.*, 223:77–94. 20, 21, 58, 85, 86, 103, 119, 122

Wang, T., Solanki, S. K., Curdt, W., Innes, D. E., and Dammasch, I. E. (2002). Doppler Shift Oscillations of Hot Solar Coronal Plasma Seen by SUMER: A Signature of Loop Oscillations? *ApJL*, 574:L101–L104. 19

Wang, T. J., Solanki, S. K., Curdt, W., Innes, D. E., Dammasch, I. E., and Kliem, B. (2003a). Hot coronal loop oscillations observed with SUMER: Examples and statistics. *A&A*, 406:1105–1121. 19

Wang, T. J., Solanki, S. K., Innes, D. E., Curdt, W., and Marsch, E. (2003b). Slow-mode standing waves observed by SUMER in hot coronal loops. *A&A*, 402:L17–L20. 19

Warren, H. P., Ugarte-Urra, I., Doschek, G. A., Brooks, D. H., and Williams, D. R. (2008). Observations of Active Region Loops with the EUV Imaging Spectrometer on Hinode. *ApJL*, 686:L131–L134. 15

Warren, H. P., Winebarger, A. R., and Hamilton, P. S. (2002). Hydrodynamic Modeling of Active Region Loops. *ApJL*, 579:L41–L44. 15

Waterman, P. C. (1969). New formulation of acoustic scattering. *The Journal of the Acoustical Society of America*, 45(6):1417–1429. 87, 89, 90

Waterman, P. C. and Truell, R. (1961). Multiple scattering of waves. *Journal of Mathematical Physics*, 2(4):512–537. 87